

# **Mid-infrared photonic devices for stellar interferometry**

**Dissertation**  
**zur Erlangung des akademischen Grades**  
**doctor rerum naturalium (Dr. rer. nat.)**

**vorgelegt dem Rat der Physikalisch-Astronomischen Fakultät  
der Friedrich-Schiller-Universität Jena**

von M.Sc. Romina Diener

geboren am 07.10.1988 in Nordhausen

## **Gutachter**

1. Prof. Dr. Thomas Pertsch, Friedrich-Schiller-Universität, Jena
2. Prof. Dr. Morten Bache, Technical University of Denmark, Lyngby
3. Prof. Dr. Alex Fuerbach, Macquarie University, Australia

Tag der Disputation: 22.08.2018

# Contents

<b>1</b>	<b>Introduction</b>	<b>3</b>
<b>2</b>	<b>Waveguide manufacturing using ultrafast laser inscription</b>	<b>10</b>
2.1	Ultrafast laser inscription in transparent materials . . . . .	10
2.2	Gallium lanthanum sulfide glass . . . . .	13
2.3	Single mode waveguides in GLS . . . . .	17
2.4	Structural modifications induced by femtosecond laser irradiation . .	23
2.4.1	Scanning electron microscopy . . . . .	23
2.4.2	Raman spectroscopy . . . . .	26
2.4.3	Polarimetric imaging . . . . .	31
2.5	Reduction of laser induced stresses by annealing . . . . .	34
2.6	Conclusions . . . . .	40
<b>3</b>	<b>Integrated optics beam combination for astronomical interferometry</b>	<b>43</b>
3.1	Evanescent coupling in integrated optics waveguides . . . . .	43
3.2	Deriving coupling coefficients and propagation constants with directional couplers . . . . .	46
3.3	Integrated optics for stellar interferometry . . . . .	49
3.4	Interferometry using arrays of straight waveguides . . . . .	52
3.4.1	Design of zig-zag discrete beam combiners . . . . .	53
3.4.2	Stress management in zig-zag discrete beam combiners . . . . .	55
3.4.3	Interferometric characterization of zig-zag discrete beam combiners . . . . .	60
3.5	Direct beam combination with the ABCD configuration . . . . .	64
<b>4</b>	<b>Nonlinear properties of gallium lanthanum sulfide glass</b>	<b>67</b>
4.1	Supercontinuum generation . . . . .	67

---

4.2	Nonlinearity of transparent materials . . . . .	68
4.3	Derivation of the propagation equation . . . . .	69
4.4	Inelastic Raman scattering . . . . .	71
4.4.1	Measurement of the Raman response . . . . .	72
4.4.2	Simulation of the output signal . . . . .	75
4.4.3	Application . . . . .	77
<b>5</b>	<b>Conclusions and Outlook</b>	<b>78</b>
	<b>References</b>	<b>I</b>
	<b>List of abbreviations</b>	<b>XXI</b>
	<b>Curriculum vitae / Lebenslauf</b>	<b>XXIII</b>
	<b>Ehrenwörtliche Erklärung</b>	<b>XXIV</b>
	<b>Acknowledgements</b>	<b>XXV</b>

# Chapter 1

## Introduction

The key to astronomical imaging is an excellent spatial resolution. Astronomical objects, such as binary stars or parent stars and their companions, can only be distinguished from each other by observing a high resolution image of the object. A higher resolution for a single telescope can be achieved by enlarging the diameter  $D$  of a single telescope because the angular resolution  $\Delta\theta$  satisfies the Rayleigh criterion  $\Delta\theta = \frac{1.22\lambda}{D}$  for the operation wavelength  $\lambda$ . The typical spot size of a seeing limited single telescopes is 1 to 2 arcseconds. Nevertheless, this is only achievable by using adaptive optics that corrects wave front disturbances caused by atmospheric turbulence [1] while the enhancement of telescope diameters has technical limits. It is not possible to extend the telescope diameter of a single telescope using adaptive optics to hundreds of meters. The main mirror of the Extremely Large Telescope (ELT), which is currently being built in Chile to be the biggest telescope in the world, will have a telescope diameter of 39 m, which is close to the upper limit of the possible dimensions. Equipped with adaptive optics, it has an expected angular resolution of 5 milliarcseconds. [2]

Optical interferometry combines multiple separate telescopes. It is a technique that increases the angular resolution of astronomical imaging compared to large single telescopes. Accordingly, stellar interferometry has a complex field of applications. Telescope interferometers explore, amongst exoplanets [3], which might lead to the discovery of earth-like planets that provide environmental conditions that allow the formation of life, young stars [4], the massive black hole in the galactic center [5], proto-planetary disks and the formation of young planets [6, 7] and much more. Considering a distant light source observed with a two element interferometer, the light is sampled at two different locations  $\vec{r}_1$  and  $\vec{r}_2$  at different times  $t_1$  and  $t_2$ . The correlation of measurements of the two electric fields is expressed in the coherence

function. The most interesting cases are temporal coherence, which describes the measurements of the electric fields at the same location but at different times, and spatial coherence, in which the measurement points have a spatial separation but the measurements are done at the same time.

The temporal coherence function  $V$  describes the correlation in time of an electric field  $E$  along a given wave train, as it is measured in a Michelson interferometer [8, 9]. It is defined as

$$\langle E^*(\vec{r}_1, t_1) \times E(\vec{r}_2, t_2) \rangle = V(\vec{r}_1 - \vec{r}_2, t_1 - t_2) = V(\vec{0}, \tau). \quad (1.1)$$

The Wiener-Khinchin theorem states that the normalized value of the temporal coherence function equals the Fourier transform of the normalized spectral energy distribution of the source. [10, 11]

The spatial coherence function

$$\langle E^*(\vec{r}_1, t_1) \times E(\vec{r}_2, t_2) \rangle = V(\vec{r}_1 - \vec{r}_2, t_1 - t_2) = V(\vec{\rho}, 0) \quad (1.2)$$

measures the correlation in space of the electric fields perpendicular to a wave train, as it is measured in Young's double slit experiment [12]. If  $|V(\vec{\rho}, \tau)| = 1$  the fields would be completely monochromatic, while for  $V(\vec{\rho}, \tau) \rightarrow 0$  they are incoherent and show no interference at all.

The foundation to the interferometry is in the Van Cittert-Zernike theorem. It states that the spatial coherence function of light from a source located far away is the Fourier transform of its angular brightness distribution and can be written as

$$V_{r,\text{norm}}(u, v) = \frac{\iint I(\alpha, \beta) \exp(-2i\pi(u\alpha + v\beta)) d\alpha d\beta}{\iint I(\alpha, \beta) d\alpha d\beta} \quad (1.3)$$

with  $\alpha$  and  $\beta$  as sky coordinates and  $u$  and  $v$  as the vector baseline between the sampling points projected to a plane oriented perpendicular to the source direction (called the  $(u,v)$ -plane). [10, 11]

For stellar interferometry the spatial coherence function (also called visibility function) is highly interesting, because it contains information about the structure of an astronomical object. For a suitable set of baselines the structure of the source can be reconstructed using the inverse Fourier transform of  $V_r(u, v)$ . [1, 10] The quality of the image can be enhanced by a denser sampling of the  $(u,v)$ -plane, which can be accomplished by the visibility measurement using multiple telescopes and multiple baselines. [13]

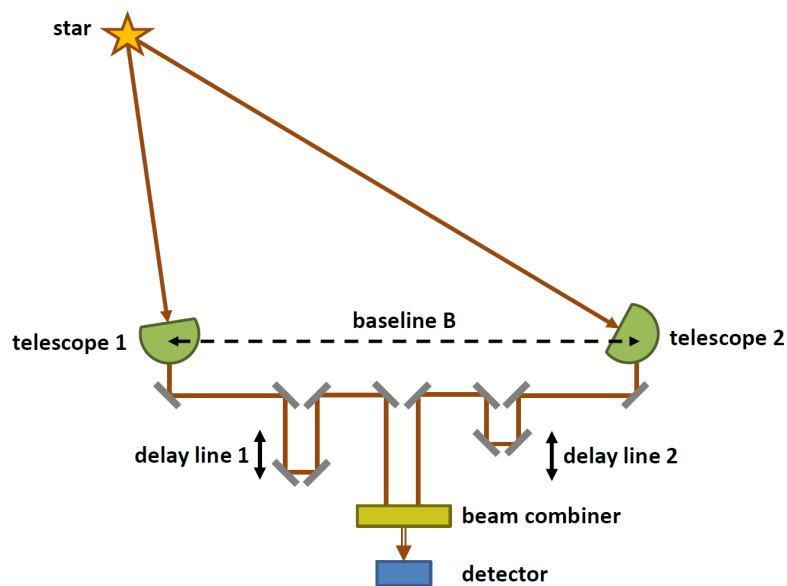


Figure 1.1: Scheme of an interferometer using 2 telescopes.

An interferometric setup for two telescopes is shown in Fig. 1.1. The light that is collected for optical interferometry is transported by delay lines. A fringe tracker corrects the optical path lengths due to transmission of the stellar light through atmospheric turbulences and coherently combines the light within an optical instrument. [14] Finally, the mutual coherence of each possible telescope pair is analyzed. [15] Recent telescope interferometers have an angular resolution of milliarcseconds [13], such as the instruments implemented at the Very Large Telescope Interferometer (VLTI) in Chile. The VLTI has four 8.2 m unit telescopes and four 1.8 m auxiliary telescopes which are organized in six different baselines at most. [16] It is equipped with three operational interferometer instruments: PIONEER [17] which observes in the H and K band, as well as AMBER [18] and GRAVITY [19] in the K band. Another instrument for L, M and N band which is called MATISSE [20] is currently being commissioned. The Center for High Angular Resolution Astronomy (CHARA) array located in California (United States) has six 1 m telescopes with the longest baseline of 330.7 m which can detect astronomical objects in the V, R, I, J, H and K band. [21] The Large Binocular Telescope Interferometer (LBTI) allows the observation of astronomical objects in the L, M and N band [22]. The two 8.4 m wide telescopes, separated by 14.4 m are located in Arizona (United States). The limitation of infrared interferometry of earth-based telescopes is atmospheric absorption. The telescopes are often placed in areas with a low appearance of water vapor. Nevertheless, there are wavelength bands which are not transparent for infrared light. The wavelength windows which can be used for infrared astronomy are shown in Table 1.2.

astronomical band	wavelengths [μm]
J	1.1 to 1.4
H	1.5 to 1.8
K	2.0 to 2.4
L	3.0 to 4.0
M	4.6 to 5.0
N	7.5 to 14.5
Q	17 to 25
Z	28 to 40

Figure 1.2: Wavelength range of astronomical bands. [23]

Pushing the wavelengths for beam combination further into the infrared is important for example to extend the number of observable objects and to have a more favorable spectral density contrast between bright stars and cool companions, like exoplanets. Planck's law states that the spectral density  $B$  at the frequency  $\nu$  of a black body having the absolute temperature  $T$  is given by

$$B(\nu, T) = \frac{2h\nu^3}{c^2} \left( e^{\frac{h\nu}{k_B T}} - 1 \right)^{-1} \quad (1.4)$$

with the vacuum speed of light  $c$  and the Planck and Boltzmann constants  $h$  and  $k_B$ . The total spectral density of an exoplanet is a combination of its thermal emission and the light reflected from the parental star. The best spectral density contrast between star and companion is found in the mid-infrared.

The investigation of beam combination systems made from infrared transparent materials and the improvement of the instrumental properties of the beam combiners, as it was done in this work are crucial for the extension of the wavelength range in astronomical interferometry and the improvement of imaging resolution.

The interferometric combination of telescopes can be accomplished by combining the beams from several telescopes with a Fizeau or Michelson interferometer [24] in a cascade of beam splitters and lenses or using integrated optics (IO) components [25, 26] which use waveguide coupling in e.g. directional couplers and discrete beam combiners for the combination of the telescope light.

The concept of IO has been introduced to astronomical interferometry in 1999. [25] Integrated beam combiners can consist of evanescently coupled waveguides that combine the electromagnetic fields, either pairwise in a cascade of couplers and



beam splitters in order to distribute and combine the starlight simultaneously on all possible baselines [27], or all at once in straight waveguide arrays using discrete diffraction. It is a stable and compact technology [28] with a low sensitivity to vibrations and temperature fluctuations and a reduced setup complexity which also works as spatial filter. Spatial filtering improves the precision of the instrument, which is very important to handle atmospheric turbulence. Additionally, the only alignment needed is the launching of the electrical fields collected by the telescope into the device which reduces the requirement for maintenance. [26] These properties even give the possibility to use them in space-based experiments. [26]

IO components can be manufactured using 2D techniques such as photo lithography [28], ion exchange diffusion [29] and chemical etching [28, 30, 31]. [26] These IO processing methods are well mastered for near-infrared light and produce waveguides with losses lower than  $0.1 \frac{\text{dB}}{\text{cm}}$  [32], but they only produce IO components with a planar geometry. Ultrafast laser inscription (ULI) uses focused ultrafast laser pulses to induce a local refractive index change to the illuminated material and can be used to write waveguides. [33] This method allows the waveguide geometry to extend to the third dimension which can avoid waveguide crossings and therefore enables the manufacturing of more complex components. In addition, it is a rather simple manufacturing process compared to the 2D methods which allows fast prototyping and the extension to mid-infrared applications.

Depending on the laser intensities, there are different writing regimes for ULI waveguide writing. At low peak intensities a smooth refractive index change occurs which can be either positive or negative. In this regime, waveguides have been written into different materials, as fused silica [34, 35], phosphate glass [36], heavy metal oxide glass [37], chalcogenide glass [38] and halide glass [39]. Waveguides can be fabricated writing a single track of smooth positive refractive index change or by writing a depressed cladding with a reduced refractive index around unmodified material [40]. At medium high intensities an anisotropic refractive index and a related strong birefringence, generated by self-organizing nanogratings [41] has been reported for silica [42, 43], multicomponent silicate [44], fluoroaluminate glasses [45], as well as, crystals like tellurium-oxide [46] and sapphire [47] and even ceramics [48]. The stress field between the laser damaged tracks, generated in this regime, can form the waveguide [49] or a depressed cladding can be generated [50]. For high laser intensities the material suffers from voids and micro-explosions. [51]

A suitable material for ULI for mid-infrared IO applications is gallium lanthanum sulfide (GLS) glass. [52] ULI was first reported to be used on GLS substrates in 1996 [34]. GLS has a transparency window reaching up to about  $10 \mu\text{m}$ , is a non-toxic

material and has stable mechanical and thermal properties. Laser irradiation with suitable parameters can induce a positive refractive index change to the glass which enables waveguide manufacturing using ULI. [53, 54]

Pairwise IO beam combiners have experienced more development compared to all-in-one devices, so far. On sky and laboratory tests of up to 4 telescopes could be successfully performed. [17, 55] The GRAVITY instrument is a 2D pairwise 4-telescope beam combiner fabricated with photolithography. Though the cross talk is below 1%, an increasing number of telescopes will increase the cross talk and the complexity of the device. Integrated optics 3-telescope beam combiners that are extended to the third dimension were introduced to the field in 2012 by using ULI. [56] This manufacturing technique also allowed to fabricate all-in-one discrete beam combiners (DBC) [57] which are periodic 2D arrays of evanescently coupled single-mode waveguides and allow the combination of 3 [58, 59] or 4 [60, 61] telescopes.

The aim of this thesis is twofold. On one hand an interferometric device for the beam combination of 4 electromagnetic input fields should be designed and fabricated using ultrafast laser inscription in gallium lanthanum sulfide glass which includes the optimization of the waveguide writing parameters, the design and optimization of s-bends, the determination of the coupling strength of different evanescently coupled waveguide configurations and the management of laser induced stresses. On the other hand the laser induced structural modification should be studied using several independent experiments. Additionally, the Raman response of laser light traversing a waveguide should be investigated.

After this introduction, in Chapter 2 the manufacturing process of waveguides in glass using ultrafast laser inscription including the working physical mechanisms and the properties of the used gallium lanthanum sulfide glass are introduced before the fabrication of single-mode waveguides and the optimization of the writing parameters are described in detail. Subsequently, the structural changes during the laser writing process are examined by using scanning microscope images, Raman spectroscopy and polarimetry. Finally, the reduction of stresses induced by the manufacturing by means of annealing is characterized.

Chapter 3 focuses on the interferometry using IO components. The concept of evanescent waveguide coupling and IO are explained, extended by the determination of coupling and propagation coefficients for directional couplers. In the following sections the design and characterization of the zig-zag and ABCD discrete

beam combiners are described while solutions to the asymmetry and polarization dependence of waveguide arrays induced by stress fields are presented.

In Chapter 4, the measurement and simulation of the nonlinear Raman-Kerr effect in GLS glass in order to investigate the influence of the Raman effect to supercontinuum generation in GLS waveguides is described.

In the end of this thesis the content and the conclusions are summarized and an outlook is given.

# Chapter 2

## Waveguide manufacturing using ultrafast laser inscription

In this chapter the physical background of ultrafast laser inscription (ULI) is explained and gallium lanthanum sulfide (GLS) glass is introduced as a material suitable for the manufacturing of waveguides that operate at mid-infrared wavelengths. In order to find suitable parameters for waveguide manufacturing that can be used for the fabrication of photonic chips, the fabrication process of single mode waveguides in this material is explained, before the results of the waveguide characterization are presented. In the second part of the chapter the structural modifications caused by the induced laser energy are studied with the aim of understanding the properties of the GLS glass and the light guiding structures. Therefore, the results of scanning electron microscopy (SEM), Raman microscopy and polarimetric measurements are compared with the behavior of the mode field diameter (MFD) for waveguides written with different parameter sets. Finally, the effects of annealing on the waveguide properties are studied in order to reduce the effects of stress induced birefringence.

### 2.1 Ultrafast laser inscription in transparent materials

ULI was first performed in 1996 [34] and has since been object of numerous studies. It uses the nonlinear photoionization mechanisms, which cause a permanent refractive index change as a result of the exposure to high intensity light radiation.

The applications of ULI are versatile. It reaches from photo polymerization [62, 63] over the manufacturing of couplers [64–68], the production of Bragg gratings [69],

implementations in nano surgery [70–72] to material processing [73–75]. It could also be utilized for research on biosensors [76], linear and nonlinear optics [77], as well as quantum optics [78–80], 3D memory storage [81] and stellar interferometry [56]. More detailed information about the last application will be given in Section 3.3. Laser irradiation of transparent materials leads to nonlinear processes that confine the absorption process to the focal volume. Laser photons at wavelengths in the visible and mid-infrared regime provide not enough energy to trigger linear absorption. Instead, the mechanism that takes place in the material is nonlinear photoionization by multi-photon absorption, tunneling ionization and avalanche photoionization. In the multi-photon absorption (MPA) process multiple photons with the laser frequency  $\nu$  are absorbed simultaneously by a valence band electron which can be promoted to the conduction band. The photon number  $m$  has to be high enough to bridge the bandgap energy  $E_g$  ( $E_g < m h \nu$ ). The ionization rate is given by

$$W_{\text{MPA}} = \sigma_m I^m \quad (2.1)$$

with  $\sigma_m$  as the multi-photon absorption coefficient and  $I$  as the intensity. Additionally, direct band to band transitions are possible by photon tunneling when the electric field of the laser pulse is strong enough to deform the Coulomb well in which the valence electrons are located in a way that they are able to tunnel through the short barrier to get free.

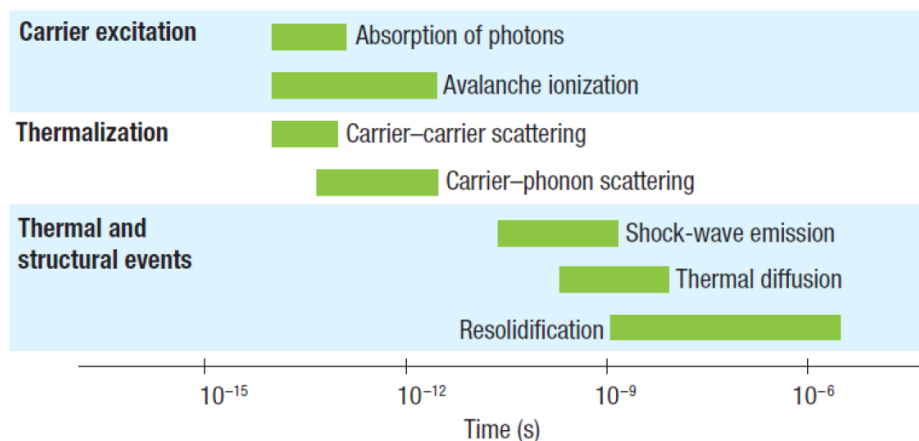


Figure 2.1: Timeline of laser-matter interaction [33].

When the induced energy of the conduction band electron exceeds the minimum conduction band level by more than the band gap energy impact ionization of valence band electrons by these conduction band electrons can occur. This mechanism may lead to an electron avalanche ionization, which has a higher contribution at longer

pulse lengths. A large number of electrons is ionized within tenths of picoseconds. The so generated large electron density leads to plasma formation which is followed by optical breakdown. [82]

The energy of the electrons can be transferred to the lattice at about one nanosecond after the initial irradiation and on a microsecond timescale the thermal energy transfers out of the focal volume. [33] When the laser has a high pulse repetition rate, the material has no time for relaxation because the time scale for the heat transfer is longer than for absorption. This way, the heat accumulates at the focal spot which can cause the glassy material to melt. On a microsecond timescale the material is resolidifying and leaves localized permanent structural modifications, such as refractive index enhancement [66] or depression [83].

At low pulse energies near the modification threshold a smooth refractive index change can be observed. [84] This can be used for waveguide writing in glasses. At higher energies the formation of periodic nanogratings orthogonal to laser polarization is reported. [43] For even higher pulse energies the pressures can overcome the Young's modulus which leads to a shockwave that leaves microexplosions or voids in the glass. [85] A refractive index change can be a result of material densification [86], induced stresses [87], color center formation [88] or elemental diffusion. [89] Confining the laser to a focal spot and scanning the focus through the transparent material by translating the sample allows waveguide writing with complex geometries. ULI is applicable to a various number of materials, e.g. glasses [34, 90], crystals [91, 92] and polymers [93].

The type and extent of the modification depend on laser parameters, such as pulse duration, laser wavelength and energy, repetition rate, as well as on material parameters, e.g. bandgap energy, thermal expansion coefficient etc. and the focusing parameters, such as numerical aperture (NA) of the objective. A positive refractive index change enables the possibility to write waveguide cores directly. A negative refractive index change, as it occurs in Nd:YAG single crystals [50] or Tm:ZBLAN glass, [40] requires writing the cladding instead of writing the waveguide core.

When the waveguide orientation is chosen to be parallel to the laser beam direction (longitudinal writing), the waveguides exhibit a circular cross section due to the Gaussian intensity profile of the laser beam. The main disadvantage is that this fabrication geometry needs objectives with a long working distance and low NA or writing parameters that allow filamentation in the material. [94] The transverse writing geometry is far more flexible and only limited in size by the range of the positioning system. [95] On the other hand, a high refractive index of the transparent material can cause spherical aberrations of the laser beam focus [82], which results

in a tear drop shaped cross section for a single track.

Multi-scans with overlapping irradiated zones can be used to shape the cross section geometry of the waveguide. The thermal history of the sample has a significant influence on the level of flexibility of the structures. [96] A short annealing leaves a less dense material. On the contrary an annealing over a longer period at the same temperature erases the effects of previous thermal treatment until complete material relaxation. The long term treated samples show a higher density and also a higher refractive index which makes it harder to achieve positive refractive index changes due to photocontraction by laser writing. [96]

## 2.2 Gallium lanthanum sulfide glass

For the search of earth-like exoplanets or protoplanetary disks, the mid-infrared wavelength range ( $5 - 30 \mu\text{m}$ ) is highly interesting. The spectral density contrast of the parent star and its exo-planet is lowest in the mid-infrared range, allowing data collection of planetary spectra with less effort compared to the operation in the visible wavelength regime. Also, the peak emission of planets in the habitable zone around solar-type stars and several bio-markers, e.g. water,  $\text{CO}_2$  or  $\text{O}_3$  are visible in this wavelength regime. [26] Accordingly, the transparency window is crucial for the selection of material for the photonic chips used in stellar interferometry. Other desired characteristics include low losses, which mean a low impurity level and a low number of defects, the resistance to thermal and mechanical stress, chemical stability and spatial homogeneity. Possible material candidates are (amorphous) chalcogenide glasses as  $\text{As}_2\text{Se}_3$  or  $\text{As}_2\text{S}_3$  with transparency windows up to  $12 - 16 \mu\text{m}$ , tellurium- or germanium-compositions which are transparent up to  $20 \mu\text{m}$  and (crystalline) silver-halide glasses and zinc selenide components with similar transparency ranges. [26]

GLS was first mentioned by Loireau-Lozac'h et al. in 1976. [52] It is a yellow/brown inorganic solid that belongs to the group of chalcogenide glasses. A chalcogenide glass contains two or more components including one or more of the chalcogenide elements S, Se, Te and elements of the IIIa to V subgroups of the periodic table. [97] GLS is the material of choice mainly because it has its transmission range in the infrared ranging from  $0.5$  to  $10 \mu\text{m}$ , laser irradiation induces a high positive refractive index contrast and it is a non-toxic alternative to arsenic-based glasses. [53]

The used samples were produced by ChG Southampton Ltd in the United Kingdom. Referring to the specifications of the company the glass composition is 50wt%

lanthanum (III) sulfide and 50 wt% gallium (III) sulfide. [98] The powdered materials are melted in an argon atmosphere for 24 h at  $1150^{\circ}\text{C}$  and rapidly cooled at  $20 \frac{\text{K}}{\text{min}}$  to avoid crystallization. Afterwards it is annealed at  $500^{\circ}\text{C}$  for 6 h (below the crystallization temperature) to enable a relaxation of the developed stresses to a stable state. Finally the glass is cut into substrates with the size of  $1 \times 10 \times 50 \text{ mm}^3$ . [99]

GLS has a melting point of  $842^{\circ}\text{C}$ , its glass transition temperature is at  $560^{\circ}\text{C}$  and material crystallization occurs at temperatures higher than about  $720^{\circ}\text{C}$ . The specific density is stated to be  $4.04 \frac{\text{g}}{\text{cm}^3}$ . [54, 99] In the glassy phase GLS is a semiconductor with a band gap of 2.6 eV (475 nm). Contrary to crystals, glasses do not have a long range order but instead a short range order of certain structural units can be observed.

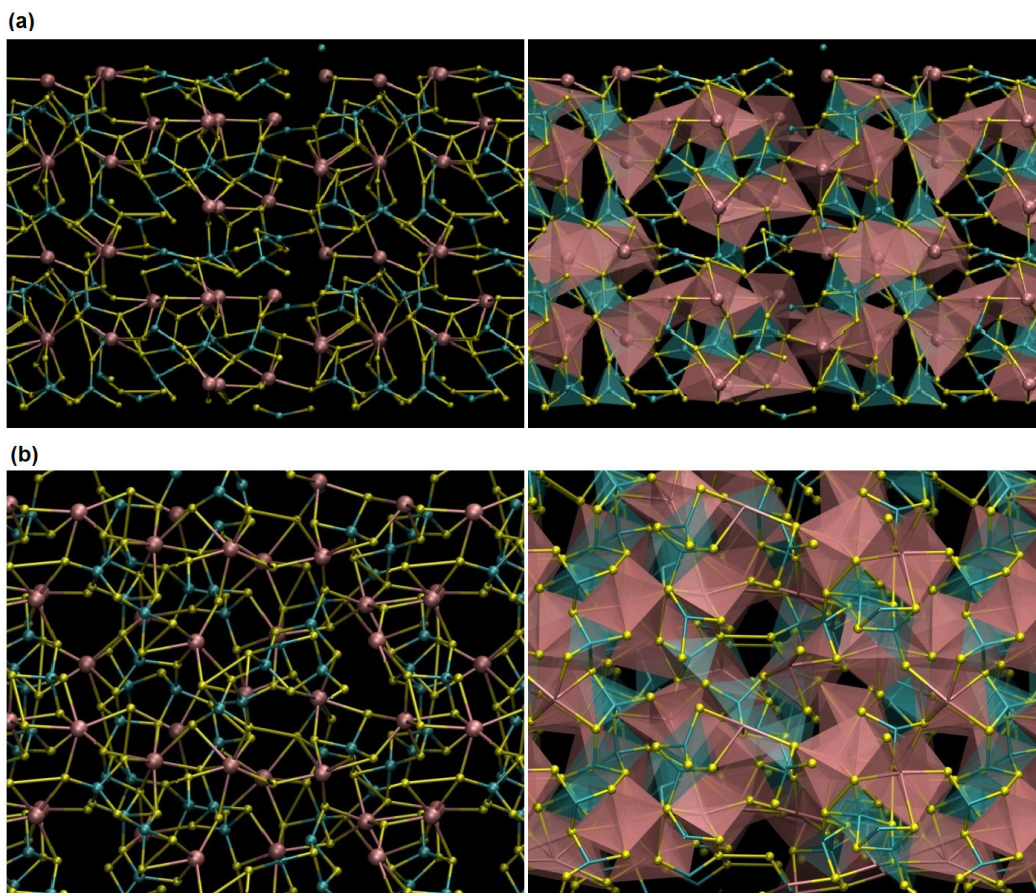


Figure 2.2: (a) Initial structure of the GLS at the first stage of the simulation. (b) Final structure of GLS in equilibrium state. Images created by Gloria Tabacchi at the DSAT-Università Insubria (Como, Italy). Left: ball and stick image. Right: polyhedra image. Atom colors: La and LaS<sub>8</sub> polyhedra - red, Ga and GaS<sub>4</sub> tetrahedra - green, S - yellow.



Ab initio molecular dynamics simulations of the GaLaS<sub>3</sub> glass with a composition 50% GaS<sub>3</sub> and 50% LaS<sub>3</sub> [54] was performed by Gloria Tabacchi at the DSAT-Università Insubria (Como, Italy). A simulation cell that matches the specific density of  $4.04 \frac{\text{g}}{\text{cm}^3}$  was built starting with the  $\beta$ -phase of the GaLaS<sub>3</sub> crystal. [100] First the melting of the structure at a temperature of 1600 K was simulated in order to obtain a liquid phase which could be cooled gradually in the second step to an equilibrium at room temperature.

The obtained glass structure is a disordered network of Ga-centered tetrahedra and La-centered polyhedra of S atoms. Gallium is essentially bonded to 4 sulfur atoms while the lanthanum is coordinated to 6, 7 or 8 sulfur atoms with the average coordination number of 7.5 which is in line with the literature [101]. A closer look to the glass structure reveals that S-S bonds are very uncommon in the final glass and the density distribution is not constant at all points in the structure.

The resulting average of the interatomic distances from the simulated structure are: 2.85 Å for Ga-Ga, 4.46 Å for La-La, 3.56 Å for S-S, 3.68 Å for Ga-La, 2.17 Å for Ga-S and 2.92 Å for La-S. The results for the initial structure with a still observable crystalline structure (a) compared with the final glass structure obtained by the simulation with no long range order (b) are shown in Fig. 2.2.

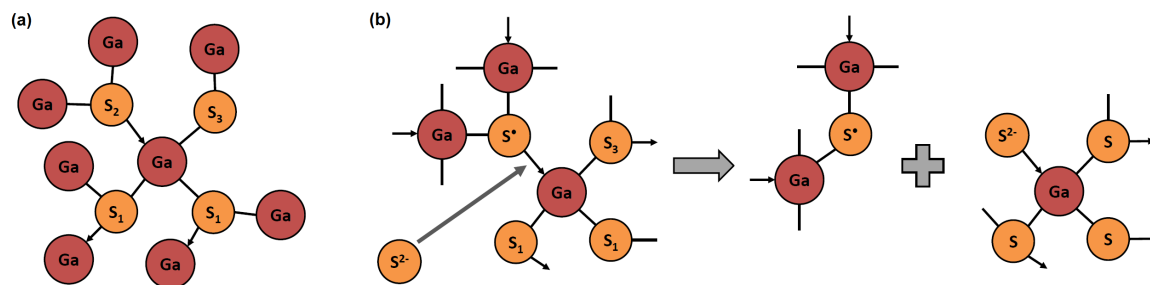


Figure 2.3: (a) Structure of the covalent gallium environment of crystalline Ga<sub>2</sub>S<sub>3</sub>. (b) Ionic cavity formation after adding La<sub>2</sub>S<sub>3</sub> [102].

The GaS<sub>4</sub> units act as glass forming units and the La-S appears to be the glass modifier. Network forming elements form an interconnecting network of polyhedra, while the network modifiers fill in the empty spaces in between. [103] In the crystalline state sulfur atoms are placed at corners of a tetrahedra with an La or Ga atom in the center. Ga<sub>2</sub>S<sub>3</sub> includes two sulfur atoms that form two covalent bonds and one dative bond to three gallium atoms. Another sulfur atom is bound to only two gallium atoms. This identifies it as a bridging atom. Introducing La<sub>2</sub>S<sub>3</sub> to the structure adds an S<sup>2-</sup> anion that links to a Ga-Atom by breaking the dative Ga-S bonds. This process is preserving the tetrahedral structure of the sulfur compound

but the previously tri-coordinated S-atom becomes a di-coordinated bridging atom. [99, 102, 104]

To gain information about the dispersion of the material the refractive index at different wavelengths have to be identified. GLS has a high refractive index of 2.31 at  $3.39 \mu\text{m}$ . A measurement of the refractive indices over several wavelengths was performed by VITRON Spezialwerkstoffe GmbH, Jena with an IR refractometer, see Fig. 2.4 (a), in order to extend the measurement of the known data [105] which already ends at a wavelength of  $1.7 \mu\text{m}$  and therefore does not cover the range in which the later fabricated waveguides should operate (up to  $3.4 \mu\text{m}$ ).

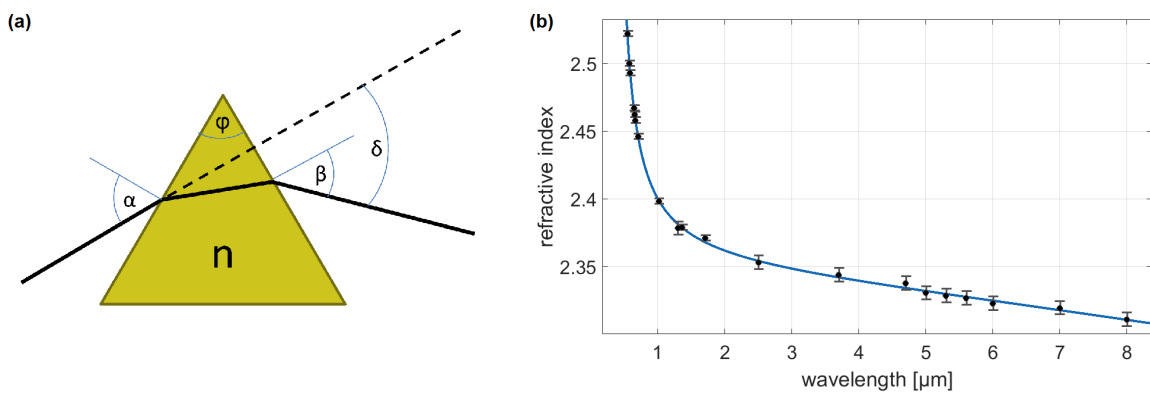


Figure 2.4: (a) Schematic image of the refractometric measurement. (b) Refractive index measurement. Values taken from measurements by VITRON Spezialwerkstoffe GmbH and [105].

A GLS prism is illuminated with light of different wavelengths with the incident angle  $\alpha$  after determining the prism angle  $\phi$  by measuring the reflection angles on both prism planes. The incoming beam is refracted by the angle  $\delta$  which is depending on  $\alpha$ ,  $\phi$  and the refractive index of the GLS prism (assuming the refractive index of air  $n_{\text{air}} = 1$ ). The refracted beam angle is measured with a goniometer at different wavelengths. To facilitate the measurement and calculation the incident angle is chosen to be orthogonal. The equation

$$n = \sin \left( \frac{\phi + \delta}{\sin \phi} \right) \quad (2.2)$$

can be used to derive the refractive index of the material. [106] The results from this experiment were added to the values from the literature [105] and plotted in Fig. 2.4 (b). These two datasets exhibited an offset in refractive index of 0.03 and therefore had to be aligned by adding a constant value to the measurement data points make a proper fit possible. A Sellmeier-fit of the obtained values resulted in a refractive

index of (for  $\lambda$  in  $\mu\text{m}$ )

$$n^2(\lambda) = 1 + \frac{4.535 \cdot \lambda^2}{\lambda^2 - 0.04545} + \frac{56.71 \cdot \lambda^2}{\lambda^2 - 1.729 \cdot 10^4} \quad (2.3)$$

When an electromagnetic wave traverses a single mode waveguide it experiences different types of dispersion. Amongst others, the material refractive index (material dispersion), the field distribution over the waveguide radius (geometrical dispersion), the polarization in birefringent materials (polarization dispersion) and nonlinear effects can affect the refractive index for light at different wavelengths. Nonlinear effects occur at high laser intensities in nonlinear materials. The refractive index becomes intensity dependent and leads to effects such as self-phase modulation or soliton generation.

There are two domains of dispersion. Normal dispersion is existent, if the derivative of the refractive index with respect to the frequency of the light is positive ( $\frac{dn}{d\omega} > 0$ ).

Anomalous dispersion occurs for ( $\frac{dn}{d\omega} < 0$ ). [107]

The zero dispersion wavelength (ZDW) is the wavelength at which the dispersion equals zero. It can be derived from Eqn. 2.3. For the manufactured waveguides it is found to be  $ZDW = 3.696 \mu\text{m}$  which is close to the operating wavelength of the mode characterization setup ( $3.39 \mu\text{m}$ ).

Transmission losses in optical glasses generally originate from absorption during electric transitions induced by a photon with sufficient energy, photon absorption and scattering. Due to the introduced interface between waveguide and bulk a high contribution to waveguide losses is given by scattering. The high hyperpolarisability of the sulfide ion leads to a large third order nonlinear refractive index that is about 100 times higher than that of  $\text{SiO}_2$ . [108]

## 2.3 Single mode waveguides in GLS

A first step towards the manufacturing of photonic chips for mid-infrared stellar interferometry is to find a way of writing single mode waveguides in the chosen material (GLS glass).

A waveguide is a light confining structure for one (slab waveguide) or two dimensions (channel waveguide or fiber) which uses the effect of total internal reflection for light guiding. It consist of a waveguide core with the refractive index  $n_{\text{core}}$  in which the light is transported and a cladding with a lower refractive index  $n_{\text{cladding}}$  which is necessary to obtain total reflection at the interface. All light beams that are

injected to the waveguide at an angle that is smaller than the critical angle

$$\cos \theta_{\text{crit}} = \frac{n_{\text{cladding}}}{n_{\text{core}}} \quad (2.4)$$

can be guided inside the waveguide core. The corresponding cone of guidable rays has an numerical aperture of

$$\text{NA} = n_{\text{core}} \sin \theta_{\text{crit}} = \sqrt{n_{\text{core}}^2 - n_{\text{cladding}}^2} \quad (2.5)$$

When the value of the waveguide diameter  $d$  approaches the wavelength, ray optics is not valid. For a waveguide the propagation equations have discrete solutions which are referred to as modes. A single mode waveguide is defined to guide only one mode. A mode is a field that has a constant transverse distribution along the waveguide axis. [107] The number of transverse electric (TE) modes guided in a 2D waveguide can be approximated for cylindrical waveguides as

$$M \sim \frac{\pi^2 d^2}{\lambda_0^2} \text{NA}^2 \quad [107] \quad (2.6)$$

The fundamental mode is nearly Gaussian. The  $\frac{1}{e}$ -diameter of the mode is referred to as the mode field diameter (MFD).

After ULI turned out to be a suitable method for waveguide writing the search for the optimal parameter set to write single mode strip waveguides is necessary. A sketch of the used setup can be seen in Fig. 2.5 (a).

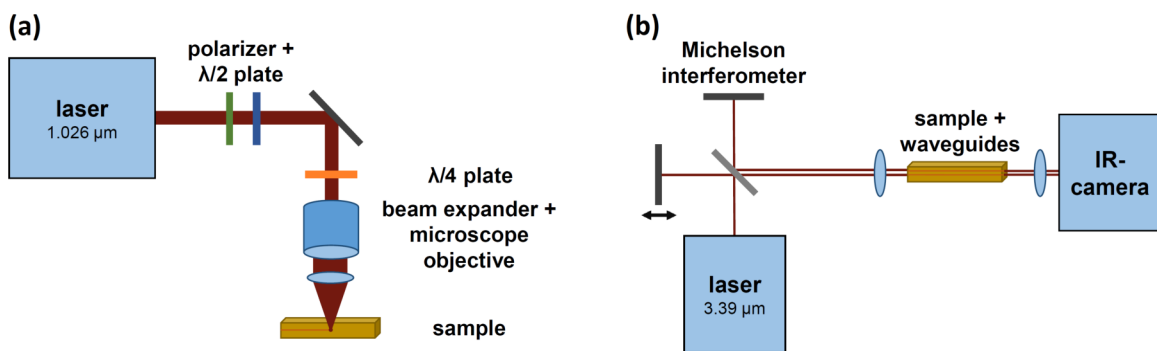


Figure 2.5: (a) Laser writing setup. (b) Characterization setup.

The laser source is an amplified PHAROS Yb:KGW laser at a wavelength of  $\lambda = 1026 \text{ nm}$ . The laser provides a pulse train with pulse durations between 190 fs and 10 ps at repetition rates between 200 kHz and 1 MHz. For fine tuning of the laser power, the setup contains a rotatable  $\frac{\lambda}{2}$ -plate and a linear polarizer. To avoid the formation of

nanogratings [43] circular polarization of the writing beam is ensured by the use of a  $\frac{\lambda}{4}$ -plate inserted in the light path. An additional 1:2 beam expander makes sure that the entrance pupil of a NA = 0.35 microscope objective is illuminated uniformly. The beam is focused 200  $\mu\text{m}$  underneath the polished surface of the sample, which is placed on a moveable computer-controlled nano-positioning stage allowing the positioning with a precision of about 200 nm and speeds up to 2  $\frac{\text{cm}}{\text{s}}$ . [109, 110]

For characterizing the mode fields transmitted by the manufactured waveguides and to perform the characterization of the integrated optics components in Chapter 3, a setup as in Fig. 2.5 (b) was built. A helium-neon laser ( $\lambda = 3.39 \mu\text{m}$ ) is used as infrared light source. A linear polarizer allows the control of the input polarization state. The laser beam is introduced to a Michelson interferometer, which allows splitting the beam and delaying one partial beam by a movable mirror. The two partial beams can then be focused by a lens ( $f = 50 \text{ mm}$ ) to two different spots on the input face of the glass sample. The sample is attached to a 3D translation stage with an additional tip-tilt facility, which opens the possibility to position the waveguide parallel to the beam. By this mean the beam is focused to the polished entrance face of the waveguide. The transmitted mode is reimaged on a FLIR-A6700sc infrared camera.

The horizontal and vertical mode field diameter is measured as the  $\frac{1}{e}$ -width of the Gaussian intensity profile observed by the camera.

First single scan experiments showed visible tracks in microscopic images with 20 times magnification for 7 to 21 mW and writing speeds between 0.25 and 6  $\frac{\text{mm}}{\text{s}}$ . The repetition rate was set to 500 kHz and the pulse duration to 400 fs. The cross section of these modifications extend to 20  $\mu\text{m}$  in height and 5  $\mu\text{m}$  in width but the refractive index change is not high enough to couple enough light at 3.39  $\mu\text{m}$  wavelength into the waveguide. Increasing the laser power up to 130 mW could increase the height to 100  $\mu\text{m}$  and the width to 18  $\mu\text{m}$ . The teardrop shaped cross section is visible, see Fig. 2.6 (a), top. It arises due to spherical aberrations induced by the plane surface of the high index GLS glass. [56]

The irradiated material is able to guide light but due to the high aspect ratio the output mode showed single mode behavior in horizontal direction but it is multi-mode in the vertical direction. A variation of the pulse duration shows the smallest aspect ratio of 4 for a single scan at 1  $\frac{\text{mm}}{\text{s}}$  and 130 mW for 400 fs. Beam shaping with a slit perpendicular to the direction of writing in front of the objective, which changes the shape of the beam focus in one dimension in order to write waveguides with a more circular cross section [111] did also not give satisfactory results. In this case, the microscopic image of the waveguide cross section showed indications of

filamentation of the laser beam.

To receive waveguides that are able to support a single mode at a wavelength of  $3.39 \mu\text{m}$  with nearly circular mode fields, the multi-pass writing technique was used which allows tailoring the refractive index contrast and the waveguide cross section. According to the literature [112], 21 overlapping lines, with each line shifted horizontally by 300 nm, form a rectangularly shaped waveguide. The cross sections of the waveguides are shown in Fig. 2.6 (a), bottom.

A parameter scan of the stage translation speed and the laser power on sample for a repetition rate of 500 kHz and a pulse duration of 400 fs with a NA of the focusing system of 0.35, identified a writing window for single mode waveguides between 1 and  $8 \frac{\text{mm}}{\text{s}}$  writing speed and 30 and 50 mW laser power, excluding 1 and  $2 \frac{\text{mm}}{\text{s}}$  for 45 mW and 1 to  $4 \frac{\text{mm}}{\text{s}}$  for 50 mW for the reason of multimode guiding and 6 to  $8 \frac{\text{mm}}{\text{s}}$  for 30 mW, because waveguides written with these parameters are not able to guide any light for a probe wavelength of  $3.39 \mu\text{m}$  (see, Fig. 2.6 (b)).

A pulse length scan for multi-scan waveguides from 200 fs to 1 ps for  $1 \frac{\text{mm}}{\text{s}}$  and 40 mW showed the smallest MFD at 500 fs. The waveguides that were manufactured with the parameters 40 mW laser power,  $1 \frac{\text{mm}}{\text{s}}$  translation speed, a pulse length of 500 fs and 500 kHz repetition rate with a NA of 0.35 exhibit the minimal measured mode field diameter for  $\lambda = 3.39 \mu\text{m}$  of  $18.6 \times 22.1 \mu\text{m}^2$ . These waveguides have a core cross section of about  $8 \times 17 \mu\text{m}^2$ .

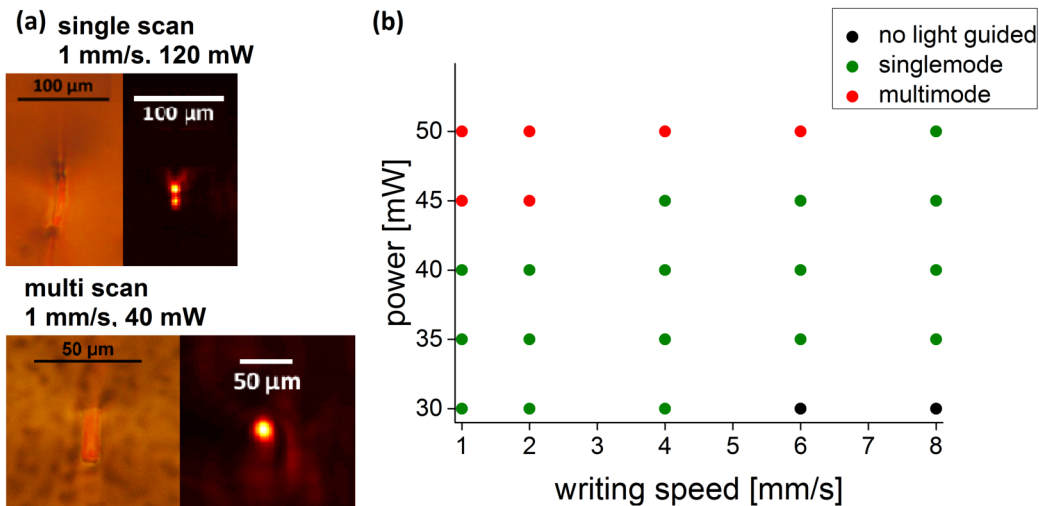


Figure 2.6: (a) Microscope images and supported modes at  $3.39 \mu\text{m}$  of a single scan waveguide written with  $1 \frac{\text{mm}}{\text{s}}$  and 120 mW (top) and multi-scan waveguide written with  $1 \frac{\text{mm}}{\text{s}}$  and 40 mW with 21 lines separated by 300 nm (bottom). [109] (b) Mode numbers of probed multi-scan waveguide parameter sets for  $\lambda = 3.39 \mu\text{m}$ .

A change of the NA of the focusing system to 0.45 did not decrease the smallest possible MFD. The smallest MFD for a NA of 0.45, a laser power of 25 mW and a writing speed of  $1 \frac{\text{mm}}{\text{s}}$  was measured to be  $19.4 \times 23.4 \mu\text{m}^2$ . The reproducibility test, which compared the MFD for 5 waveguides written with an identical parameter set, showed a standard deviation of  $\sim 2\%$  for the horizontal and 5% for the vertical MFD.

For estimating the propagation losses there are several possible techniques, e.g. the scattering technique [113] which is limited for our waveguides due to the small amount of scattered light, prism coupling [114] which cannot be used for buried waveguides and the Fabry-Perot resonance method [115] which needs a heating facility in the characterization setup. [103] For obtaining the propagation losses of the waveguides in GLS the cut-back method was used. [116, 117] Waveguides with identical writing parameters were written in two 50 mm long samples. One sample kept its length of 50 mm and the other one was cut into 5, 14 and 30 mm long pieces. The throughput powers for all four samples was measured and the propagation loss of about  $(0.91 \pm 0.35) \frac{\text{dB}}{\text{cm}}$  obtained.

The comparison of the MFDs for waveguides written with different parameters showed interesting results.

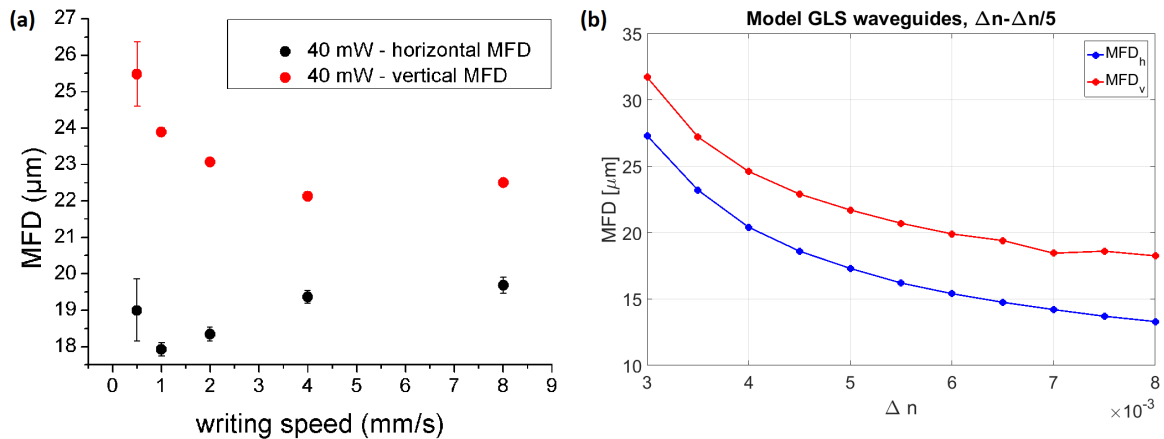


Figure 2.7: (a) MFD at  $3.39 \mu\text{m}$  of waveguides written with a laser power of 40 mW and varying translations speeds. (b) Simulation of horizontal and vertical MFD over  $\Delta n$  for a wavelength of  $3.39 \mu\text{m}$ . Both for vertical input polarization.

A plot of the horizontal and vertical MFD over the writing speed for a laser power of 40 mW is shown in Fig. 2.7 (a). The minimal horizontal MFD can clearly be distinguished for  $1 \frac{\text{mm}}{\text{s}}$ . The slope change at this point could indicate a different resulting structure after laser irradiation for different writing speeds. Smaller refractive index changes lead to larger MFD. Therefore, there might be a different

structural effect responsible for translation speeds higher and lower than  $1 \frac{\text{mm}}{\text{s}}$ , that is leading to the change in trend for the refractive index change. Slower sample translation speeds mean a higher amount of energy density absorbed by the glass.

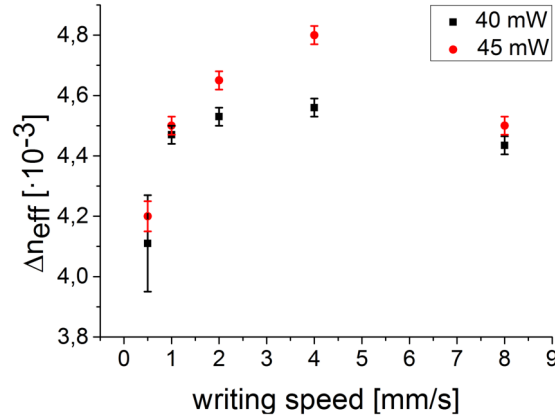


Figure 2.8: Refractive index difference  $\Delta n_{\text{eff}}$  of waveguides written with laser powers of 40 mW and 45 mW and varying translation speeds.

A refractive index contrast of  $\Delta n_{\text{eff}} \sim 4 \cdot 10^{-3}$  to  $5 \cdot 10^{-3}$  could be derived from beam propagation simulations done with the RSoft mode solver software, see Fig. 2.8. For the simulation of a 7 mm long waveguide with a rectangular waveguide cross section of  $8 \times 17 \mu\text{m}^2$ ,  $\Delta n$  of the waveguides was set to  $\frac{4}{5}\Delta n$  of the material refractive index and the refractive index of surrounding material with the dimensions of  $12 \times 25.5 \mu\text{m}^2$  was set to  $-\frac{1}{5}\Delta n$ . The reason for the use of this model describing the waveguide cross section is a stress induced negative refractive index change surrounding the waveguides that was observed in the measurements shown in Section 2.6 (Fig. 2.25). The MFD over refractive index change was simulated to compare it to the MFD measurements, see Fig. 2.7 (b). Increasing the translation speed leads to a larger MFD and a smaller  $\Delta n$ .

To match the diameter of the input mode to the waveguide size a taper can be useful. To test the influence of the launching mismatch to the transmitted power the translation speed of the sample was changed along the waveguide length. Starting from different velocities between  $1$  and  $8 \frac{\text{mm}}{\text{s}}$  at a laser power of 40 mW and reducing linearly the translation speed along the length until the final velocity of  $1 \frac{\text{mm}}{\text{s}}$  resulted in waveguides that change their size uniformly from one side of the sample to the other. For an optimal input coupling the MFD matching between input beam and waveguide input face is necessary. The MFD of the focused He-Ne laser is  $32.5 \mu\text{m}$ . The throughput power of the tapered waveguides were measured. The transmitted power for  $2 \frac{\text{mm}}{\text{s}}$  to  $1 \frac{\text{mm}}{\text{s}}$  writing speed over a length of 10 mm is the highest of the



tested tapers, see Fig. 2.9.

For a better comparability, the MFD values used in this section express the values of the output modes received with linear vertical input polarization.

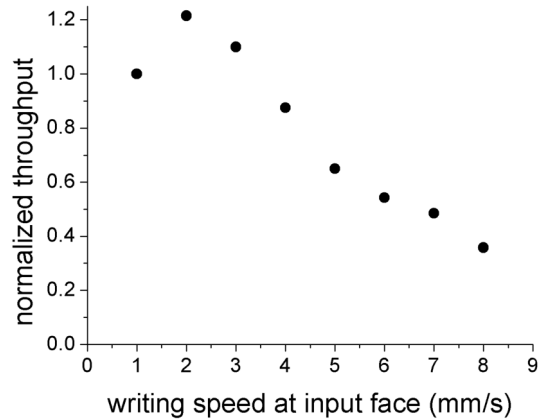


Figure 2.9: Throughput of differently tapered waveguides normalized to the untapered waveguide written with a writing speed of  $1 \frac{\text{mm}}{\text{s}}$  at 40 mW laser power.

## 2.4 Structural modifications induced by femtosecond laser irradiation

### 2.4.1 Scanning electron microscopy

For the investigation of the presence of nanostructures in laser irradiated GLS glass, scanning electron microscopy (SEM) is a helpful tool. It allows the view to the surface of the waveguide cross section with a resolution at a nanometer scale.

Electrical non-conducting materials, such as the investigated GLS glass sample, have to be coated for example with a carbon layer to avoid charge deposition on the sample which would lead to distortions of the electron beam and therefore an inaccurate image. [118]

Waveguides with laser powers of 40 and 45 mW and writing speeds of 0.5, 1, 2, 4 and  $8 \frac{\text{mm}}{\text{s}}$  at a pulse repetition rate of 500 kHz and a pulse length of 500 fs were written into one sample. Afterwards, the sample input face was polished and chemically etched for 1 h in 1-molar (1 mol per liter) hydrochloric acid (HCl).

The SEM images for waveguides fabricated with a laser power of 40 mW and sample translating speeds of 0.5, 1 and  $8 \frac{\text{mm}}{\text{s}}$ , as well as 45 mW and  $2 \frac{\text{mm}}{\text{s}}$  have been taken with the FEI Helios NanoLab and displayed in Fig. 2.10. The cross sections of the

waveguide that is used in the interferometric devices (40 mW and  $1 \frac{\text{mm}}{\text{s}}$  for 21 scans with a line separation of 300 nm) shows a very smooth surface without any hint of irregularities. Reducing the deposited energy per volume by accelerating the translation speed to  $8 \frac{\text{mm}}{\text{s}}$  exhibits also a smooth surface with vertical lines which show that the scan distance of the laser writing for this parameter set is too high. The unmodified material in between the scan lines lower the effective refractive index difference for waveguides written with this parameter set.

Reducing the scan speed to  $0.5 \frac{\text{mm}}{\text{s}}$  and therefore increasing the deposited energy has a drastic effect on the surface smoothness. Small irregular structures can be distinguished that indicate a different structure than for the areas that were scanned faster. The same behavior can be seen for increasing the laser power to 45 mW.

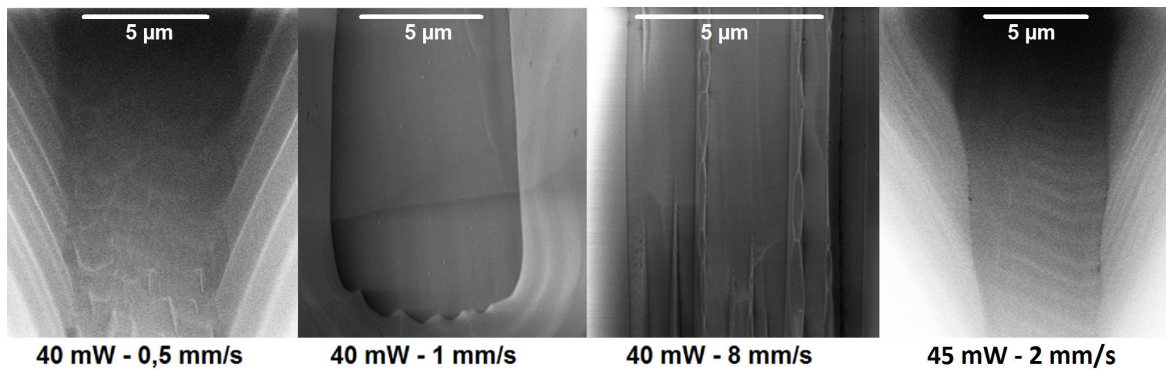


Figure 2.10: SEM images of the cross sections of waveguides written with different parameters.

The smooth surface of waveguides written with less deposited energy indicates a glassy structure that is not too different from the bulk structure. The rough structures for higher laser powers or slower writing speeds could originate from crystallization seeds that start to form at a higher temperature ( $\sim 720^\circ \text{C}$ ) [99] or defects due to laser induced nanocracks [85].

A test etching for 20 h showed a formation of conical holes with depths and diameters depending on the used writing parameters, see Fig. 2.11 (a, b). For 40 mW laser power and  $0.5$  to  $4 \frac{\text{mm}}{\text{s}}$  translation speed the holes have approximately the same depths of  $85$  to  $100 \mu\text{m}$ ,  $8 \frac{\text{mm}}{\text{s}}$  writing speed shows comparably shallow cavities of  $13 \mu\text{m}$  depth. The etching rate decreases more drastically for faster writing speeds than  $4 \frac{\text{mm}}{\text{s}}$  with a slope of  $-2.84 \cdot 10^{-7}$  (compared to  $0.43 \cdot 10^{-7}$  for slower writing)<sup>1</sup>. For 45 mW and  $0.5$  to  $2 \frac{\text{mm}}{\text{s}}$  the grooves are much deeper with a depth of  $200$  to  $215 \mu\text{m}$ ,  $175 \mu\text{m}$  for  $4$  and  $114 \mu\text{m}$  for  $8 \frac{\text{mm}}{\text{s}}$ . The slope of the etching rate is  $-0.16 \cdot 10^{-7}$

<sup>1</sup>The units have been canceled out:  $\frac{\mu\text{m}/\text{h}}{\text{mm}/\text{s}} = \frac{1}{3600} \cdot 10^{-3} \frac{\text{mm}/\text{s}}{\text{mm}/\text{s}} = \frac{1}{3.6} \cdot 10^{-6}$

for velocities slower than at  $2 \frac{\text{mm}}{\text{s}}$  and  $-2.16 \cdot 10^{-7}$  for higher writing speeds.<sup>2</sup> This means, laser modified material that has experienced a higher amount of absorbed energy has a lower resistance to HCl etching.

Assuming linear etching the etching rates differ between parameter sets and lie between  $0.7$  and  $4.9 \frac{\mu\text{m}}{\text{h}}$  for  $40 \text{ mW}$  laser power and between  $5.7$  and  $10.8 \frac{\mu\text{m}}{\text{h}}$  for a laser power of  $45 \text{ mW}$ . For details see Fig. 2.11 (c). The large gap between the etching rates for  $40 \text{ mW}$  and  $45 \text{ mW}$  laser power at  $0.5$  to  $2 \frac{\text{mm}}{\text{s}}$  writing speed can be the result of a phase transition that is taking place in between the parameter values. The hole diameters exhibit a similar dependency. The diameter of the etched cones at the surface is approximately  $50$  to  $53 \mu\text{m}$  for  $40 \text{ mW}$  and  $0.5$  to  $8 \frac{\text{mm}}{\text{s}}$ , about  $67 \mu\text{m}$  for  $45 \text{ mW}$  and  $0.5$  to  $2 \frac{\text{mm}}{\text{s}}$ ,  $63 \mu\text{m}$  for  $4 \frac{\text{mm}}{\text{s}}$  and  $57 \mu\text{m}$  for  $8 \frac{\text{mm}}{\text{s}}$ .

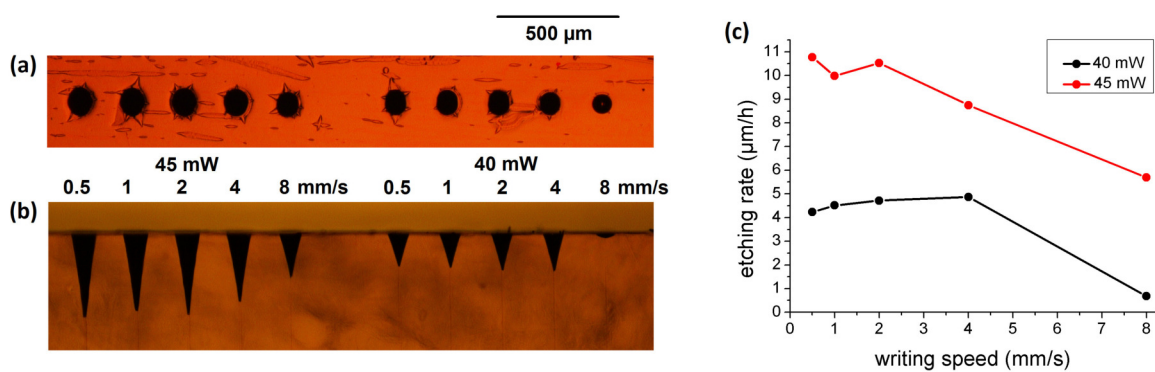


Figure 2.11: (a) Cross sections of waveguides manufactured with different parameters and etched with 1-molar HCl for 20h. (b) Side view of the conical holes resulting from the chemical etching process. (c) Overview of hole diameters and depths after 20 h of etching time.

These observations lead to the assumption that higher absorbed laser energies and therefore higher induced temperatures during the writing process results in a different final structure of the glass than lower deposited energies. Structural characteristic as e.g. nanocracks, crystallization or other reformation of atomic bonds make the surface profile rougher and the material more vulnerable to chemical etching. However, waveguides fabricated with a lower laser energy density seem to have a structure close to the structure of the bulk material and are therefore less susceptible to the etching acid. The slope of the etching rate changes drastically at  $4 \frac{\text{mm}}{\text{s}}$  for  $40 \text{ mW}$  and at  $2 \frac{\text{mm}}{\text{s}}$  for  $45 \text{ mW}$ , which indicates a different structural behavior for high and low deposited energies by the ULI process.

<sup>2</sup>see Fn. 1

### 2.4.2 Raman spectroscopy

More insight to the structure of the GLS glass and information about the structural changes that occur during laser irradiation is given by Raman microscopy.

The Raman effect results from inelastic photon scattering when a material is illuminated typically with a laser at a frequency  $\nu$ .

Raman scattering induces Stokes and anti-Stokes lines. In Stokes Raman scattering the involved atoms or molecules are excited to a virtual state and then relax to a level that is higher than the ground state. This way the particles are excited into higher vibrational or rotational energetic states while the scattered photons are reemitted with lower energy which results in a decrease of  $\nu$ . Anti-Stokes Raman scattering is the result of the absorption of photon energy by exciting the atom or molecule from a virtual state to an excited state followed by the relaxation to the energetic ground level. The particle reduces its energy and the emitted photon has a higher frequency than the incident photon.

The Raman spectrum is the spectrum of the scattered photons. It shows the intensity of the scattered light as a function of its frequency difference to the incident photons in wavenumbers. Stokes and anti-Stokes peaks are located symmetrically around the excitation frequency, but the intensities differ depending on the population of the initial states of the particles in the material. The spectrum depends on the molecular structure of the irradiated material allowing it to be used for material identification and analysis.

The Raman peak position indicates the atomic bond types that show altered vibrational or electronical states, the peak width shows the distribution of the bond angles and the peak height gives information about the number of bonds of a kind. [119, 120]

#### Laser modification in gallium lanthanum sulfide glass

Structural changes due to laser irradiation in  $\text{SiO}_2$  [121–123] and germanium based chalcogenide glasses [96, 124] have been revealed by Raman microscopy. A comparison of Raman spectra from irradiated and non-irradiated GLS showed no significant variations, so far [125, 126] but the Raman modes contributing to the bulk spectrum have been investigated. [127]

The following measurement results were obtained with the RENISHAW inVia Raman Microscope. The cross section of waveguides written with several parameter sets was polished and a line scan over the waveguide cross section could be performed.

The resolution of the scan was  $1 \mu\text{m}$ . The bulk and waveguide spectra could be clearly distinguished by the change in Raman intensity. The Raman intensity over the wavenumbers and the distance along the line for an excitation wavelength of  $532 \text{ nm}$  is displayed in Fig. 2.12 (a). The two main features of the Raman spectrum are a strong broad peak from  $260$  to  $445 \text{ cm}^{-1}$  with two side peaks in the range from  $95$  to  $260 \text{ cm}^{-1}$  and a broad medium strong band from  $445$  to  $900 \text{ cm}^{-1}$  in which the bands indicating Ga and La are overlapping.

A cumulative Gaussian peak fit of the spectrum can reveal differences in peak heights, peak position and FWHM (full width at half maximum) of the several peaks. The four peaks with colors red ( $(135 \pm 59) \text{ cm}^{-1}$ ), green ( $(208 \pm 84) \text{ cm}^{-1}$ ), blue ( $(333 \pm 117) \text{ cm}^{-1}$ ) and turquoise ( $(644 \pm 484) \text{ cm}^{-1}$ ) have been fitted respectively with a Gaussian function, see Fig. 2.12 (b).

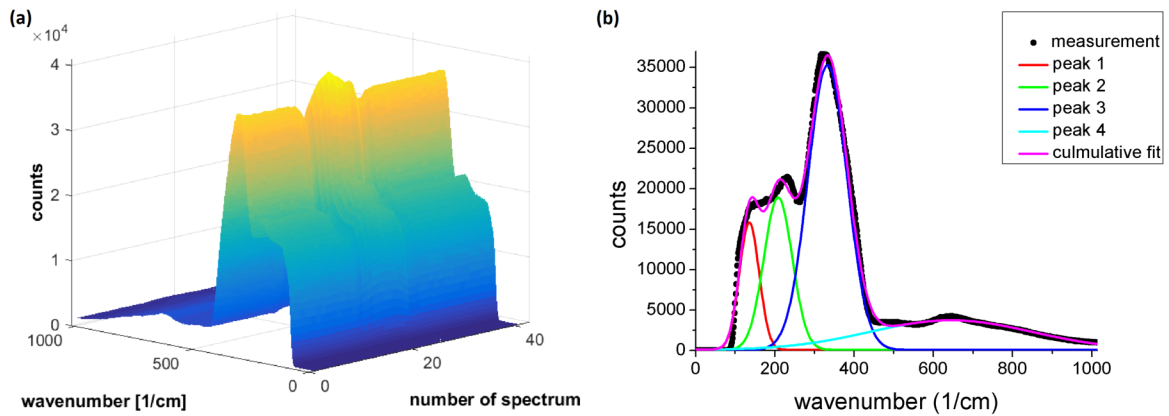


Figure 2.12: (a) Raman line scan: Raman intensities over wavenumbers and spectrum position. (b) Deconvolution of 4 peaks of one spectrum.

The potential origin of the shoulder (peak 1 and 2) can be due to stretching vibrations of the  $\text{GaS}_4$  tetrahedra ( $135$  and  $210 \text{ cm}^{-1}$ ) overlapping with  $\text{GaS}_4$  vibrations ( $141 \text{ cm}^{-1}$ ). At  $135$  and  $200 \text{ cm}^{-1}$  the vibrational modes of  $\text{La}_6\text{Ga}_{10/3}\text{S}_{14}$  could also have an effect to the side feature. Additionally,  $\text{LaS}_8$  breathing vibrations seem to have a contribution at  $210 \text{ cm}^{-1}$ . The main peak might be a superposition of  $\text{GaS}_4$  stretching vibration which has a Raman response at  $330 \text{ cm}^{-1}$  and  $\text{GaS}_4$  vibrations at  $329 \text{ cm}^{-1}$ . It can also originate in the bonds of  $\text{La}_{10/3}\text{Ga}_6\text{S}_{14}$  which have a peak at  $329 \text{ cm}^{-1}$  and also have a peak at  $142 \text{ cm}^{-1}$ . An overview is given by Tab. 2.13.

The subtraction of the fitted curve from the measurements revealed several residual peaks. The peaks at  $(171 \pm 12) \text{ cm}^{-1}$ ,  $(237 \pm 11) \text{ cm}^{-1}$ ,  $(310 \pm 12) \text{ cm}^{-1}$  and  $(398 \pm 14) \text{ cm}^{-1}$  have also been fitted with Gaussian functions.  $\text{GaS}_4$  stretching modes have a Raman peak at  $172 \text{ cm}^{-1}$  and can be responsible for the first fitted feature.

The residual peak at  $237\text{ cm}^{-1}$  can be a superposition of  $\text{GaS}_4$  stretching modes,  $\text{GaS}_4$  stretching modes and bonds in the  $\text{La}_6\text{Ga}_{10/3}\text{S}_{14}$  structure (all at  $233\text{ cm}^{-1}$ ). At  $307\text{ cm}^{-1}$  the  $\text{GaS}_4$  modes and at  $308\text{ cm}^{-1}$  modes originating from  $\text{La}_6\text{Ga}_{10/3}\text{S}_{14}$  can be distinguished in the residual spectrum, as well as the  $\text{LaS}_8$  breathing mode and the  $\text{GaS}_3$  stretching mode at  $310\text{ cm}^{-1}$ . Furthermore, contributing to the peak at  $398\text{ cm}^{-1}$  the  $\text{GaS}_4$  stretching mode appears at  $404\text{ cm}^{-1}$ .

peak / residuum	wave-number	refers to	source
residual peak	$102\text{ cm}^{-1}$	$\text{LaS}_8$ ( $95\text{ cm}^{-1}$ ) $\text{La}_6\text{Ga}_{10/3}\text{S}_{14}$ ( $104\text{ cm}^{-1}$ ) $\text{GaS}_4$ ( $106\text{ cm}^{-1}$ )	Lucazeau 1977 Lucazeau 1978 Nemec 2009
peak 1	$135\text{ cm}^{-1}$	$\text{GaS}_4$ ( $135\text{ cm}^{-1}$ ) $\text{La}_6\text{Ga}_{10/3}\text{S}_{14}$ ( $135\text{ cm}^{-1}$ ) $\text{GaS}_4$ ( $141\text{ cm}^{-1}$ ) m $\text{La}_{10/3}\text{Ga}_6\text{S}_{14}$ ( $142\text{ cm}^{-1}$ )	Lucazeau 1977 Lucazeau 1978 Lucazeau 1978 Nemec 2009
residual peak	$171\text{ cm}^{-1}$	$\text{GaS}_4$ ( $172\text{ cm}^{-1}$ )	Lucazeau 1977
peak 2	$208\text{ cm}^{-1}$	$\text{La}_6\text{Ga}_{10/3}\text{S}_{14}$ ( $200\text{ cm}^{-1}$ ) $\text{GaS}_4$ ( $210\text{ cm}^{-1}$ ) $\text{LaS}_8$ ( $210\text{ cm}^{-1}$ )	Lucazeau 1978 Nemec 2009 Nemec 2009
residual peak	$237\text{ cm}^{-1}$	$\text{GaS}_4$ ( $233\text{ cm}^{-1}$ ) $\text{La}_{10/3}\text{Ga}_6\text{S}_{14}$ ( $233\text{ cm}^{-1}$ )	Lucazeau 1977 Lucazeau 1978
residual peak	$310\text{ cm}^{-1}$	$\text{GaS}_4$ ( $307\text{ cm}^{-1}$ ) $\text{La}_{10/3}\text{Ga}_6\text{S}_{14}$ ( $308\text{ cm}^{-1}$ ) $\text{GaS}_4$ ( $310\text{ cm}^{-1}$ ) $\text{LaS}_8$ ( $310\text{ cm}^{-1}$ )	Lucazeau 1977 Lucazeau 1978 Lucazeau 1978 Lucazeau 1978
peak 3	$333\text{ cm}^{-1}$	$\text{GaS}_4$ ( $329\text{ cm}^{-1}$ ) $\text{La}_{10/3}\text{Ga}_6\text{S}_{14}$ ( $329\text{ cm}^{-1}$ )	Lucazeau 1977 Lucazeau 1978
residual peak	$398\text{ cm}^{-1}$	$\text{GaS}_4$ ( $404\text{ cm}^{-1}$ )	Lucazeau 1977
peak 4	$644\text{ cm}^{-1}$	fluorescence	

Figure 2.13: Deconvoluted peaks resulting from a Gaussian fit and residual peaks of the Raman spectrum of GLS bulk and the contributions to the spectral features. [127–129]

Literature research only shows references for wavenumbers lower than  $400\text{ cm}^{-1}$ . The Raman spectrum taken with an excitation wavelength of  $532\text{ nm}$  revealed a broad band at  $530$  to  $900\text{ cm}^{-1}$  which vanishes when the laser wavelength is changed to  $633\text{ nm}$ . This indicates the measured peak is mainly generated by fluorescence.



The fluorescence frequency of  $644\text{ cm}^{-1}$  is corresponding to a wavelength of  $15.52\text{ }\mu\text{m}$  or a transition energy of  $79.9\text{ meV}$ .

A depth-scan from  $-100\text{ }\mu\text{m}$  to the surface showed a dependence of overall intensities from the depth. The Raman intensity increases when the spectrum is collected closer to the surface. This surface effect is weaker for non-irradiated than for irradiated material, which means for increasing depths the difference in intensity of bulk and waveguide becomes larger. The ratio of Raman intensities of the waveguide over the bulk  $R_{\text{wg/bulk}}$  for the varying depth  $x$  in  $\mu\text{m}$  can be described with the exponential decay function  $R_{\text{wg/bulk}} \propto \exp\left(\frac{-x}{50.6}\right)$ . They can be observed in Fig. 2.14 (a). An explanation of this observation is that the exciting beam might get coupled into the waveguide, so the Raman signal could get 'trapped' or effects of spherical aberrations contribute to the measured behavior. Nevertheless, the chosen focal plane has no influence on the shape of the measured Raman spectrum. Normalized spectra obtained from different depths are still identical, see Fig. 2.14 (b).

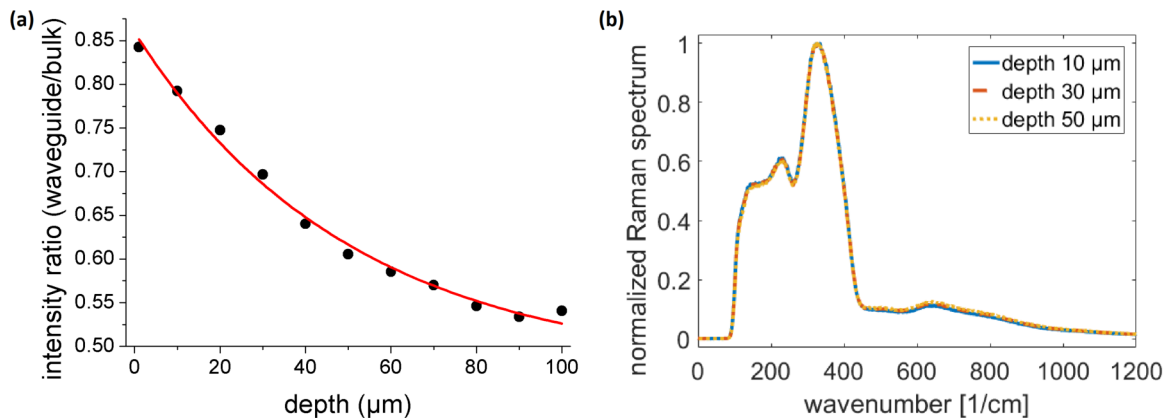


Figure 2.14: (a) Ratio of the heights of the main peak at  $333\text{ cm}^{-1}$  of the waveguide over the bulk for varying depths. (b) Waveguide Raman spectra taken in different measurement depths and normalized to the main peak at  $333\text{ cm}^{-1}$ .

More information about structural changes during laser irradiation is obtained by the comparison of relative changes of the single peaks in bulk and irradiated material. A direct comparison of normalized spectra from the irradiated area to the untreated material is shown in Fig. 2.15 (a). Both spectra were normalized to the maximum value of peak 3 (the highest peak). There is a clear difference distinguishable in relative peak heights especially for peak 1 and 2. The ratios of waveguide (wg) over bulk are displayed in Fig. 2.15 (b). Peak 1 and 2 are shifted to higher wavelengths by 1 and 2%. In contrast, the other fitted peaks experience a blue shift. The peak values of all peaks are higher for the waveguide region. The strongest difference of 20% is seen for peak 2. The waveguide peak widths show small differences from the bulk

widths.

The number of  $\text{GaS}_4$  tetrahedra and the  $\text{La}_6\text{Ga}_{10/3}\text{S}_{14}$  structure – both are contributing to peaks 1 to 3 – seem to be increased and slightly blue shifted due to laser radiation. A change of the coordination of lanthanum which leads to a reformation of the  $\text{GaS}_4$  tetrahedra and the  $\text{LaS}_8$  polyhedra is a possible reason for this result.

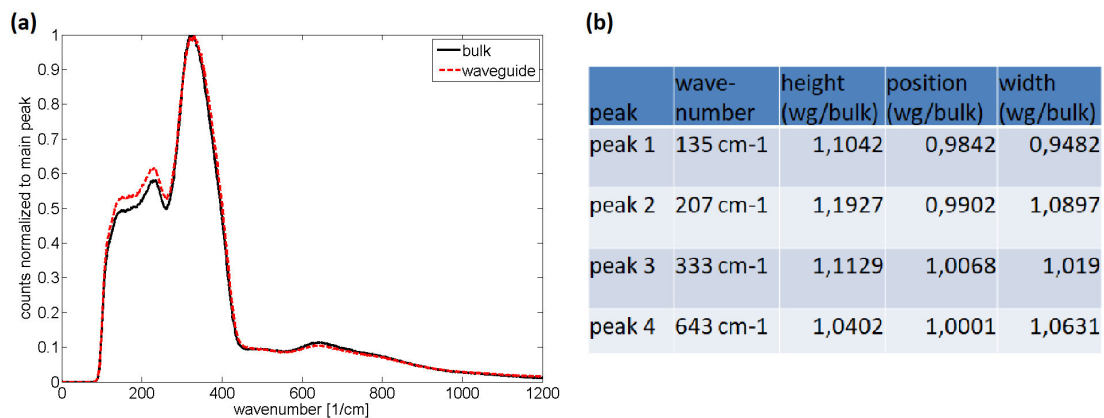


Figure 2.15: (a) Comparison between waveguide and bulk spectrum, normalized to the peak value. (b) Values for the ratio waveguide/bulk for peak height, peak position and peak width.

### Influence of laser parameters to the irradiated material

Interesting results are found by comparison of the Raman spectra of the polished cross sections of waveguides fabricated with different ULI parameters. Comparing the main peak value ( $333 \text{ cm}^{-1}$ ) normalized to the bulk spectrum over the cross sections (see Fig. 2.16) reveals a trend of lower peak height change for higher induced energies between bulk and waveguide. For higher translation speeds the waveguide peak intensity is observed to be higher than for lower translation speeds. For  $45 \text{ mW}$  laser power and  $1 \frac{\text{mm}}{\text{s}}$  translation speed and slower the peak heights for the irradiated material are actually lower than for the bulk GLS.

This indicates the change in the material modification process for these parameters compared to the waveguides written with lower laser energies, as already seen from the results for SEM (Section 2.3) and MFD (Section 2.4.1).

Also noticeable in all the Raman line scans are clear dips surrounding the waveguide peak. An increase in peak height corresponds to an increase of bond numbers with the same angle. This could indicate a densification or even a crystallization trend of the modified material. This means the local densification is caused by a material migration from the surrounding material to the focal volume which leads to



a reduction in density of the neighboring regions. This can be caused by a change of the lanthanum coordination number which creates La defects. Lanthanum is bound in  $\text{LaS}_6$ ,  $\text{LaS}_7$  and  $\text{LaS}_8$  tetrahedra with the average coordination number of 7.5 in the GLS bulk glass. If this number is decreased due to laser irradiation the density can locally increase and result in an enhanced refractive index.

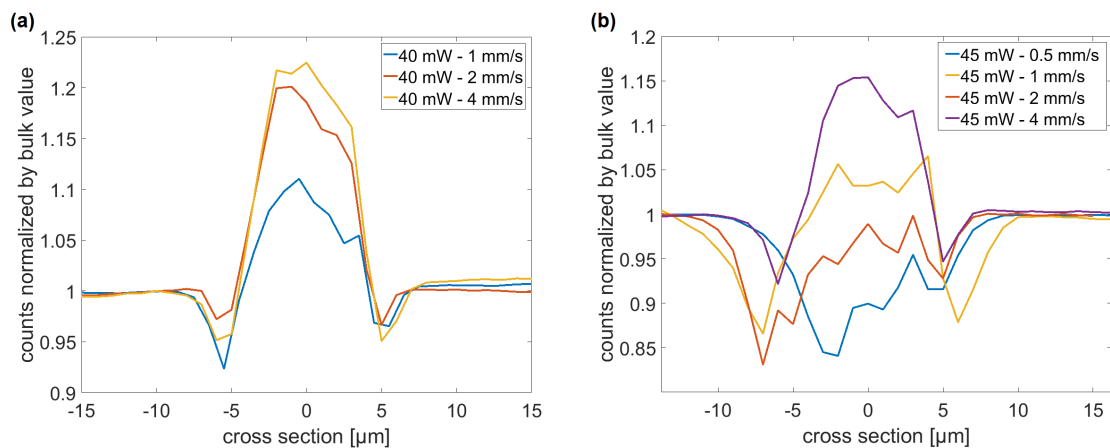


Figure 2.16: Comparison of the peak intensity at  $333\text{ cm}^{-1}$  change of Raman measurements on a line crossing waveguides for a laser power of 40 mW (a) and 45 mW (b) written with different writing speeds.

### 2.4.3 Polarimetric imaging

To write photonic integrated optics waveguides in glasses there is a need to put attention to the laser induced stresses. During laser inscription the optical and mechanical properties are locally altered. ULI can lead to e.g. material densification [86], expansion [87] or micro-cracks [85]. These volume changes result in a stress field surrounding the modification area.

The differing values for orthogonal polarization states of the input light (see Section 2.3) led to the conclusion that the waveguides are birefringent. To proof this, in addition to the polarizer manipulating the input polarization a polarization analyzer was added to the characterization setup and positioned after the sample. Setting the input polarization vertical ( $0^\circ$ ), diagonal ( $45^\circ$ ) and horizontal ( $90^\circ$ ) to the optical axis and observing the guided light intensities for different analyzer angles showed a total extinction for orthogonal polarizer-analyzer angles for  $0^\circ$  and  $90^\circ$ . However, diagonally polarized input light resulted in an output intensity different from zero for all possible analyzer angles, see Fig. 2.17 (b).

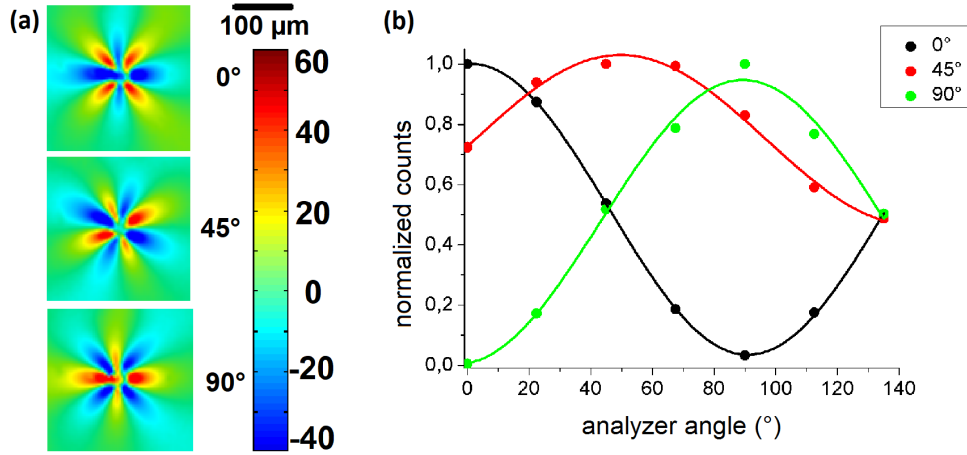


Figure 2.17: (a) Polarimetric image of the optical path difference of a single waveguide with rotating input polarization. (b) Transmitted intensity over analyzer angle for  $0^\circ$ ,  $45^\circ$  and  $90^\circ$  polarized input light.

Accordingly, transmitted diagonally polarized light is not linearly polarized. Therefore, vertical and horizontal modes exhibit different propagation coefficients. The output field can be calculated using the Jones matrix formalism [107]

$$\hat{E}_{\text{out}} = \hat{P} \hat{T} \begin{pmatrix} 1 \\ \frac{1}{2} \end{pmatrix} \quad (2.7)$$

with

$$\hat{P} = \begin{pmatrix} \cos^2 \theta & \sin \theta \cos \theta \\ \sin \theta \cos \theta & \sin^2 \theta \end{pmatrix} \quad (2.8)$$

and

$$\hat{T} = \begin{pmatrix} 1 & 0 \\ 0 & e^{i\varphi} \end{pmatrix} \quad (2.9)$$

using the phase difference between orthogonal directions  $\varphi$  and the direction angle of the fast axis  $\theta$  with respect to the x-axis. The measured data points from Fig. 2.17 are fitted with the following equation

$$|E_{\text{out}}|^2 = A(1 + \cos \theta \sin \theta \cos \varphi) \quad (2.10)$$

with  $A$  being the amplitude of the measurement and  $\theta$  the analyzer angle. For the phase delay  $\varphi = 0.82$  rad was obtained. This value leads to an estimation of the optical

path difference (OPD) and the effective refractive index change:  $OPD = \lambda \frac{\varphi}{2\pi} = 0.44 \mu\text{m}$  and  $\Delta n = \frac{OPD}{L} = 6.3 \cdot 10^{-5}$  with the sample length  $L = 7 \text{ mm}$ . A RSoft beam propagation simulation of the waveguide using the mode solver feature of the program resulted in  $\Delta n_{\text{eff}} = 3 \cdot 10^{-5}$ , which is in the same order of magnitude. With this knowledge, the difference of the propagation constants for the orthogonal linear polarization states can be calculated to  $\Delta\beta \sim 0.12 \text{ mm}^{-1}$ .

The origin of this behavior is the form birefringence of the waveguides due to the non-circular geometry of the waveguide cross section.

An imaging microscope with crossed polarizers, one on each side of the sample, showed a butterfly-shaped shadow of about  $100 \mu\text{m}$  size around the waveguide which is a hint that the waveguides also show a kind of stress induced birefringence (see Fig. 2.17).

An imaging polarimeter can visualize mechanical stresses by displaying the OPDs in the sample. They are a direct measure of the stress birefringence of the sample. Instead of measuring the phase difference interferometrically, the photoelastic effect is used for the birefringence diagnosis. In the case of a translation through a birefringent material the orthogonal TE and TM modes have different propagation velocities. This speed difference leads to a phase shift and an OPD between the modes and the traversing linearly polarized light becomes elliptically polarized.

The imaging polarimeter ilis StrainMatic M4/180 which was used for the measurements uses light with linear polarization with changeable orientation and a wavelength of  $\lambda = 589 \text{ nm}$ , which is converted into elliptical polarization by traversing the sample due to the photoelastic effect. A  $\frac{\lambda}{4}$ -plate converts the transmitted light back to linear polarized light whose angle  $\alpha$  can be determined with an analyzer and correlated to the stress birefringence with [130]

$$OPD = \frac{\alpha \cdot \lambda}{\pi} . \quad (2.11)$$

The OPD image of cross section of a  $d = 3 \text{ mm}$  long waveguide in GLS is shown in Fig. 2.17 (a). The maximal OPD of the stress pattern is  $60 \text{ nm}$ . From this value the refractive index change can be calculated by  $\Delta n = \frac{OPD}{d} \sim 2 \cdot 10^{-5}$ . Compared to the laser induced refractive index change of  $\sim 10^{-3}$  this value is only 2 orders of magnitude smaller. Therefore, an influence to the optical properties of neighboring waveguides is possible. The phase delay between two  $25 \text{ mm}$  long waveguides with this difference in the core refractive index is  $\sim \frac{1}{3}\pi \text{ rad}$ .

Polarimetric measurements with a fixed analyzer (see Fig. 2.17 (a)) revealed that the optical axes rotate when the linear polarization of the input light is changed. This

proves that the optical axes are aligned along the circumference of concentric circles. The strain measurements of parallel waveguide arrays with 3, 4, and 5 waveguides in one plane with a separation distance of  $20\ \mu\text{m}$  reveal a complex stress field with accumulated strains and also resulting refractive index changes in the overlapping regions with peaks located in between the written waveguides ca.  $16.7\ \mu\text{m}$  above the waveguides, see Fig. 2.18 (b).

Laser irradiation densifies the material and induces a nearly isotropic, long-range radial stress field to the glass which affects the optical properties of any waveguide written successively within the range of the stress field (20 to  $25\ \mu\text{m}$ ).

The experiments have shown that these stresses accumulate when waveguides are located close to each other. The example in Fig. 2.18 shows the 3 mm-long 5-waveguide array which exhibits an OPD increase of the area to the left compared to the right of the array that is about 13 nm. For 4 and 3 waveguides the polarimetric measurement revealed an OPD increase of 9 nm and 7 nm, respectively.

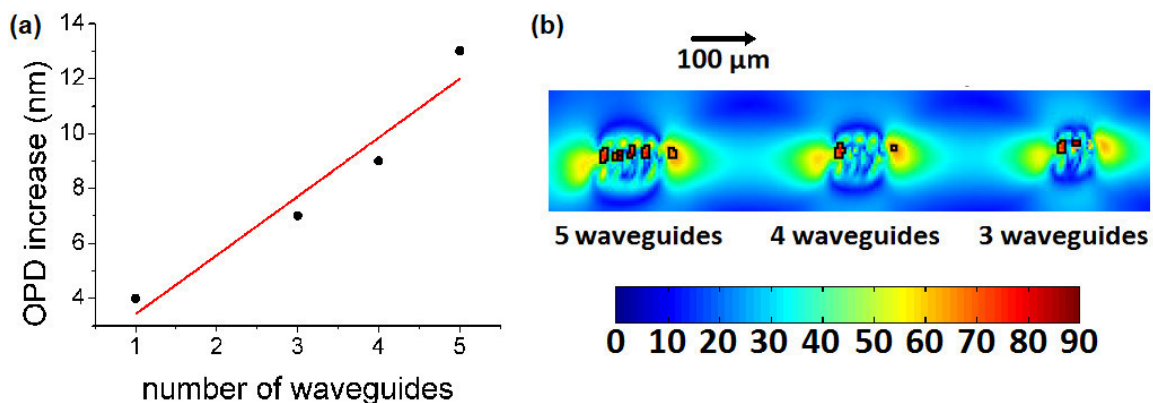


Figure 2.18: (a) Increase of optical path difference for writing arrays of waveguides with varying waveguide numbers. (b) Stress field of an array of 5, 4 and 3 waveguides separated by  $20\ \mu\text{m}$  (sample length: 3 mm). The arrow indicates the direction of writing.

## 2.5 Reduction of laser induced stresses by annealing

Annealing is used to relieve materials from stresses. The material is heated to allow a reorientation of the material particles to an energetically better condition. [96] The heat treatment can take place before (pre-annealing) or after (post-annealing) the waveguide writing.

Pre-annealing should relax the stresses due to the substrate fabrication process, the cutting and the polishing of the glass substrates. It has a clear visible effect on the

later MFD of the waveguide at a wavelength of  $3.39 \mu\text{m}$ , see Fig. 2.19.

One GLS substrate was cut into 5 pieces of the same size ( $20 \times 10 \times 1 \text{ mm}^3$ ). One part was put aside for reference and the other pieces were heated in an argon atmosphere with a rate of  $1 \frac{\text{K}}{\text{min}}$  until the final temperature of  $500^\circ \text{C}$ . Afterwards, the samples stayed at this temperature for 24 h, 36 h, 48 h or 60 h and the temperature was decreased at  $1 \frac{\text{K}}{\text{min}}$  back to room temperature. After the annealing process waveguides with identical parameter sets were written into the samples and the MFDs were compared.

The size of the mode field of waveguides written with 40 mW laser power increases for longer annealing times. For  $0.5 \frac{\text{mm}}{\text{s}}$  and  $1 \frac{\text{mm}}{\text{s}}$  translation speed there is a local MFD minimum visible for 24 h. Higher writing speeds lead to a stronger MFD slope with increasing annealing time. The slope for the linear fit of the MFD of  $0.5 \frac{\text{mm}}{\text{s}}$  is  $0.017 \frac{\mu\text{m}}{\text{h}}$ , for  $1 \frac{\text{mm}}{\text{s}}$  it is  $0.049 \frac{\mu\text{m}}{\text{h}}$  and increasing for 2, 4 and  $8 \frac{\text{mm}}{\text{s}}$  to 0.050, 0.069 and  $0.214 \frac{\mu\text{m}}{\text{h}}$ .

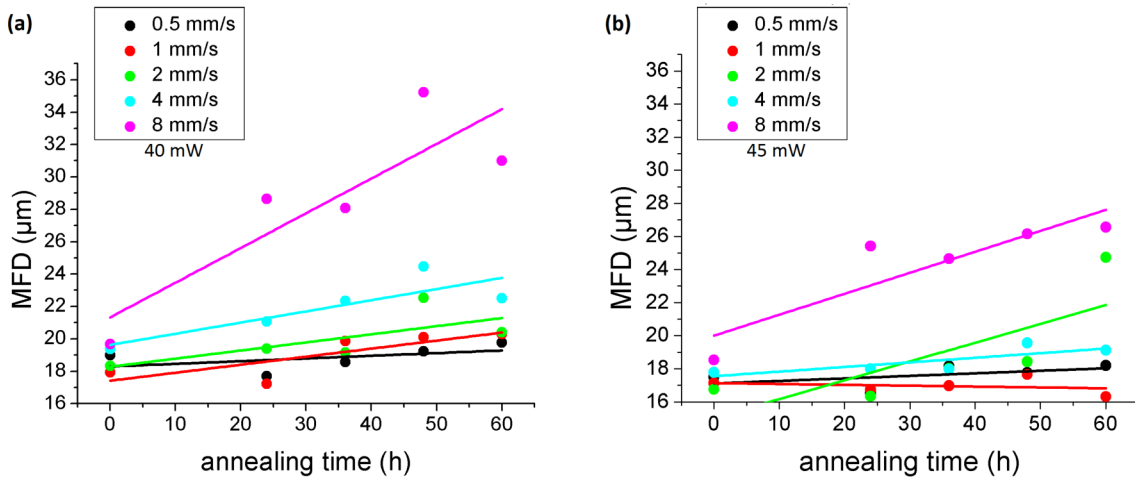


Figure 2.19: (a) MFD at  $3.39 \mu\text{m}$  wavelength of waveguides written with (a) 40 mW and (b) 45 mW laser power and different writing speeds in samples annealed with different annealing times.

For 45 mW the slopes are not as steep. For  $0.5 \frac{\text{mm}}{\text{s}}$  it is  $0.014 \frac{\mu\text{m}}{\text{h}}$  which is about the same, for  $1 \frac{\text{mm}}{\text{s}}$  the values are almost constant ( $0.005 \frac{\mu\text{m}}{\text{h}}$ ) and for 2, 4 and  $8 \frac{\text{mm}}{\text{s}}$  the rates are 0.113, 0.028 and  $0.127 \frac{\mu\text{m}}{\text{h}}$ .

The annealing has a stronger influence to the MFD of waveguides that experienced less deposited energy due to ULI. The waveguides written with high laser powers or low writing speeds are more stable during heat treatment.

The refractive index contrast could be derived as described in Section 2.3 and shown in Fig. 2.20. A negative trend in refractive index change over annealing time is

distinguishable for higher writing speeds and a lower laser power, while the refractive index difference is nearly constant for higher laser powers and low scanning velocities. This means that waveguides fabricated with less deposited energies tend to adapt the refractive index to the bulk refractive index in a stronger way than others. A different resulting structure or a phase transition between the parameter sets could be the origin of this behavior.

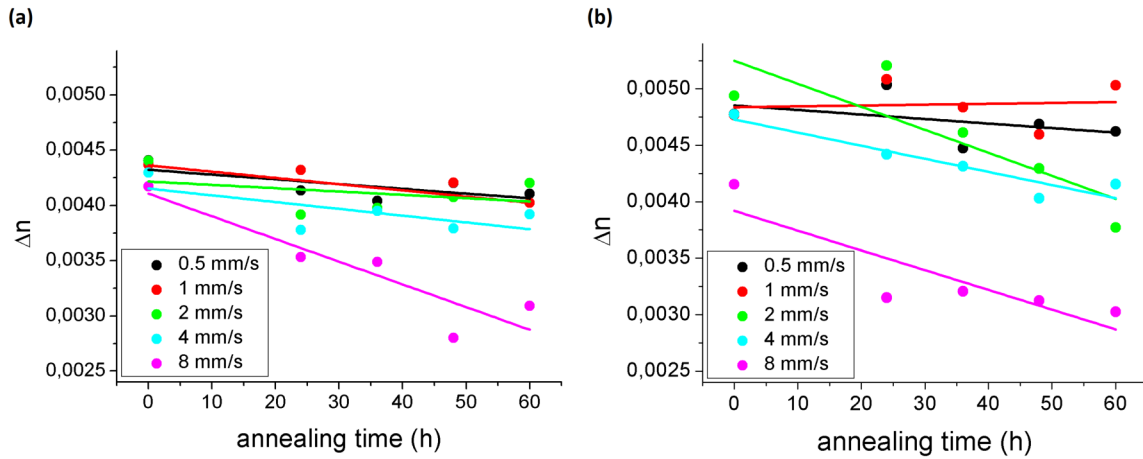


Figure 2.20: (a) Refractive index change  $\Delta n$  of waveguides written with (a) 40 mW and (b) 45 mW laser power and different writing speeds in samples annealed with different annealing times.

A pre-annealing of 24 h at 500° C showed the smallest mode field diameter and the highest refractive index change for waveguides fabricated with 40 mW laser power and 1  $\frac{\text{mm}}{\text{s}}$  writing speed. Longer annealing times produce larger mode fields and therefore less  $\Delta n$ . Accordingly, longer annealing times are not necessary.

Polarimetry measurements for annealed samples can reveal the effect of the annealing process on the stress field in GLS. When delivered, the 1 mm thick samples showed maximum OPD values of about 10 nm at the edges which corresponds to a  $\Delta n$  of  $\sim 10^{-5}$  and is probably due to the cutting of the samples. This stress can be reduced to half by annealing the substrate 24 h at 500° C. Waveguides written in annealed material exhibit a smaller stress area and also less contrast in OPD and therefore refractive index change, see Fig. 2.21 (a). Longer annealing does not lead to a further decrease of the stress.

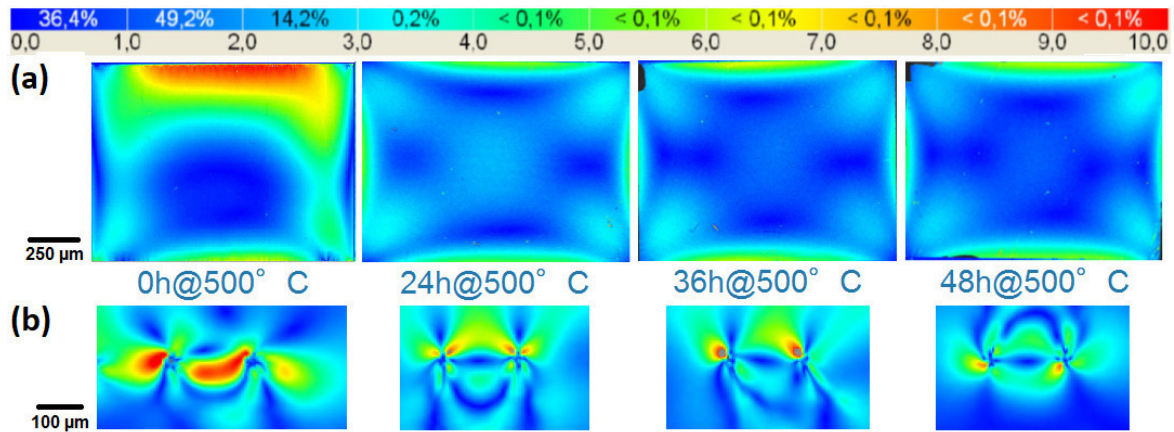


Figure 2.21: (a) Comparison of polarimetric images of plain unmodified samples for different annealing times. (b) Images of two waveguides separated by 170  $\mu\text{m}$ .

Raman measurements of pre-annealed waveguides written with a laser power of 40 mW and a writing speed of  $1 \frac{\text{mm}}{\text{s}}$  showed the results in Fig. 2.22. A drastic change in the main peak contrast at  $333 \text{ cm}^{-1}$  for bulk and waveguide is distinguishable for the first 24 h of annealing. For longer annealing times the shape of the graphs does not vary as strongly. This correlates with the OPD and MFD measurement results. The MFDs are reduced for a 24 h annealing and increase for longer annealing times while the peak intensity change between bulk and waveguide is weakest for an annealing time of 24 h.

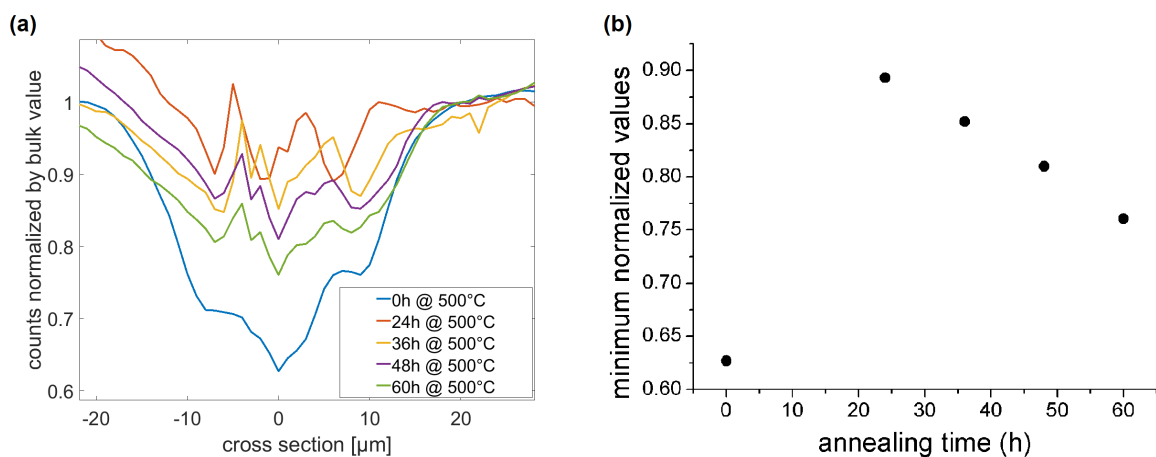


Figure 2.22: (a) Comparison of the peak intensity change at  $333 \text{ cm}^{-1}$  of Raman measurements at the line scan crossing waveguides written with different annealing times for a waveguide written with a laser power of 40 mW and a translation speed of  $1 \frac{\text{mm}}{\text{s}}$ . (b) Minimum value of (a) over annealing time.



The measured OPD for the waveguide surrounding material also decreases for an annealing of 24 h but not for longer annealing times. Sample annealing for longer than 24 h is obviously not necessary. The Raman measurements show the smallest difference between waveguide and bulk structure for this tempering treatment.

The density of the samples annealed at 500° C for different annealing times were estimated by measuring the dimensions with a micrometer stage and the mass with precision scales and shown in Fig. 2.23 (a). A minimum in between 24 h and 36 h can be observed. The MFD measurements also showed a minimum for an annealing time of 24 h. If the density of the bulk glass is low, the MFD can be small, because the ULI can induce a higher density change and therefore a higher refractive index change.

The relaxation of the material due to annealing also causes a reduction in refractive index change. According to literature [96] annealing lowers the enthalpy of the material, which results in a thermodynamically more stable glass that has a higher density and a higher refractive index. The tempered structures lose their flexibility to react to laser irradiation and enhance the refractive index for longer annealing times.

In cooperation with the glass manufacturer ChG Southampton Ltd. the annealing temperatures of the glass samples during the fabrication process could be changed. The temperature after quenching was set to 490° C, 500° C, 550° C and 600° C for one sample each. The densities of these samples are shown in Fig. 2.23 (b). The observed trend of the mean density is positive for increasing annealing temperatures with a saturation at about 550° C.

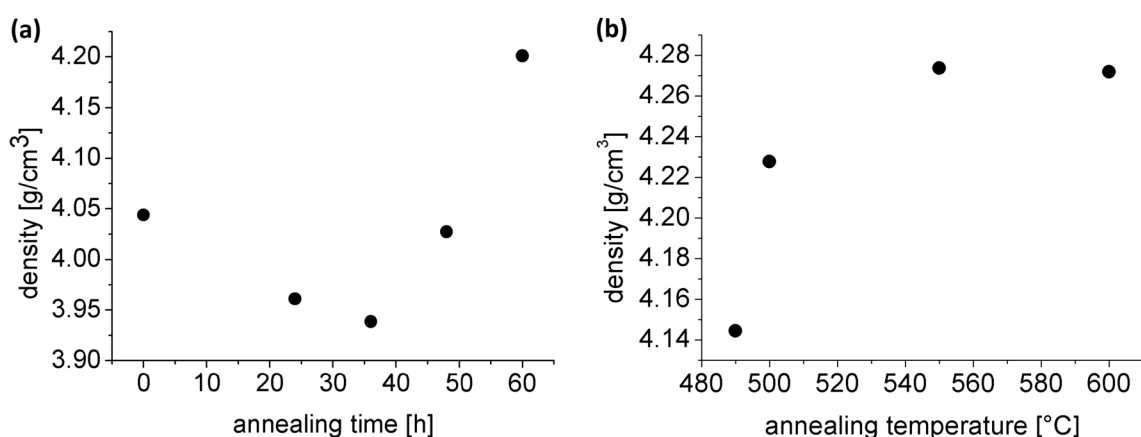


Figure 2.23: (a) Density for samples annealed at different annealing times for an annealing temperature of 500° C. (b) Density for samples annealed at different annealing temperatures.



While the three samples annealed with a temperature lower than  $600^\circ\text{C}$  exhibit a transparent 'glassy' appearance the sample annealed at  $600^\circ\text{C}$  is unclear or 'milky'. This change in appearance is due to the fact that the annealing temperature exceeded the crystallization temperature which leaved the sample with a crystalline structure. A small difference in total measured density can be observed between Fig. 2.23 (a) and Fig. 2.23 (b) because the assumption that all corner angles being rectangular and no scratches or other surface irregularities being present might not be correct. Nevertheless, in average the relations between the measured values should be still correct.

Raman microscopy on the sample annealed to  $600^\circ\text{C}$  revealed more sharp features compared to the other samples (see Fig. 2.24 (b)). There are three peaks contributing to first characteristic feature at  $161\text{ cm}^{-1}$ ,  $198\text{ cm}^{-1}$  and  $232\text{ cm}^{-1}$  which correspond to  $\text{La}_6\text{Ga}_{10/3}\text{S}_{14}$  ( $200\text{ cm}^{-1}$ ),  $\text{La}_{10/3}\text{Ga}_6\text{S}_{14}$  ( $196\text{ cm}^{-1}$ ,  $233\text{ cm}^{-1}$ ),  $\text{GaS}_4$  tetrahedra ( $232\text{ cm}^{-1}$ ) and  $\text{La}_2\text{S}_8$  ( $225\text{ cm}^{-1}$ ). The most prominent peak at  $320\text{ cm}^{-1}$  is formed by resonances in the  $\text{GaS}_4$  and  $\text{La}_6\text{Ga}_{10/3}\text{S}_{14}$  structures. Another side peak at  $360\text{ cm}^{-1}$  is originated by the  $\text{GaS}_4$  tetrahedra while the remaining features turned out to be part of the fluorescence spectrum. A variation of the laser wavelength revealed the position and the extent of the fluorescence (see Fig. 2.24 (b)) as it is also the case for the Raman spectrum of the glassy substrate.

A change in input polarization had no significant effect on the spectrum, see Fig. 2.24 (a).

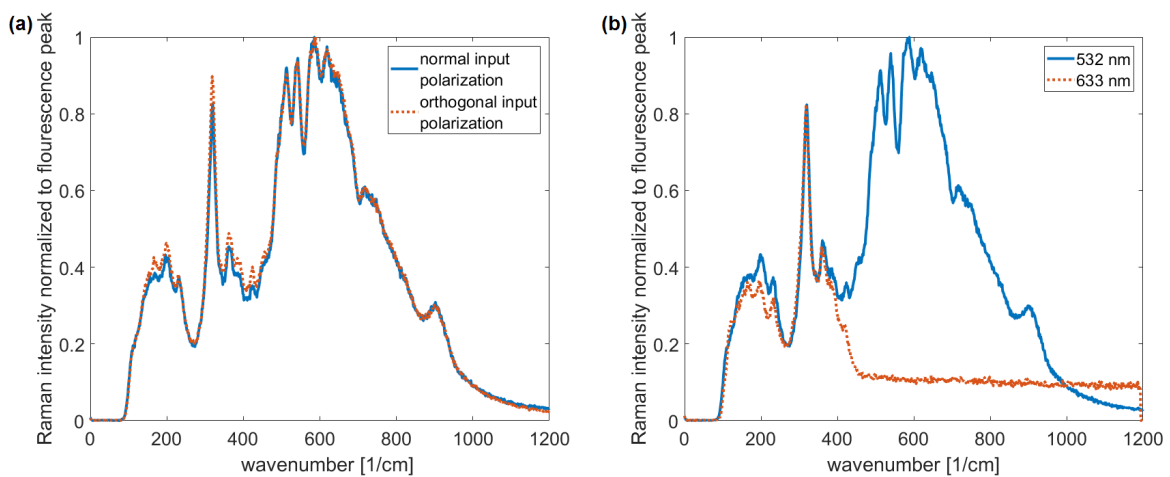


Figure 2.24: (a) Raman spectra of the crystalline sample for normal and orthogonal input polarization. (b) Raman spectra of the same sample with the excitation wavelength of 532 nm and 633 nm.

Post-annealing can reduce stresses after laser writing. GLS samples, as they were delivered, have experienced ULI for the fabrication of multimode waveguides (50 mW laser power and  $1 \frac{\text{mm}}{\text{s}}$  writing speed) followed by an annealing treatment at 24 h at  $400^\circ \text{C}$  with heating and cooling rates of  $1 \frac{\text{K}}{\text{min}}$ .

The post-annealing process could reduce the stress field surrounding the waveguides to about 60% but even multimode waveguides exhibit no transmitted field after annealing, though the used temperature is far away from the glass transition temperature ( $580^\circ \text{C}$ ). Further investigation on post-annealing is necessary.

## 2.6 Conclusions

In conclusion GLS is a suitable material for ULI of single mode waveguides operating at  $3.39 \mu\text{m}$ . Several independent experiments showed a parameter dependent laser induced modification of the glass structure. The stresses can influence the wave transmission characteristics of a waveguide. The use of waveguide arrays with many closely spaced waveguides can therefore exhibit a strong stress dependent transmission behavior.

The measurements of the mode field diameter, the surface structure with scanning electron microscopy, the optical path difference and the Raman spectra over the waveguide cross section of waveguides written with different laser powers and sample translation speeds exhibit a consistent result. There is a structural difference for waveguides written with high laser deposited energy, meaning high laser powers and low writing speeds, compared to waveguides that experienced less laser power irradiation and a shorter irradiation time.

According to the MFD measurement in Section 2.3 the point on which the structural change occurs is the minimal point of MFD over the translation speed of about  $1 \frac{\text{mm}}{\text{s}}$  for 40 mW and  $2 \frac{\text{mm}}{\text{s}}$  for 45 mW. The higher deposited energies at high laser power or slow writing speeds induce a higher local temperature to the irradiated region. This can lead to a local melting or crystallization of the material. For the SEM images in Section 2.4.1 the structure of the waveguide cross sections surface was shown to change below  $1 \frac{\text{mm}}{\text{s}}$  for 40 mW and below  $2 \frac{\text{mm}}{\text{s}}$  for 45 mW. The etching rate also changed its slope drastically at  $4 \frac{\text{mm}}{\text{s}}$  for 40 mW laser power and at  $2 \frac{\text{mm}}{\text{s}}$  for 45 mW. The comparison of the highest peaks of the Raman spectra of the waveguide cross sections in Section 2.4.2 showed an uniform increase in intensity for translation speeds higher than  $1 \frac{\text{mm}}{\text{s}}$  and a lower Raman intensity originating from the waveguide compared to the bulk for writing speeds of  $2 \frac{\text{mm}}{\text{s}}$  and below.

In all measurements the points of the change in the observed features coincide. The possibility that the change in material properties is random is very small, which supports the assumption that for higher deposited energies a higher temperature in the glass is reached which leads to a possible partial crystallization of the illuminated material while for smaller energies the laser modification is mainly due to material densification caused by La recoordination and atom relocation due to tensile stresses, maybe even in melted glass phase.

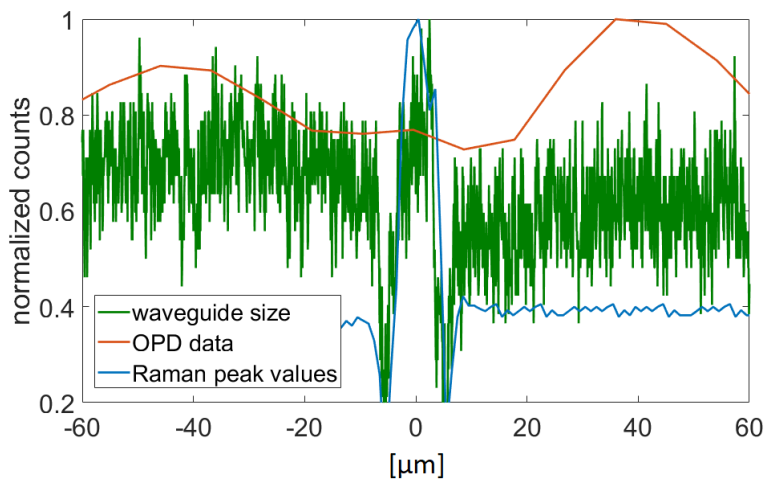


Figure 2.25: Comparison of the polarimetric cross section, the Raman peak intensities and the waveguide size over distance for the same waveguide (40 mW laser power and  $1 \frac{\text{mm}}{\text{s}}$  writing speed).

Direct comparison of the polarimetric waveguide cross section, the Raman main-peak heights across a waveguide and the horizontal microscopic image profile of one waveguide written with 40 mW laser power and  $1 \frac{\text{mm}}{\text{s}}$  match quite well. The locations of the waveguide boundaries are identical. At the edges of the waveguide a region with lower refractive index occurs. The densification of the waveguides involves a migration of atoms from the surrounding volume which leads to a decreased density in the poly-crystalline waveguide region.

Another contribution to the refractive index change of the irradiated material can be color center formation. A color center is a defect with an anionic vacancy in a transparent material which is filled with electrons or holes. It can be introduced by exposure of ionizing radiation. These defects cause a color change of the material when the electronic ground state is excited by absorption of certain wavelengths. [131] ULI can also introduce color centers to the glass which can contribute to the local refractive index of the material. [132] A hint for color center formation can be the observation of a red shift of the waveguides in microscope images (Fig. 2.6).

The fluorescence spectra obtained by the Raman measurement show an electron transition at an energy of 80 meV.

A decrease of propagation losses and the reduction of manufacturing time could be achieved by optimizing the number of laser scans and scan separation distance or the change of writing wavelength. A broad parameter scan would be necessary. Also the reproducibility of the waveguide's properties is an important goal which is also connected to the control of spatial homogeneity of the sample structure before the ULI process. To achieve a more homogeneous glass structure the annealing during the fabrication process of the GLS samples has to be optimized. Additionally, a temperature treatment after ULI with shorter annealing times could decrease the stress birefringence of the waveguides while keeping the ability of wave guiding.

# Chapter 3

## Integrated optics beam combination for astronomical interferometry

In this chapter evanescent coupling of waveguides and the benefit of integrated optics waveguide arrays for astronomical interferometry are described. S-bends and directional couplers are designed, fabricated and the propagation constant and coupling coefficient are obtained from the characterization results to enable the design of integrated optics beam combiners based on evanescent waveguide coupling. Interferometric beam combiners consisting of an array of straight waveguides arranged in a zig-zag configuration and a pairwise ABCD beam combiner are presented and interferometrically characterized to evaluate the applicability to stellar interferometry using a multiple telescope configuration. Finally the asymmetric behavior of the zig-zag discrete beam combiner (DBC) is traced back to laser induced stresses, followed by the presentation of solutions to this problem by stress compensation in order to improve the presented components even further.

### 3.1 Evanescent coupling in integrated optics waveguides

Evanescent coupling is a useful phenomenon for interferometric applications of integrated optics beam combiners. It can be understood by the following picture. When electromagnetic fields enter a region in which they cannot propagate the field fades exponentially. The wave vector becomes complex-valued outside of the allowed waveguide region. For two closely placed waveguides the electrical field of one waveguide can perturb the propagation equation of the other waveguide. Therefore, the amplitude of the field generally becomes a function of the propagation

distance  $z$ . [133]

Integrated optics directional beam combiners can be described using the coupled mode theory. The coupled mode theory was first formulated in the 1950's [134] and soon connected to waveguides [135–139]. It is a mathematically simple and physically intuitive theory that describes the power coupling of weakly coupled nearly identical waveguides by the linear superposition of the modes of individual waveguides. Evanescent coupling allows a power flow from one waveguide to another though the waveguide cores do not overlap. It is enabled by photon tunneling through the cladding.

This means for at least two dielectric waveguides, which are placed close enough to each other in a parallel configuration so that the electromagnetic fields can reach the other waveguide, but far enough to obtain only weak waveguide coupling, the evolution of the amplitudes of the modes  $A_1$  and  $A_2$  can be described by coupled mode equations. Their solution describes the wave propagation of electromagnetic fields in the waveguides and evanescent coupling between them.

For isolated waveguides

$$\frac{dA_1}{dz} = -i\beta_1 \cdot A_1 \quad (3.1)$$

and

$$\frac{dA_2}{dz} = -i\beta_2 \cdot A_2 \quad (3.2)$$

describe the wave propagation with  $\beta_1$  and  $\beta_2$  being the propagation constants of the waveguides. When the waveguides are brought close together coupling plays a role:

$$\frac{dA_1}{dz} = -i\beta_1 \cdot A_1 - ik_{12} \cdot A_2 \quad (3.3)$$

and

$$\frac{dA_2}{dz} = -i\beta_2 \cdot A_2 - ik_{21} \cdot A_1 \quad (3.4)$$

with  $k_{12}$  and  $k_{21}$  being the coupling coefficients between the modes in the referring waveguides. The coupling coefficients result from the overlap integrals of the respective waveguide fields. The guided power is described by  $P(z) = P_1 + P_2 = |A_1|^2 + |A_2|^2$ . The law of power conservation requires that  $k_{12} = k_{21} = \kappa$  are real-valued. After separating the average phase factor we receive

$$A_i(z) = \hat{A}_i \cdot \exp\left(-i \frac{\beta_1 + \beta_2}{2} z\right) \quad (3.5)$$

for either waveguide, which leads to

$$\frac{d\hat{A}_1}{dz} = -\frac{i}{2} \cdot \Delta\beta \cdot \hat{A}_1 - i\kappa\hat{A}_2 \quad (3.6)$$

and

$$\frac{d\hat{A}_2}{dz} = +\frac{i}{2} \cdot \Delta\beta \cdot \hat{A}_2 - i\kappa\hat{A}_1 \quad (3.7)$$

with the detuning mismatch factor  $\Delta\beta = \beta_2 - \beta_1$ . When waveguide 1 is excited at the input power  $P_0$  the power values evolve as

$$P_1(z) = P_0 \left( \cos^2(\gamma z) + \left( \frac{\Delta\beta}{2\gamma} \right)^2 \cdot \sin^2(\gamma z) \right) \quad (3.8)$$

and

$$P_2(z) = P_0 \left( \frac{|\kappa|^2}{\gamma^2} \sin^2(\gamma z) \right) \quad (3.9)$$

with

$$\gamma = \sqrt{\kappa^2 + \left( \frac{\Delta\beta}{2} \right)^2} . \quad (3.10)$$

Eqn. 3.8 and 3.9 can be simplified to

$$P_1(z) = P_0 \cos^2(\gamma z) \quad (3.11)$$

and

$$P_2(z) = P_0 \sin^2(\gamma z) \quad (3.12)$$

for the case when  $\Delta\beta = 0$  and the waveguides are phase matched. [107] The complete power transfer from one waveguide to the other happens at one coupling length [140]

$$z = L_C = \pi / (2\gamma) . \quad (3.13)$$

A 50/50 beam splitter can be realized by a directional coupler (compare Section 3.2) with the directional coupler interaction length of  $l = \frac{L_C}{2}$ .

If a phase mismatch ( $\Delta\beta \neq 0$ ) is introduced to the system, for example by applying an electric voltage to an electro-optical material, the power transfer ratio can be controlled, which can be used for the manufacturing of electrically active directional couplers. [107]

### 3.2 Deriving coupling coefficients and propagation constants with directional couplers

To be able to design a beam combiner with the required performance the coupling coefficient needs to be known.

The optical component used to investigate the coupling of waveguides in gallium lanthanum sulfide glass was a directional coupler, which consists of two waveguides that are brought close together by raised-sine double s-bends, see Fig. 3.1 (a). The curvature of waveguides introduces losses due to the scattering of light out of the waveguide. In order to estimate the bending losses when working with a short bending length, a scan of the dislocation height of s-bends  $h$  was necessary. The following equation for the single s-bend geometry was used:

$$y = \frac{hx}{l} - \frac{h}{2\pi} \cdot \sin\left(\frac{2\pi x}{l}\right) \quad (3.14)$$

with  $h$  the lateral distance from begin to end of the bend and  $l$  the length of the bent part.

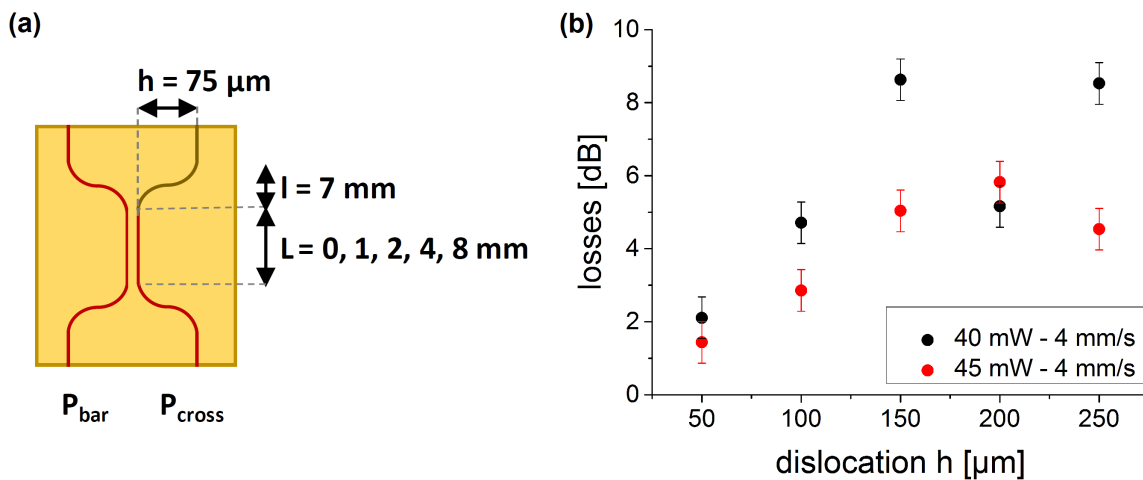


Figure 3.1: (a) Schematic image of the design of the directional coupler. (b) Losses of double-s-bends with different writing laser powers and dislocations and a length of  $l = 7 \text{ mm}$  and a writing speed of  $4 \frac{\text{mm}}{\text{s}}$  for a characterization wavelength of  $3.39 \mu\text{m}$ .

Combining two of these bends with a straight part in between creates the double s-bends shown in Fig. 3.1 (a). The bending losses can be determined by comparing the transmission of waveguides with a variation in  $h$  to straight waveguides while keeping the length  $l$  of the bend constant. The result can be observed in Fig. 3.1 (b). Double s-bends with the dislocation  $h = 75 \mu\text{m}$  and the length  $l = 7 \text{ mm}$  are assumed



to exhibit a reasonable bending loss of about 2 dB at a wavelength of  $3.39 \mu\text{m}$  when using the benefit from the small size, which is an important property when designing photonic chips based on cascaded couplers.

The directional coupler consists of two waveguides built of one s-bend that brings the waveguides towards each other a straight part, at a small distance between the waveguides and a second s-bend, which leads the waveguides back to their original x-position (see Fig. 3.1 (a)).

In order to receive a value for the coupling coefficient an experimental series of directional couplers with a variation of the horizontal (20 to  $30 \mu\text{m}$ ) and diagonal (18 to  $24 \mu\text{m}$ ) gap and a variation of the length (0, 1, 2, 4, 8 mm) of the straight central section was performed. For every coupler the splitting ratio  $R = \frac{P_{\text{cross}}}{P_{\text{bar}} + P_{\text{cross}}}$  was calculated using the waveguide output powers of the injected ( $P_{\text{bar}}$ ) and the coupled ( $P_{\text{cross}}$ ) waveguide (see Fig. 3.1 (a) for details) and the values for the coupling coefficient  $\kappa$ ,  $\gamma$  and the propagation constant  $\Delta\beta$  were calculated as fit parameters of Eqn. 3.9 (see Fig. 3.3 (a)):

$$\frac{P_{\text{cross}}}{P_{\text{bar}} + P_{\text{cross}}} = \left(\frac{\kappa}{\gamma}\right)^2 \cdot \sin^2(\gamma L + \varphi) \quad (3.15)$$

and Eqn. 3.10 with  $\varphi$  being the phase difference between both fields. [110, 141, 142] For horizontal couplers the splitting ratio is increasing until a gap of 21 to  $22 \mu\text{m}$  followed by a decrease until  $30 \mu\text{m}$  for all measured coupler lengths. The coupling constant is decreasing for broader gaps from  $(0.89 \pm 0.04) \frac{1}{\text{mm}}$  at  $21 \mu\text{m}$  to  $(0.80 \pm 0.02) \frac{1}{\text{mm}}$  at  $30 \mu\text{m}$ , see Fig. 3.2 (b).

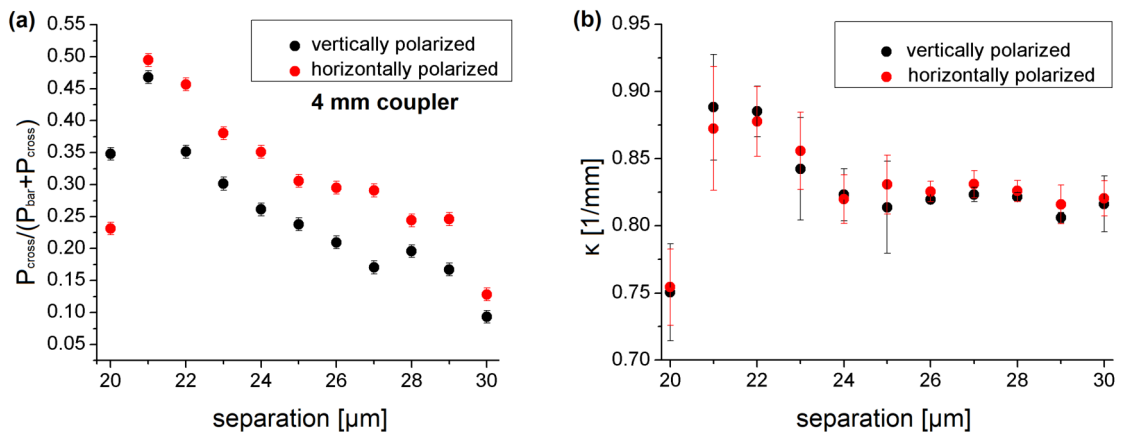


Figure 3.2: (a) Splitting ratio over gap width for horizontal 4 mm couplers written with 45 mW and  $1 \frac{\text{mm}}{\text{s}}$  writing speed. (b) Coupling coefficient  $\kappa$  for horizontal directional couplers with varying gap.

A measure of the changes in amplitude and phase of an electromagnetic wave propagating through a waveguide is the propagation constant  $\beta$ . The propagation constant difference between two waveguides in the directional coupler  $\Delta\beta = \beta_2 - \beta_1$  is shown in Fig. 3.3 (b). The value of  $\Delta\beta$  increases until it reaches its highest value of  $(0.45 \pm 0.06) \frac{1}{\text{mm}}$  for vertically and  $(0.21 \pm 0.02) \frac{1}{\text{mm}}$  for horizontally polarized light at a  $24 \mu\text{m}$  gap before it decreases again.

The polarization dependence is most probably caused by a laser-induced stress field surrounding the waveguides which leads to a different yield of successive waveguides with respect to the previous ones. The variation of effective refractive index in the stressed region is  $2.5 \cdot 10^{-4}$ . This was discussed in Section 2.4.3.

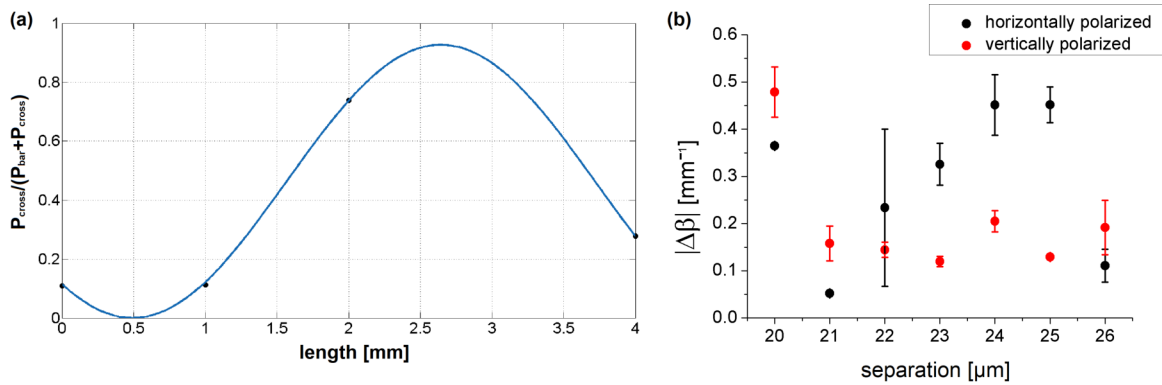


Figure 3.3: (a) Fitted splitting ratio for a coupler separation of  $21 \mu\text{m}$ . (b) Propagation constant over gap width for horizontal directional couplers.

Further characterization of a  $25 \text{ mm}$  long  $2 \times 2$  directional coupler with a horizontal dislocation of the waveguide due to the bend of  $75 \mu\text{m}$  and interaction length of  $4 \text{ mm}$  in the L ( $3$  to  $4 \mu\text{m}$ ) and M ( $4.6$  to  $5 \mu\text{m}$ ) band were performed at the university of Cologne by Jan Tepper [143].

The chromaticity of the splitting ratio could be measured by injecting two beams of a Michelson interferometer into one waveguide while one interferometer arm is delayed to receive an OPD of the second beam. Fourier transform spectroscopy enabled the derivation of the output spectrum. The splitting ratio over wavelength ranged from 30% to 70% in L-band.

Exciting both coupler arms at a time with monochromatic light at  $3.39 \mu\text{m}$  the change of polarization was found to be almost identical for both injected waveguides which is essential for its potential use in stellar interferometry. The elliptically polarized output light for angles other than  $0^\circ$ ,  $90^\circ$  and  $180^\circ$  (compare Section 2.4.3) was verified with this measurement.

The fringe contrast injecting  $3.39 \mu\text{m}$  monochromatic light was determined to be

97.8% and 98.1% for the coupler arms. In a L-band measurement (interferogram shown in Fig. 3.4) the contrast was found to be 94.9%. The  $\pi$ -phase shift was demonstrated over one coherence length. M-band measurements using the same component resulted in a fringe contrast of 92.1%. The differential dispersion, which is the difference in dispersion parameters of the two channels, is twice as large at this wavelength band. No temperature dependence of the coupler performance could be observed. [143]

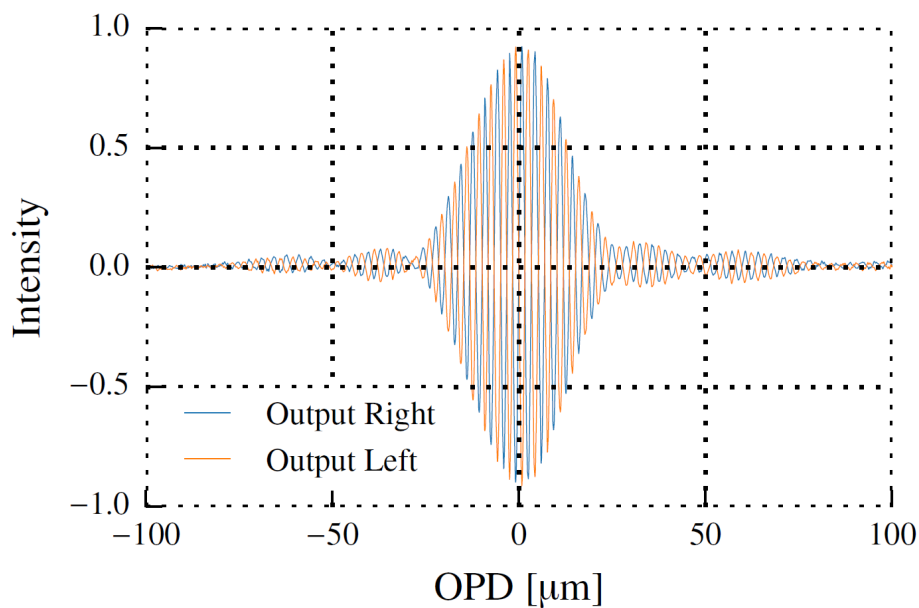


Figure 3.4: L-band interferogram of the directional coupler output. [143]

### 3.3 Integrated optics for stellar interferometry

Utilizing a discrete beam combiner (DBC) simplifies beam combination with multiple cascades of directional couplers to a two-dimensional regular array of coupled waveguides using discrete diffraction. The parallel waveguides can be arranged in a square array [57], but also other geometries are possible (see Section 3.4). A DBC that can be used for interferometric beam combination not only needs the possibility of nearest-neighbor (NN) coupling. Also the next-nearest-neighbor (NNN) interaction plays an important role. Complex visibilities cannot be retrieved by NN-coupling alone. Because long range coupling breaks the symmetry in the phase pattern, a simultaneous retrieval of all correlation functions is possible. [61]

Interferometric beam combiners transfer information of phase variations to ampli-

tude variations. [60] The output pattern of the waveguide array is obtained by interference of the input intensities that spread across the array. [59] For  $N$  input beams, the needed minimum amount of waveguides in the DBC  $M$  is determined by  $N^2$ . [60]

The interferometric intensities can be derived by a linear superposition

$$I = \left\langle \left| \sum_{i=1}^N \vec{E}_i \right|^2 \right\rangle = \sum_{i=1}^N \langle E_i \rangle \cdot \sum_{j=1}^N \langle E_j^* \rangle = \sum_{i=1}^N \Gamma_{i,i} + 2 \sum_{i=1}^{N-1} \sum_{j=i}^N C_{i,j} \cdot \Re \Gamma_{i,j} \quad (3.16)$$

using the electromagnetic input fields  $\vec{E}_i = \hat{e}_i E_i$ . The polarization mismatch is expressed by  $C_{i,j} = \hat{e}_i \cdot \hat{e}_j$  and  $\Gamma_{i,j} = \Gamma_{j,i}^* \equiv \langle E_i E_j^* \rangle$  takes the complex visibilities (mutual coherence functions) into account. In signal processing the spatial coherence is used to examine the power transfer between input and output of a system.

When using an interferometric beam combiner the relative phase between the input fields is usually modulated in space or time to retrieve the individual coherence functions. A multi-field beam combiner can be described by the visibility-to-pixel matrix (V2PM). [144] It is the link between the measured output intensities of the waveguides in an interferometric beam combiner and the visibility function. The intensity at  $n^{\text{th}}$  output is given by

$$\begin{aligned} I_n &= \sum_{i=1}^N \langle |U_{n,i} E_i|^2 \rangle + 2 \sum_{i=1}^{N-1} \sum_{j=i}^N C_{i,j} \Re \langle U_{n,i} E_i U_{n,j}^* E_j^* \rangle \\ &= \sum_{i=1}^N |U_{n,i}|^2 \Gamma_{i,i} + 2 \sum_{i=1}^{N-1} \sum_{j=i}^N C_{i,j} [\Re(U_{n,i} U_{n,j}) \cdot \Re \Gamma_{i,j} - \Im(U_{n,i} U_{n,j}) \cdot \Im \Gamma_{i,j}] \\ &\quad n = 1, \dots, M \end{aligned} \quad (3.17)$$

with  $U$  as the complex transfer matrix between input and output fields.

The coherence functions are rearranged on a vector of length  $N^2$  which results in

$$\vec{J} = (\Gamma_{1,1}, \dots, \Gamma_{N,N}, \Re \Gamma_{1,2}, \dots, \Re \Gamma_{N-1,N}, \Im \Gamma_{1,2}, \dots, \Im \Gamma_{N-1,N}) \quad (3.18)$$

This leads to

$$\vec{I} = \text{V2PM} \cdot \vec{J} \quad (3.19)$$

The V2PM has a size of  $M \times N^2$  with real valued entries. [60, 145]

The V2PM can be calibrated column wise. [146] Assuming the combination of 4 input beams, the calibration of the first 4 columns of the V2PM can be done by recording the output intensities of all waveguides for one injected field at a time. The

measured values can be normalized by the sum of the coefficients and sequentially fill the columns of the V2PM for every input injection point. The values connected to the last  $(N - 1)N$  columns, which means 12 columns for the combination of 4 telescopes, are retrieved by monitoring the output intensities of all waveguides when exciting each combination of 2 input waveguides at once while introducing a phase modulation  $\Delta\varphi_n$  to one of the input fields  $A_1$  and  $A_2$ . The output intensities are given by

$$I_n = \begin{aligned} & \text{V2PM}_{n1} \cdot |A_1|^2 + \text{V2PM}_{n2} \cdot |A_2|^2 \\ & + 2\sqrt{\text{V2PM}_{n1} \cdot \text{V2PM}_{n2}} |A_1| \cdot |A_2| \cdot V_{12} \cos(\varphi - \Delta\varphi_n) \end{aligned} \quad (3.20)$$

with the phase  $\varphi$  and the visibility  $V_{12}$ . The oscillatory term  $\tilde{I}_n$  can be isolated by subtracting the DC term  $\text{V2PM}_{n1} \cdot |A_1|^2 + \text{V2PM}_{n2} \cdot |A_2|^2$ , which leads to

$$\tilde{I}_n = a_n \cos(\varphi) + b_n \sin(\varphi) \quad (3.21)$$

while

$$a_n = \text{V2PM}_{n4} \cdot V_{12} \sqrt{|A_1|^2 \cdot |A_2|^2} \quad (3.22)$$

and

$$b_n = \text{V2PM}_{n5} \cdot V_{12} \sqrt{|A_1|^2 \cdot |A_2|^2} \quad (3.23)$$

can be obtained by fitting of the signal  $\tilde{I}_n$ .  $|A_1|$  and  $|A_2|$  are calculated as the sum of the output intensities of all waveguide outputs for exciting waveguide 1 and 2 separately. The coefficients  $\text{V2PM}_{n4}$  and  $\text{V2PM}_{n5}$  can be calculated.

The remaining columns can be filled in the same way using the output interference patterns for the other input waveguide combinations. To retrieve the searched  $\vec{J}$  vector the pseudo inverse of the V2PM (pixel to visibility matrix - P2VM [145]) has to be multiplied with the intensity matrix  $I_n$ .

To achieve the tolerance regarding measurement deviations the V2PM has to be well conditioned. The quantity describing this is the condition number (CN) that originates from the singular value decomposition (SVD). The SVD uses the fact that any  $M \times N$  matrix  $A$  with  $M \geq N$  can be written as the product of an orthogonal  $M \times N$  matrix  $U$ , the diagonal  $N \times N$  matrix  $W$  with positive or zero elements and the transposed  $N \times N$  orthogonal matrix  $V$

$$A = (U) \cdot \begin{pmatrix} w_0 & 0 & 0 & 0 \\ 0 & w_1 & 0 & 0 \\ 0 & 0 & \ddots & 0 \\ 0 & 0 & 0 & w_{N-1} \end{pmatrix} \cdot (V)^T . \quad (3.24)$$

The CN is the ratio of the highest and lowest non-zero values of the matrix  $W$ , the so called singular values. In the presence of measurement noise, more precise coherence functions can be retrieved for smaller CN. [59, 147]

The Michelson fringe visibility

$$V_{ij} = \sqrt{\frac{(\Re\Gamma_{ij})^2 + (\Im\Gamma_{ij})^2}{\Gamma_{i,i}\Gamma_{j,j}}}, \quad i \neq j \quad (3.25)$$

and its phase

$$\varphi_{ij} = \arctan \frac{\Im\Gamma_{ij}}{\Re\Gamma_{ij}} \quad (3.26)$$

can be computed using the V2PM. [148]

### 3.4 Interferometry using arrays of straight waveguides

It has been shown that DBCs consisting of a square waveguide array are suitable for the all-in-one beam combination of up to 4 telescopes. [58, 59] The necessity of NNN coupling for the retrieval of all field correlation functions proves the need of a 2D geometry for the DBC cross section. [61] Changing the waveguide array geometry to a zig-zag has two advantages. It can decrease the NNN coupling distance and therefore increase the coupling coefficients and it enables high resolution spectro-interferometry. The use of dispersing elements can generate a spectral image of every waveguide output. Due to the alternating waveguide order the spectra are well separated and not overlapping.

### 3.4.1 Design of zig-zag discrete beam combiners

The zig-zag DBC is a 2D array of straight evanescently coupled waveguides. The lattice consists of two planes of parallel waveguides separated by  $v$  which are shifted by half the horizontal spacing  $h$ . The resulting cross section of the array can be described as consecutive waveguides with a horizontal spacing of  $\frac{h}{2}$  starting at the bottom which have an alternating height of  $\pm\frac{v}{2}$ . This can be seen as a zig-zag order of waveguides, which is responsible for the name of the zig-zag DBC.

Knowing the horizontal and vertical coupling coefficients of different configurations of  $v$  and  $h$  from the experiments described in Section 3.2, the optimal parameters for the zig-zag DBC could be derived from the coupled wave equation, formulated in Section 3.2. The results indicate that for four input fields a configuration of 23 waveguides with  $h = 21 \mu\text{m}$  and  $v = 10.8 \mu\text{m}$  with 12 waveguides at the bottom and 11 waveguides at the top row is suitable for interferometric applications and gives the lowest CN at an array length of  $1.34 \cdot L_C$ . The input fields are injected at the inputs 5, 10, 14 and 19 (see Fig. 3.5).

To avoid the overlap of the input fields the waveguide array is equipped with input waveguides that connect the beginning of the DBC that starts inside the glass to the sample edge. [148, 149]

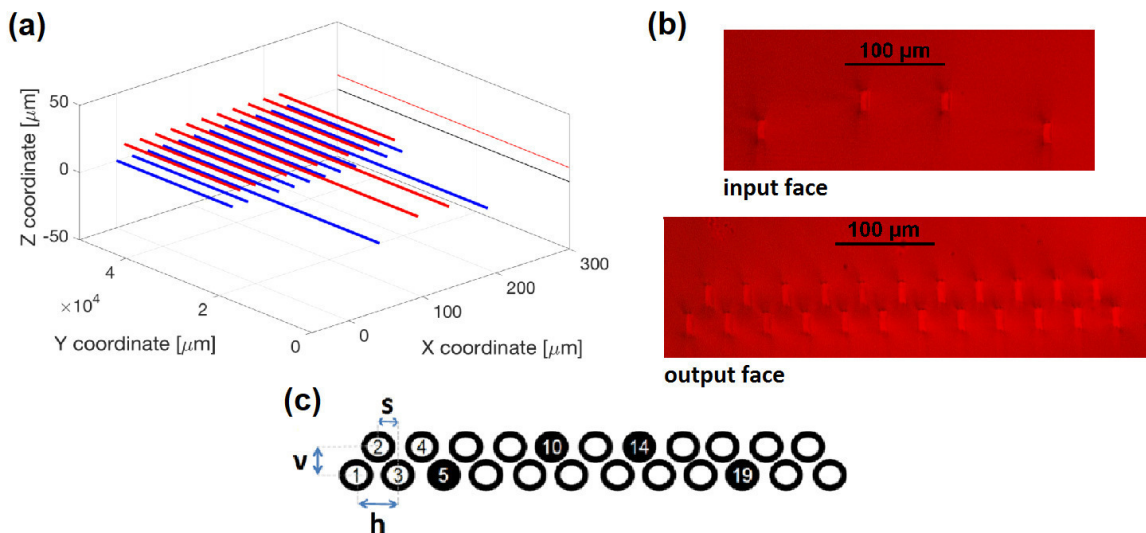


Figure 3.5: (a) Schematic sketch of the zig-zag waveguide array. [148] (b) Microscopic image of input and output face of the sample. [109, 149] (c) Cross section of the 23 waveguide zig-zag DBC configuration with input waveguide positions marked in black. [149]

In the experiment the length was varied to tune the coupling between the waveguides, because the coupling turned out to be smaller for more than 2 waveguides compared to the coupling measured for the directional couplers. Zig-zag arrays with 6 mm, 10 mm, 15 mm and 20 mm coupling lengths were fabricated.

The interferometric output patterns should be symmetrical for the illumination of symmetrical input configurations. This symmetry could not be observed, as can be seen in Fig. 3.6. Also the input polarization shows a strong dependency on the intensity distribution at the waveguide array output.

A variation of waveguide gap and length did not lead to a satisfactory symmetrization of the output pattern and an elimination of the polarization dependence in combination with sufficient coupling between waveguides, i.e. if a configuration showed a symmetric behavior as it is the case for  $h = 21 \mu\text{m}$ ,  $v = 10.8 \mu\text{m}$  and  $L = 6 \text{ mm}$ , due to the small interaction length, just 5 of the 23 waveguides are illuminated at the output of the array.

The problem was identified to be stress induced birefringence and yield that originates from the laser inscription process, mentioned in Section 2.4.3.

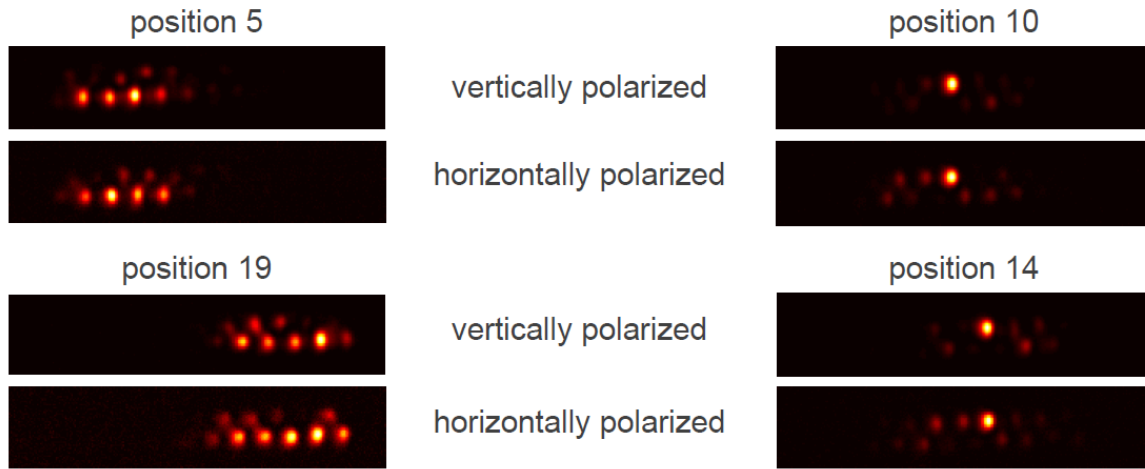


Figure 3.6: Comparison of output patterns with different injection points and orthogonal linear input polarizations for  $h = 21 \mu\text{m}$ ,  $v = 10.8 \mu\text{m}$ ,  $L = 15 \text{ mm}$ , 500 kHz, 500 fs,  $1 \frac{\text{mm}}{\text{s}}$ , 40 mW.



### 3.4.2 Stress management in zig-zag discrete beam combiners

For writing integrated photonic devices in glasses there is a need to put attention to stress management. As could be seen in Section 2.4.3 laser writing induces a stress field surrounding the modified area which leads to a local variation of the mechanical and optical properties of the glass.

Successful ways to control laser induced stresses in SiO<sub>2</sub> glass have already been accomplished. For example for increased deposited energy laser irradiation causes the formation of nano pores which leads to an expansion of the material and therefore counteracts the glass densification. [150] Additionally, the balance of stress birefringence by manipulation of the shape birefringence in laser treated material [151] and the depth dependence of the retardance size caused by birefringent behavior [152] have been shown. The change of the polarization angle of linearly polarized light during the waveguide writing process can also help in compensating the birefringence of the waveguides. [153] In SiO<sub>2</sub> the prediction and control of laser induced stresses for a couple of stressors has already been shown. [154]

When waveguides are arranged in a periodic lattice as it is the case for the zig-zag DBC stress control is very important. The physics of the interaction of the laser induced stress fields is quite complicated. As shown in Section 2.4.3 the stresses accumulate for an increased number of laser induced defects. The first waveguide has expected properties but material close to the waveguide location will experience a stress induced refractive index change. Writing a second waveguide in the affected area will result in a waveguide with properties different from the first one. The ultrafast laser inscription (ULI) of the later waveguides may effect a refractive index change of the former written waveguide, as well. The rise of the induced stresses was shown to be linear for up to 5 horizontally separated waveguides in Fig. 2.18.

The influence of the stress field on neighboring waveguides was determined by the fabrication and characterization of asymmetrical  $2 \times 2$  directional couplers. Since the propagation constant was shown to be non-zero (Section 3.2) for symmetrical couplers a change in writing parameters of the second written waveguide might compensate the stress-induced variation. The same symmetry for the directional couplers as in Section 3.2 was used, with one major difference: The translation speed of the sample was changed for the second waveguide.

Both slower and faster scanning was performed. While the first waveguide was always written with  $1 \frac{\text{mm}}{\text{s}}$  writing speed the scanning velocity for the following waveguide was varied from  $0.5 \frac{\text{mm}}{\text{s}}$  to  $2 \frac{\text{mm}}{\text{s}}$ . The gap between the waveguides was kept constant.

As described for symmetrical directional couplers in Section 3.2, the influence of mechanical stresses on the propagation constant of the second waveguide was determined by measuring the splitting ratio of couplers with different interaction lengths. To determine the splitting ratio of an asymmetric coupler [135] Eqn. 3.15 was used with Eqn. 3.10 as the effective coupling constant and  $\kappa$  as the coupling constant of an equivalent symmetrical coupler ( $\Delta\beta = 0$ ). Using the derived splitting ratios of all asymmetrical couplers with varying interaction lengths and speed differences, the model of Eqn. 3.15 could be fitted to obtain the corresponding values of  $\Delta\beta$  as a function of the writing speed difference  $\Delta v$ , see Fig. 3.7.

The sign of  $\Delta\beta$  was chosen according to the comparison of the MFDs of the two waveguides that are part of the coupler. When  $\text{MFD}_1 < \text{MFD}_2$  the sign was chosen to be negative and vice versa. For  $\Delta v = 0$  the sign could only be guessed from the trend of  $\Delta\beta$ .

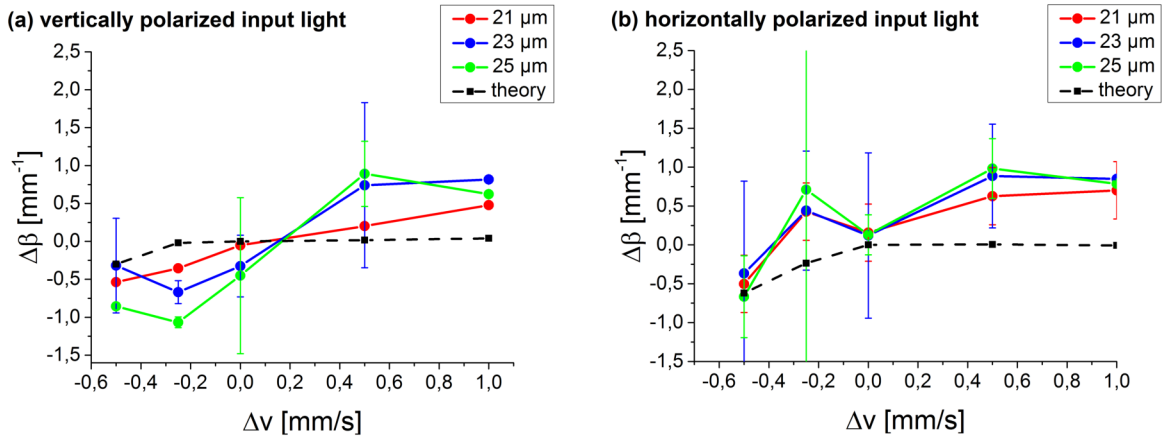


Figure 3.7: Change of propagation constant over writing speed difference of waveguide 2 with respect of waveguide 1 for (a) vertically polarized and (b) horizontally polarized input light.

The theoretical values were calculated from the simulated refractive index change  $\Delta n$  in Section 2.3 derived from the MFDs of the different waveguides using

$$\Delta\beta = \frac{2\pi}{\lambda} \cdot \Delta n_{\text{eff}} \quad (3.27)$$

with the wavelength  $\lambda = 3.39 \mu\text{m}$ . These results differ significantly from the measured values. Accordingly, the stresses induced to the material influence notably the  $\Delta\beta$  and therefore the coupling of the waveguides in the array and the effect of the laser writing to the material is significantly different in the stressed material.

At  $\Delta v = 0$  the data of  $\Delta\beta$  over  $\Delta v$  show a negative detuning of the second waveguide

with respect to the first one in the order of  $0.5 \text{ mm}^{-1}$  for all gaps. This could explain the light transfer asymmetry observed in the manufactured waveguide array. Accordingly, a compensation of the propagation constant difference and therefore the correction of the stress induced effects on the second waveguide should be possible when the translation speed of the sample is adjusted for every waveguide at a time. For further investigation 7-waveguide arrays with 3 different symmetrical input sites were written with ULI in Gallium Lanthanum Sulfide (GLS) with varying translation speeds for every following waveguide. The parallel waveguides had a gap of  $h = 23 \mu\text{m}$  and variable in length ( $L = 6, 10, 15, 20, 25$  and  $30 \text{ mm}$ ).

The manufactured device was tested by exciting one of the 7 waveguides at single input waveguides and observing the corresponding output diffraction pattern for both horizontal and vertical input light polarization with respect to the optical table (see Fig. 3.8).

When exciting the central input waveguide, the expected output pattern is symmetrical, and the output patterns of injection at the far left and far right waveguide should be mirror images of each other. The output diffraction patterns do not show the expected symmetry. Additionally, the output diffraction pattern is strongly dependent on the input polarization state for waveguide arrays longer than  $22 \text{ mm}$ . Considering the results from Fig. 2.18 and Fig. 3.7 an assumed linear change of translation speed might compensate the stresses and lead to a more symmetric and maybe even a polarization corrected output pattern. Indeed, applying a speed correction by increasing gradually the translation speed after the fabrication of one waveguide showed an improvement of both the symmetry and the polarization dependence of the interferometric output pattern. The best symmetry was achieved for the  $15 \text{ mm}$  long array and a translation speed correction of  $0.2 \frac{\text{mm}}{\text{s}}$ . The value of the subsequent speed difference was taken from the results in Fig. 3.7 and verified in the experiment (Fig. 3.8). For vertical input polarization the symmetry of the output patterns indicate that the coherence length is about  $22 \text{ mm}$ . This is the maximum array length that still allows the input beams to interfere with each other. A simultaneous correction for both orthogonal input polarizations with the described method is not possible.

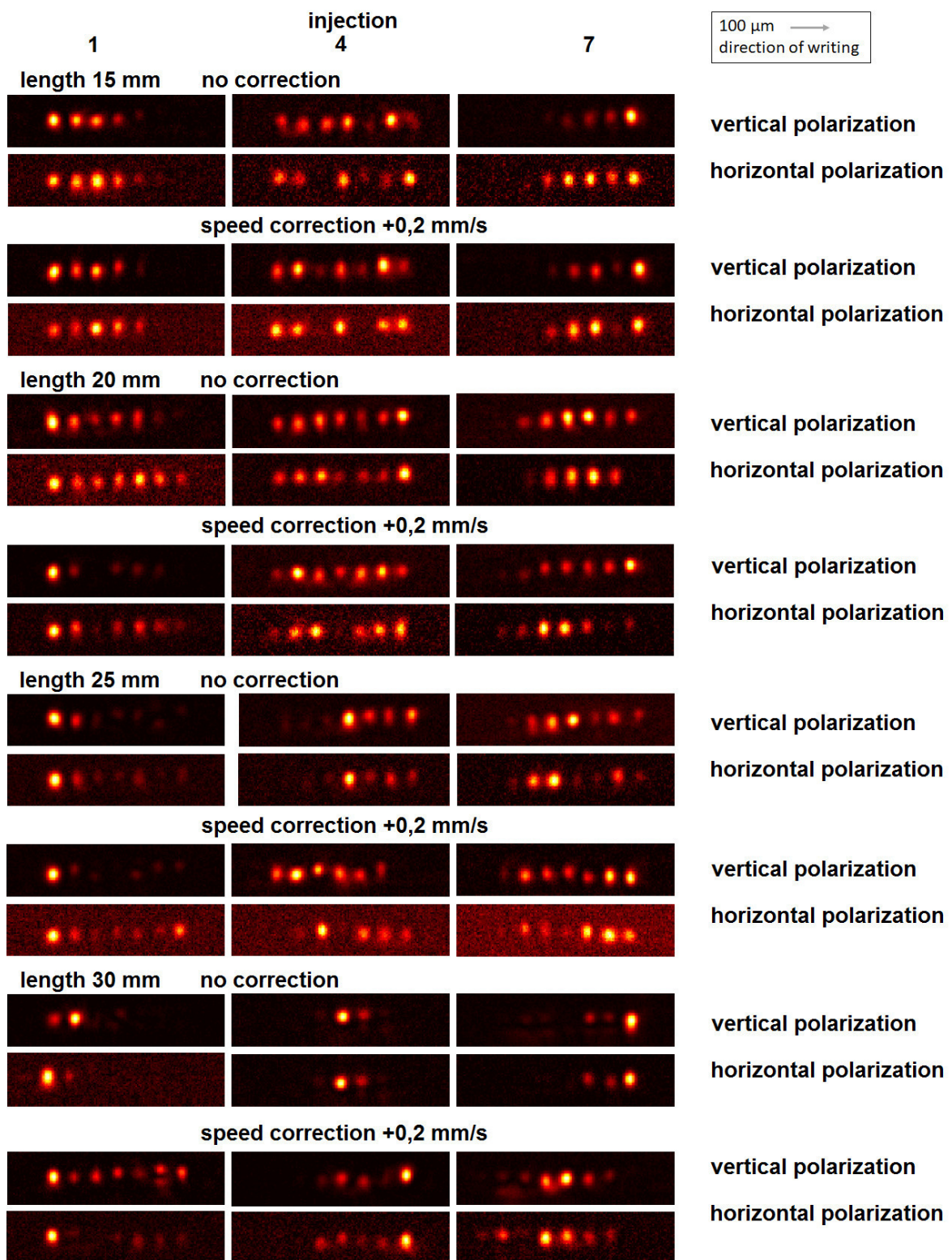


Figure 3.8: Intensity output patterns for 7 waveguide arrays with varying lengths and writing speed variation.

Several 23 waveguide zig-zag array configurations have been tested with the approach for stress compensation with a linear translation speed change, as well. The horizontal  $h$  and vertical  $v$  spacing of the waveguides were kept constant, consistently to the best working zig-zag DBC in Section 3.4 with  $h = 21 \mu\text{m}$  and  $v = 10.8 \mu\text{m}$ . The length  $L$  and the gradual translation speed difference in horizontal direction  $\Delta v$  were varied and the results were compared.

When injecting light into symmetrical input sites the output pattern is expected to be symmetrical. The orientation of the linear input polarization should have as little influence as possible to the resulting interferometric light distribution.

The best symmetry could be observed for  $L = 15 \text{ mm}$  and  $\Delta v = 0.15 \frac{\text{mm}}{\text{s}}$ . The corresponding output mode patterns are more symmetrical than without the stress correction. The assumed sign of  $\Delta\beta$  at  $\Delta v = 0$  in Fig. 3.7 was confirmed to be correct by the success of the stress compensation by variation of the writing speed by  $0.15 \frac{\text{mm}}{\text{s}}$ . The zero crossing point of  $\Delta\beta$  for a gap of  $21 \mu\text{m}$  is also located at this speed.

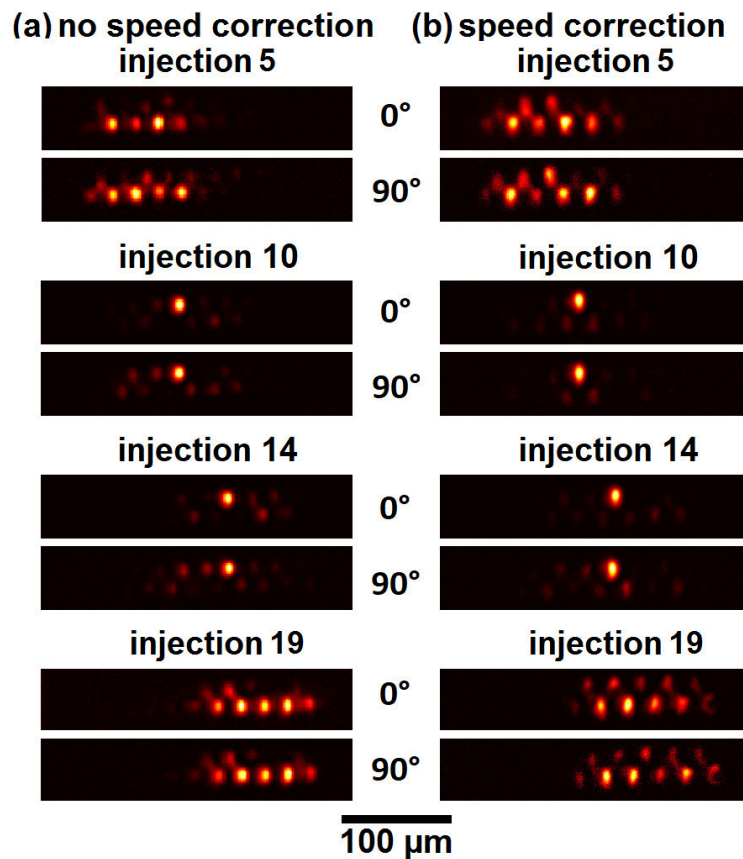


Figure 3.9: Interferometric output of zig-zag DBC with 20 mm length, a horizontal gap of  $h = 21 \mu\text{m}$  and a vertical gap of  $v = 10.8 \mu\text{m}$  (a) with no stress compensation, (b) with a gradual horizontal change of writing speed of  $0.15 \frac{\text{mm}}{\text{s}}$ .



### 3.4.3 Interferometric characterization of zig-zag discrete beam combiners

For the interferometric characterization of the zig-zag waveguide array the setup in Fig. 2.5 (b) was used to split the beam into two partial beams which can be focused to two different spots at the input plane of the DBC sample. The photometry of the waveguide outputs was recorded with an IR-camera.

For the demonstration of the results a 23 waveguide zig-zag DBC with horizontal waveguide gap of  $h = 24 \mu\text{m}$ , a vertical spacing of  $v = 10.8 \mu\text{m}$  and a length of 25 mm was chosen. The laser power in the ULI process was chosen to be 40 mW and the writing speed for the first waveguide is  $1 \frac{\text{mm}}{\text{s}}$  while the writing speed increased by  $0.075 \frac{\text{mm}}{\text{s}}$  for every waveguide according to the numbering in Fig. 3.5 (c), which corresponds to a speed difference of  $0.15 \frac{\text{mm}}{\text{s}}$  for waveguides separated by  $h$ .

According to the sequence of steps described in Section 3.3 the V2PM has been calculated. First, only one input waveguide is illuminated to derive the first 4 columns of the  $16 \times 23$ -entries. The output intensities for all 23 waveguides for the injection of the 5<sup>th</sup>, 10<sup>th</sup>, 14<sup>th</sup> and 19<sup>th</sup> waveguide were measured and the total output intensities for every injection were calculated as the sum of the single output intensities of each waveguide. The normalization of these values by the total output intensity produces the first 4 columns of the V2PM. The second step is injecting two different input waveguides simultaneously to calculate the missing entries for the columns 5 to 16.

baseline	input waveguides
1	5 + 10
2	5 + 14
3	5 + 19
4	10 + 14
5	10 + 19
6	14 + 19

Figure 3.10: Waveguide input combination corresponding to the baseline number.

One of the two beams is delayed by a movable mirror. The mirror is installed on a one-dimensional translation stage that moves with  $1 \frac{\mu\text{m}}{\text{s}}$  speed.

The output modes are recorded by the infrared-camera with a rate of 30 Hz over at least 5 fringes. The recorded intensities periodically increase and decrease following

sinusoidal oscillations. The recorded interference pattern is fitted for each output over frame number  $x$  with a combined cos-sin-function:

$$I_n = a_n \cdot \cos(\omega \cdot x) + b_n \cdot \sin(\omega \cdot x) + I_0 \quad (3.28)$$

with the frequency of phase modulation  $\omega$ , an offset  $I_0$  and the amplitudes  $a_n$  and  $b_n$ . The values for the corresponding baselines (see Table 3.10) can be obtained with Eqn. 3.22 and Eqn. 3.23 from the fitted parameters. The columns are filled respectively; 2 columns per baseline. The V2PM is illustrated in Fig. 3.11.

The CN of this DBC is 14.13 and was calculated as described in Section 3.3.

Several parameter configurations were tested and the corresponding V2PM were calculated. The quality of the beam combiners is confirmed by a low CN.

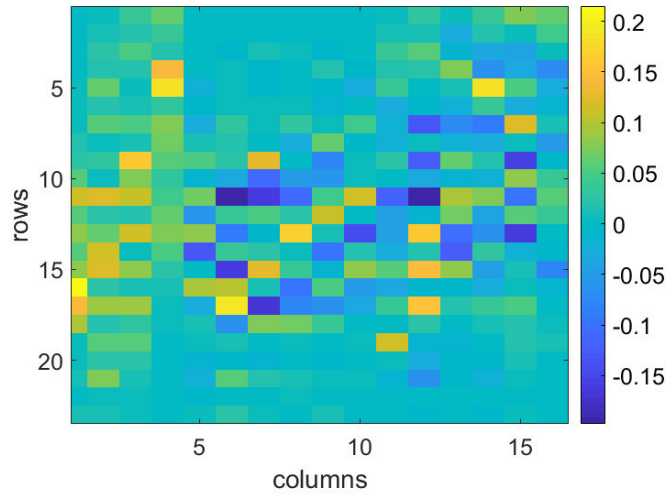


Figure 3.11: V2PM of a zig-zag DBC with  $h = 24 \mu\text{m}$ ,  $v = 10.8 \mu\text{m}$  and  $L = 25 \text{ mm}$ .

The instrumental visibilities were estimated from the obtained V2PM. Fig. 3.12 illustrates the Michelson visibility of the different baselines. Referring to Eqn. 3.25 the root of the squared sum of the sin- and cos- coefficients  $\sqrt{(\Re\Gamma_{1,2})^2 + (\Im\Gamma_{1,2})^2}$  over the root of the corresponding photometry  $\sqrt{\Gamma_{1,1} \cdot \Gamma_{2,2}}$  was plotted and the visibilities were determined by a linear fit of the values. For baseline 1, 2 and 3 the instrumental visibilities were estimated to be  $0.877 \pm 0.018$ ,  $0.892 \pm 0.020$  and  $0.931 \pm 0.033$  while the baselines 4, 5 and 6 showed instrumental visibilities of  $0.971 \pm 0.042$ ,  $0.885 \pm 0.010$  and  $0.863 \pm 0.030$ . A reason of the not ideal performance of the instrument can be the birefringence of the input waveguides, which introduces a change in the polarization state, as described in Section 2.3. The length of the input waveguides might have a non-negligible influence to the performance of the device and has to be investigated.

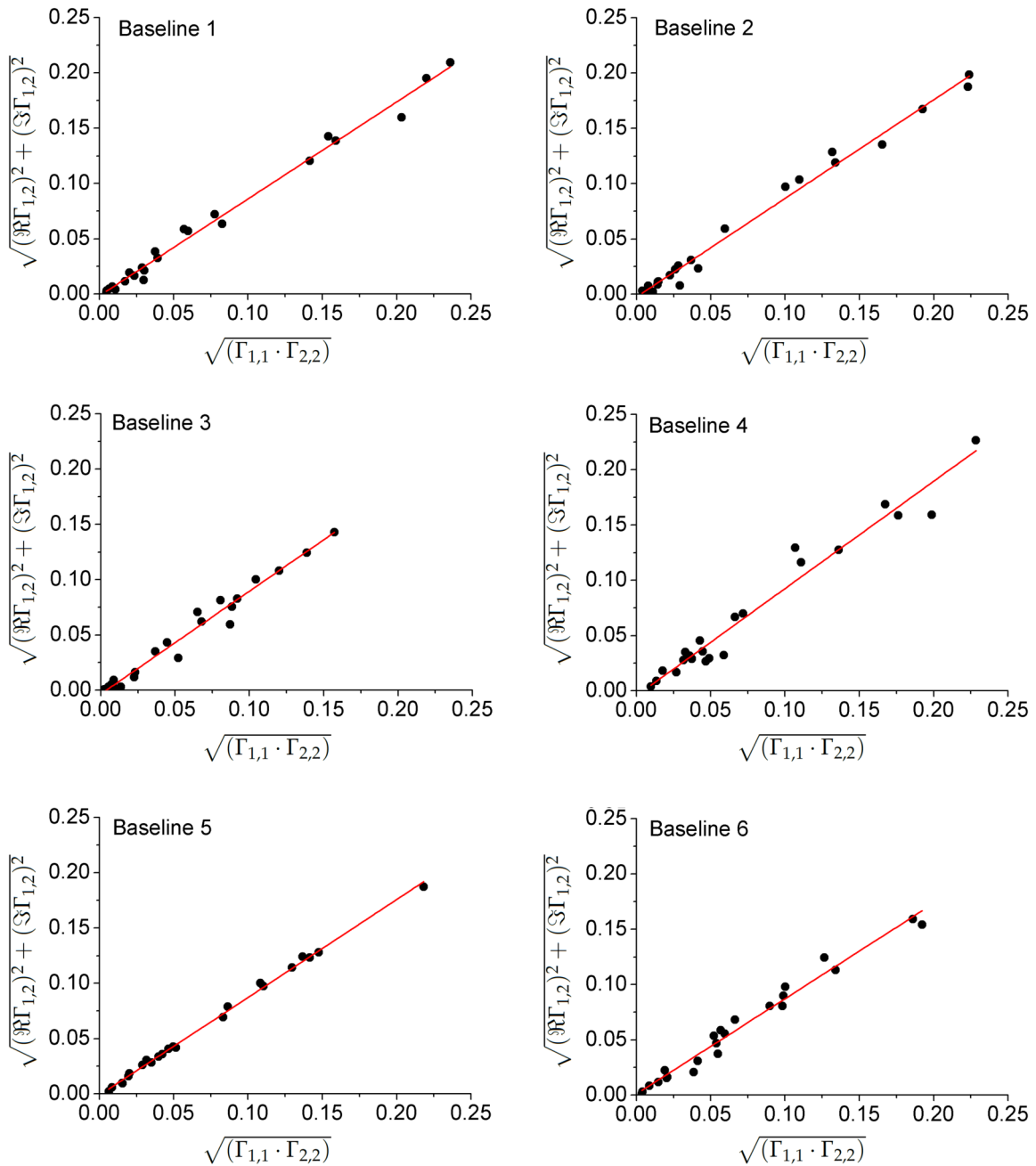


Figure 3.12: Illustration of the Michelson visibility for the baselines 1 to 6.

Using the P2VM which is the pseudo-inverse of the V2PM the coherence functions  $\Gamma_{ij}$  of the 6 baselines were retrieved from the photometric data. The results are summarized in Fig. 3.13. Shown are the ratios of the imaginary and the real part (quadrature) of the measured coherence functions in blue and the expected distribution of complex visibilities, which correspond to the radii of the circles. The complex visibilities are ranging from 0.95 to 1.04.

The signal to noise ratio (SNR) which is the ratio between the levels of the signal



and the background noise, varied from 12 to 25 which is only by a factor of 2 lower than the SNR of the GRAVITY instrument [146]. This verifies the stability of the retrieval algorithm. Since the expected CN of the V2PM is not matching the simulated value of 3.6 and a decrease of the SNR should be possible, there is still room for improvement of the device also in order to achieve a higher sensitivity, which is very important for the observation of faint astronomical objects. [148, 149]

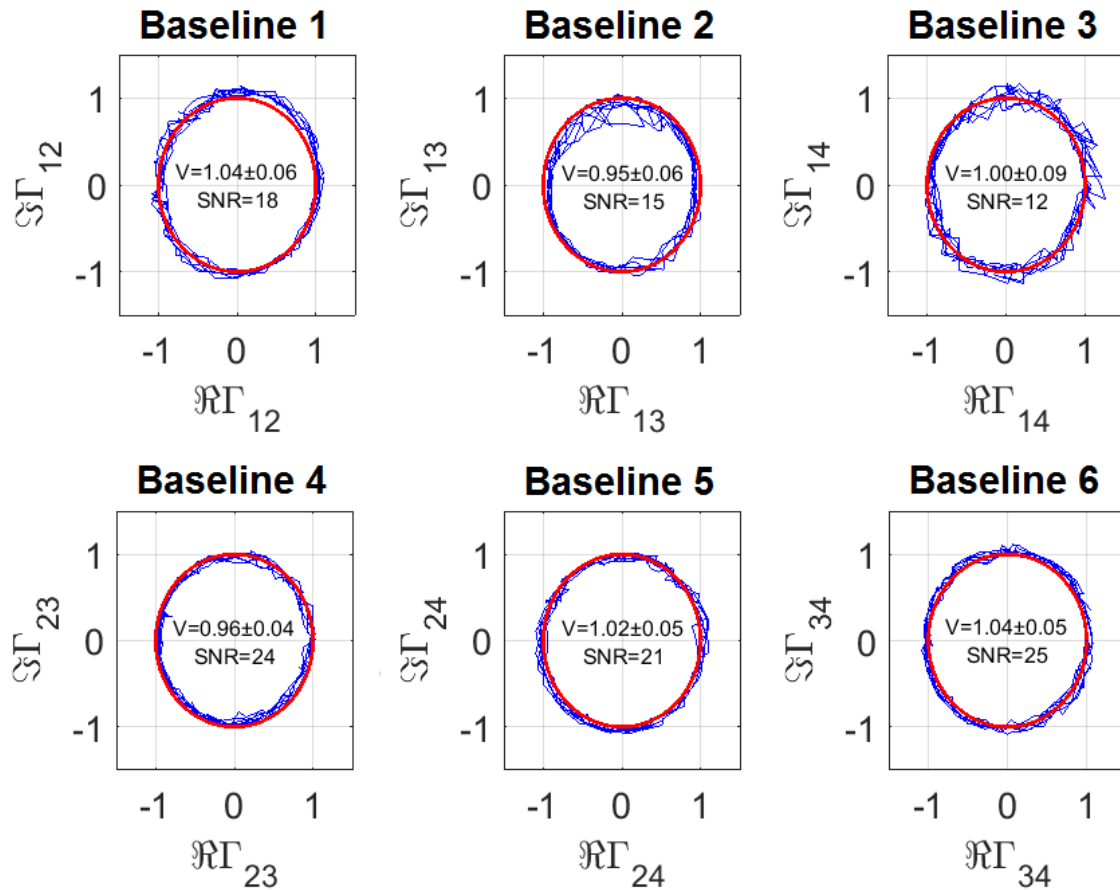


Figure 3.13: Quadrature of the coherence functions (or complex visibilities) of the 6 possible baselines (combinations of waveguide inputs). The red circles express expected distributions of coherence function; the blue lines exhibit the measured quadrature of the coherence function. [148]

The measured and expected phase differences are corresponding to the delay of the beams shown in Fig. 3.14 are in good agreement. The residuals of the measured phase compared to the expected phase are very small and illustrate that the retrieved linear phase ramp has a standard deviation ranging from 0.13 to 0.17 rad. The delay mirror positioning stage has an accuracy of 50 nm. [148, 149]

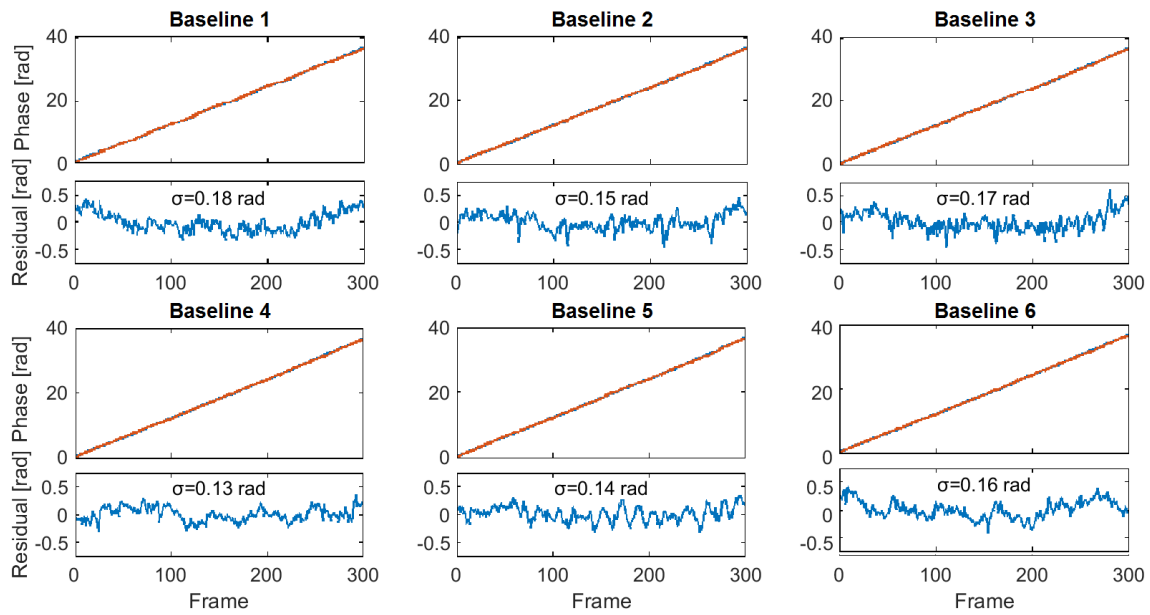


Figure 3.14: Retrieved phase (top) and deviation of input fields from linearity (bottom) over frames for the 6 possible baselines of the 4 input fields DBC. [148, 149]

### 3.5 Direct beam combination with the ABCD configuration

ABCD beam combination is a 4 level phase shifting device used for the determination of the phase of an interference pattern [155]. The interferometry fringes are sampled with 4 phases, each separated by  $\frac{\pi}{2}$ . The ABCD concept is implemented in the GRAVITY beam combiner. [16]

The ABCD beam combiner allows the interferometric combination of 2 input fields. It has 4 input sites 1, 2, 3, and 4. First, each waveguide is split in 2 by a 50/50 beam splitter with the design shown in Section 3.2. Respectively, two waveguides are brought together from a  $170.5 \mu\text{m}$  gap at the input face to  $20.5 \mu\text{m}$  using 7 mm long double raised-sine s-bends of a dislocation of  $h = 75 \mu\text{m}$  at each bend which have a 4-mm-long straight section attached and afterwards the waveguide gap returns to their original positions. This beam splitter is followed by a 50/50 directional coupler of channels 1-3 and 2-4. ULI has the advantage that x-crossings can be avoided by the usage of two double s-bends in vertical direction. This limits cross talk between the fields guided by the crossing waveguides at the crossing point. By bending waveguide 2 in negative and waveguide 3 in positive horizontal direction by  $50 \mu\text{m}$  over a length of  $l = 7 \text{ mm}$  they can be crossed without interaction. They are

then brought back together with the corresponding outer waveguides in the original vertical position to a gap of  $20.5 \mu\text{m}$  before being separated to a distance of  $80.5 \mu\text{m}$  at the output face of the sample, using a double-s-bend with the dislocation of  $30 \mu\text{m}$  and a length of  $5 \text{ mm}$ .

The waveguides 1 and 4 have been designed to undergo the same  $z$ -displacement in order to avoid optical path differences in the waveguide array.

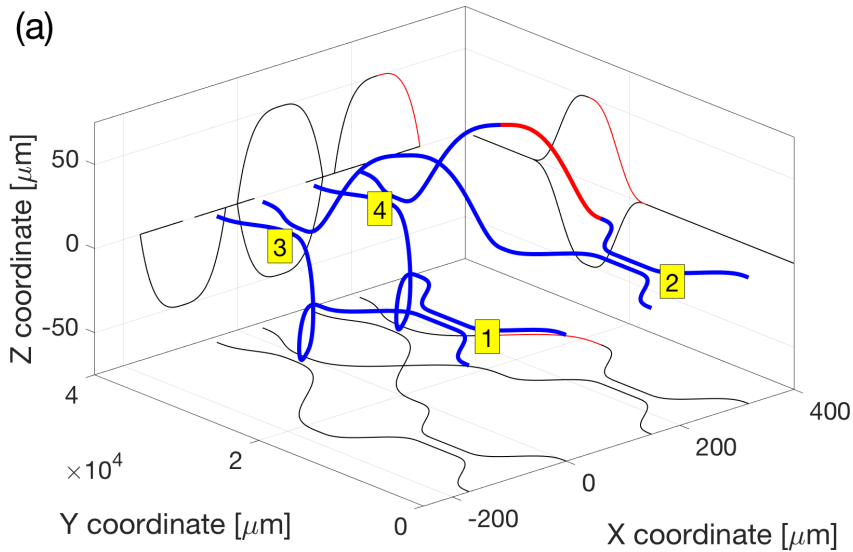


Figure 3.15: Schematical top view of the ABCD beam combiner designed for interferometric 2 beam combination. [148]

The necessary  $\frac{\pi}{2}$ -phase-shift is introduced to the field in channel 1 by local variation of writing speed, which varies the refractive index, as shown in Section 2.3. In channel 1 two 2.5-mm-long straight taper sections are surrounding a 1.2-mm-long section with the maximum writing speed of  $1.4 \frac{\text{mm}}{\text{s}}$ . Waveguides 2, 3 and 4 experience no speed modification. This writing speed increase lowers the propagation constant for the particular length. These values were estimated from the results of the  $\Delta\beta$  measurements in asymmetric couplers (Section 3.4.2).[148]

The photometric measurement results were obtained by Jan Tepper at the University of Cologne. The V2PM was then be calibrated in the way that is described in Section 3.3. For the excitation of one waveguide input, the output intensity distribution is uniform. Because the first two columns of any ABCD combiner V2PM are identical, the CN becomes infinite. A visibility of  $V_{1,2} = 0.92 \pm 0.06$  with a SNR of 28 has been be measured.

The last two columns of the V2PM can be used to determine the phase delay that is induced by the phase shifter. The matrix elements are proportional to the quadratures

of the cross products of the field transfer function. The phase shift was determined to be 2.2 rad which is higher than optimal (1.6 rad). The measured standard deviation of the phase delay residuals is 0.2 rad which mainly originates in the nonlinearity of the mechanical delay line. [148]

The reason for the deviation from optimal performance is the high bending losses of the device. Because the double s-bends of the ABCD combiner exhibit additional bending losses and the straight waveguides only suffer from propagation losses, the overall losses of the ABCD component are higher compared to the zig-zag DBC. The instrumental visibility is about 30%. It can be improved by controlling the birefringence and lowering the bending losses by changing the bending geometry.

# Chapter 4

## Nonlinear properties of gallium lanthanum sulfide glass

Gallium lanthanum sulfide (GLS) glass is a highly nonlinear material which can be used for applications besides stellar interferometry. In this chapter, the nonlinearity of GLS is studied and the applicability for supercontinuum generation is discussed. First an introduction to nonlinear properties of the material is given, followed by the derivation of the propagation equation of electromagnetic waves in nonlinear materials. Furthermore, the inelastic Raman scattering is specified and the measurement of the Raman response is described. The Raman fraction and the Raman gain were retrieved from the experimental results and compared to the obtained values from wave propagation simulations.

The aim is to investigate the influence of the Raman effect during shock wave generation on supercontinuum generation.

### 4.1 Supercontinuum generation

Common lasers radiate coherent light at one wavelength or a wavelength range of a few nanometers. In the case of the generation of white light, this small range is extended to the whole visible spectrum and into the infrared. Spectrally broadened coherent light is called a supercontinuum. It is a complex nonlinear phenomenon which can be achieved by spectral broadening of laser pulses in a nonlinear material. [156, 157]

A supercontinuum was first observed in bulk silica in 1970 [158, 159] and has been extended to other materials, such as solids [159–161], fluids [160, 162–164] and gases

[165–167], fibers [168, 169] and waveguide structures [170].

The spectral broadening can be achieved using self-phase modulation of laser beams that are focused into waveguides. Since, the field intensities can be maintained and the nonlinearity is enhanced, the supercontinuum generation is easier accomplished in waveguides and fibers than in bulk materials. The supercontinuum generation in waveguides results from the generation of new spectral components by Raman scattering, four wave mixing and their interplay. Supercontinua can be generated by focusing femtosecond laser pulses in waveguides or fibers. [157, 171]

## 4.2 Nonlinearity of transparent materials

Nonlinear effects occur when intense electromagnetic radiation is focused into a material with a high nonlinearity. The origin lies in the inharmonic motion of bound electrons during the absorption process. The nonlinear polarization is described by evaluating the  $n^{\text{th}}$  Taylor expansion of the polarization  $P$  in powers of the electric field strength  $E$

$$P = \epsilon_0(\chi^{(1)}E + \chi^{(2)}E^2 + \chi^{(3)}E^3 + \dots + \chi^{(n)}E^n) \quad (4.1)$$

with  $\epsilon_0$  being the vacuum permittivity,  $\chi^{(i)}$  the  $i^{\text{th}}$  order susceptibility. The linear susceptibility is represented by  $\chi^{(1)}$ . The second order susceptibility  $\chi^{(2)}$  is responsible for effects such as second harmonic generation and sum frequency generation [172].  $\chi^{(2)} = 0$  for centro-symmetric materials as glasses. In turn,  $\chi^{(3)}$  is responsible for third-harmonic generation and four wave mixing.

The Kerr effect is a third order nonlinear effect that describes the intensity dependent refractive index. It originates from nonlinear refraction:

$$n(\omega, I) = n_0(\omega) + n_2I \quad (4.2)$$

with  $n_0(\omega)$  as the linear refractive index,  $I$  as the optical intensity and  $n_2$  as the nonlinear refractive index. The third order susceptibility  $\chi^{(3)}$  is connected to the nonlinear refractive index  $n_2$  by

$$\chi_{\text{real}}^{(3)} = \frac{4}{3}n_0^2\epsilon_0cn_2 \quad (4.3)$$

with the index indicating the real part of  $\chi^{(3)}$ . [173] The intensity dependence of the refractive index results in the self-phase modulation of the electromagnetic wave.

The self-induced phase shift is determined by using

$$\Phi_{\text{NL}} = n_2 k L I \quad (4.4)$$

with the waveguide length  $L$  and the wavenumber  $k = \frac{2\pi}{\lambda}$ . The generation of new frequencies for pulsed laser light is possible because the laser intensity in the medium becomes time dependent. This leads to bandwidth broadening

$$d\omega(t) = -\frac{d\Phi_{\text{NL}}(t)}{dt} = -n_2 k L \frac{dI(t)}{dt} . \quad (4.5)$$

For  $n_2 > 0$ , the leading part of the pulse ( $\frac{dI(t)}{dt} > 0$ ) is decreasing in frequency and the tailing part ( $\frac{dI(t)}{dt} < 0$ ) is increasing in frequency. [174]

Nonlinear absorption occurs due to an electric current that is responsible for an ionization of the medium. The material ionization leads to a plasma generation. In any case, nonlinear effects occur due to stimulated elastic scattering. Energy transfer from field to material is taking place for effects such as stimulated Raman scattering (SRS) which induces optical phonons in forward direction, and stimulated Brillouin scattering (SBS) which results in acoustical phonons travelling backwards. [175, 176] [157, 177]

### 4.3 Derivation of the propagation equation

Maxwell's equations for dielectric media read

$$\nabla \times \vec{E} = -\frac{\partial \vec{B}}{\partial t} \quad (4.6)$$

and

$$\nabla \times \vec{B} = \mu_0 \left( \vec{J} + \frac{\partial \vec{D}}{\partial t} \right) \quad (4.7)$$

with  $\vec{E}$  and  $\vec{B}$  as electric and magnetic field and  $\vec{J}$  as the current density of free charges. The polarization is given by

$$\hat{P}(\vec{r}, \omega, z) = \epsilon_0 \chi(\omega) \hat{E}(\vec{r}, \omega, z) \quad (4.8)$$

with  $\hat{E}$  as the Fourier transformation of  $\vec{E}$  and the dielectric displacement by

$$\hat{D}(\vec{r}, \omega, z) = \epsilon_0 \epsilon(\omega) \hat{E}(\vec{r}, \omega, z) + \hat{P}(\vec{r}, \omega, z) \quad (4.9)$$

where  $\epsilon(\omega) = 1 + \chi(\omega)$  describes the relative permittivity of the medium. The wave equation in the frequency domain then reads

$$\nabla^2 \hat{E} - \nabla(\nabla \hat{E}) + \frac{\omega^2 n^2(\omega)}{c^2} \hat{E} = \mu_0(-i\omega \hat{J} - \omega^2 \hat{P}) \quad (4.10)$$

with  $c$  as the speed of light in vacuum,  $\mu_0$  as the vacuum permeability,  $n$  as the refractive index and  $\omega$  as the frequency. Assuming the linear polarization of the electric field is transverse to the propagation axis means that the  $\nabla(\nabla \hat{E})$ -term can be neglected. [178]

To further simplify the derivation of the propagation equation, the slowly varying envelope approximation (SVEA) can be used as long as the envelope has a time scale that is much larger than the carrier oscillation scale, so the fields are considered nearly monochromatic. The spectrum is centered at the carrier frequency  $\omega_0$  and the spectral width is  $\Delta\omega$  so that  $\frac{\Delta\omega}{\omega_0} \ll 1$ . The propagation constant is derived by

$$\beta(\omega) = n(\omega) \frac{\omega}{c} = \beta_0 + (\omega - \omega_0)\beta_1 + \frac{1}{2}(\omega - \omega_0)^2\beta_2 + \frac{1}{6}(\omega - \omega_0)^3\beta_3 + \dots \quad (4.11)$$

with

$$\beta_n = \left( \frac{d^n \beta}{d\omega^n} \right)_{\omega=\omega_0} . \quad (4.12)$$

For a pulse duration longer than 100 fs only the terms up to  $\beta_2$  are relevant, which leads to

$$\frac{\partial A(z,t)}{\partial z} + \beta_1 \frac{\partial A}{\partial t} + \frac{i}{2}\beta_2 \frac{\partial^2 A}{\partial t^2} + \frac{\alpha}{2}A = i\gamma|A(z,t)|^2 A(z,t) \quad (4.13)$$

with the nonlinearity coefficient  $\gamma = \frac{n_2\omega_0}{cA_{\text{eff}}}$ , the effective core area  $A_{\text{eff}}$ , the envelope  $A(z,t)$  of  $E(z,t)$

$$A(z,t) = \frac{1}{2} \sqrt{c_n \epsilon \epsilon_0} E(z,t) \cdot \exp(i(\omega_0 t - \beta_n(\omega_0)z)) \quad (4.14)$$

with  $c_n$  as the velocity of light in the material,  $\epsilon$  as the dielectric constant,  $\epsilon_0$  as the vacuum permittivity,  $\alpha$  as propagation losses,  $\beta_1$  as the group delay and  $\beta_2$  describing the group delay dispersion. [157, 177]



## 4.4 Inelastic Raman scattering

Inhomogeneities in solid media that are comparable in size to the wavelength of the transmitted radiation scatter incoming light. If the homogeneity is only spatial, elastic scattering is taking place. If also temporal perturbations occur, sidebands in the scattered spectrum appear which belong to inelastic scattering. Raman or Brillouin scattering can be the origin. Planck [179] and Einstein [180] laid the foundation for the consideration of light as a particle wave. Since photons carry energy and momentum they can participate in inelastic scattering and exchange energy or momentum with the scattering medium. In 1923 Smekal [181] was the first to theoretically predict sidebands in the scattered spectrum. The observation of the effect followed in 1928 by Raman and Krishnan [182] in benzene. The proof that the Raman effect also occurs in solids was done by Landsberg and Mandelstam [183]. Soon, the new effect was used for material studies. [184] The mercury arc became the most-used light source, first with photographic and then with spectrophotometric detection. A catalog of molecular vibrational frequencies could be measured. [185] To investigate the influence in shock wave generation for supercontinuum generation the Raman coefficient needs to be found. General aspects of the Raman effect were introduced in Section 2.4.2 of this work.

Raman gain can be described as the time-dependent nonlinear refractive index. When high-intensity pulses perturb the electronic structure of a molecule, the polarizability of the molecule changes or the refractive index becomes intensity dependent. This laser-induced electronic perturbation also has an effect on the field that the nucleus of the molecule experiences. Therefore, the perturbation can excite molecular vibrations. The Raman effect describes the intensity-dependent polarizability connected to the molecular vibrations. [186]

GLS is a highly nonlinear material with a nonlinearity that is 2-3 times higher than the nonlinearity of silica. [108] The Raman response function is necessary to predict the nonlinear response of the material. The understanding of nonlinear processes can help in finding optimal laser writing parameters for ultrafast laser inscription (ULI).

Introducing higher dispersion terms for ultra short pulses [187] and the Raman gain in Eqn. 4.14, low frequency components can be amplified by the energy transfer from higher frequency components, which results in a red shift. [188, 189]

The nonlinear Schrödinger equation is described by

$$\begin{aligned} \frac{\partial A(z, t)}{\partial z} = & - \frac{\alpha}{2} A + i \sum_{n \geq 1} \frac{i^n \beta_n}{n!} \frac{\partial^n A}{\partial t^n} \\ & + i\gamma \left( 1 + \frac{i}{\omega} \frac{d}{dt} \right) A(z, t) \int_0^\infty R(t') |A(z, t - t')|^2 dt' \end{aligned} \quad (4.15)$$

with  $t'$  from the retarded medium response. The first term contains the losses, the second term takes higher order dispersion into account and the first bracket in the third term belongs to self-phase modulation, four-wave mixing and Raman, while the second bracket describes self-steepening. The nonlinear response  $R(t)$  includes the Raman term

$$R(t) = g_0 \int_0^\infty S(\omega) \cdot \sin(\omega t) d\omega \quad (4.16)$$

which is obtained by the Raman signal  $S$ . [157, 177]

#### 4.4.1 Measurement of the Raman response

The Raman response function can be retrieved by the measurement of the Raman spectrum (Section 2.4.2) and Raman gain of a waveguide core, connected with derivation of the nonlinear coefficient  $n_2$ . The Raman gain at a pump laser was determined by the experiment shown in Fig. 4.1. The pump laser source is a Light Conversion NOPA (Non-collinear optical parametric amplifier) which is pumped by a picoREGEN picosecond-laser by HIGH Q LASER with a seed wavelength of  $\lambda_{\text{seed}} = 1.58 \mu\text{m}$  and a pulse length of  $T_{\text{seed}} = 80 \text{ fs}$ . The seed comes from a continuous wave diode laser. The beam originating from the laser system has a pulse length of  $T_{\text{laser}} = 2.67 \text{ ps}$  with a repetition rate of  $f_{\text{laser}} = 5 \text{ kHz}$  and a wavelength of  $\lambda_0 = 1.55 \mu\text{m}$ . The power is tuned by a  $\frac{\lambda}{2}$  plate and the beam is focused to the waveguide input face with a 50 mm lens generating a Gaussian beam waist of  $w_0 = 15.11 \mu\text{m}$ . The sample is located on a positioning stage which gives the possibility of achieving a measured net input coupling to the waveguide of  $\eta_{\text{wg}} = 0.68 \pm 0.05$  considering a Fresnel loss at the surface of  $\eta_{\text{Fresnel}} = 0.83$ .

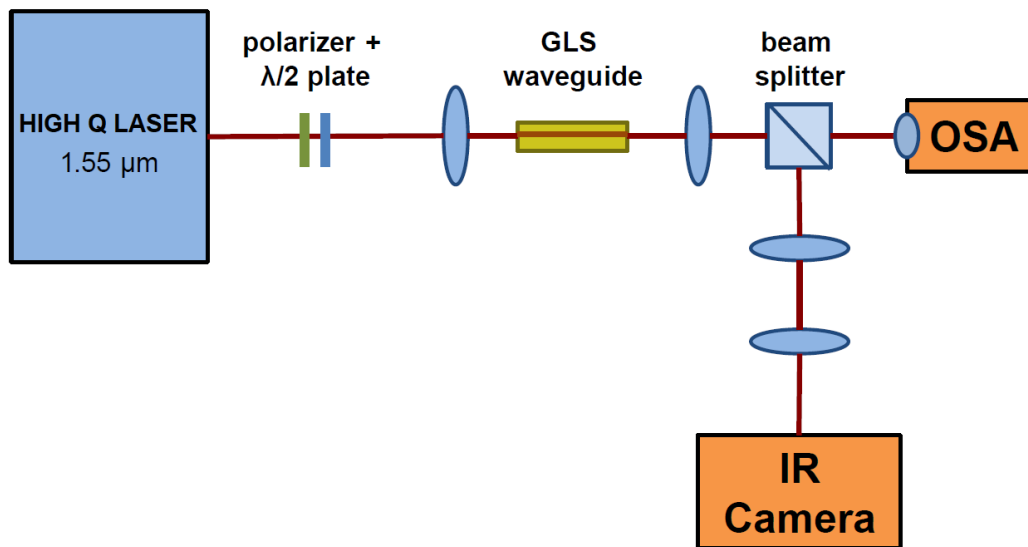


Figure 4.1: Setup for the measurement of the nonlinear response of the waveguide material to laser pulses.

The output radiation of the waveguide can be observed by an infrared camera. This way the alignment of the waveguide can be checked. A beam splitter allowed the simultaneous measurement of the optical spectrum with an optical spectrum analyzer (OSA).

The Raman spectra of GLS waveguides have been discussed in Section 2.4.2. The inverse Fourier transform of the Raman gain  $g(\Omega)$  gives the Raman response in the time domain

$$h_R(t) = \text{FT}^{-1}(g(\Omega)) \quad . \quad (4.17)$$

The response function is an exponentially decaying sinusoidal oscillation. The frequency of the Raman gain peak can be extracted from the oscillation period and the width of the gain spectrum can be obtained from the decay rate. [186]

The response function is related to the nonlinear polarization. [190] The third order susceptibility is proportional to the Raman gain coefficient. [191] Furthermore, the response function can be obtained directly from the real part of the nonlinear refractive index  $n_2$ .

The nonlinear refractive index can be derived from the spectral broadening of the pump pulse as function of the input power. Compared with the pulse propagation simulation, which uses 1D pulse propagation while taking into account the material dispersion and the nonlinear Kerr response.

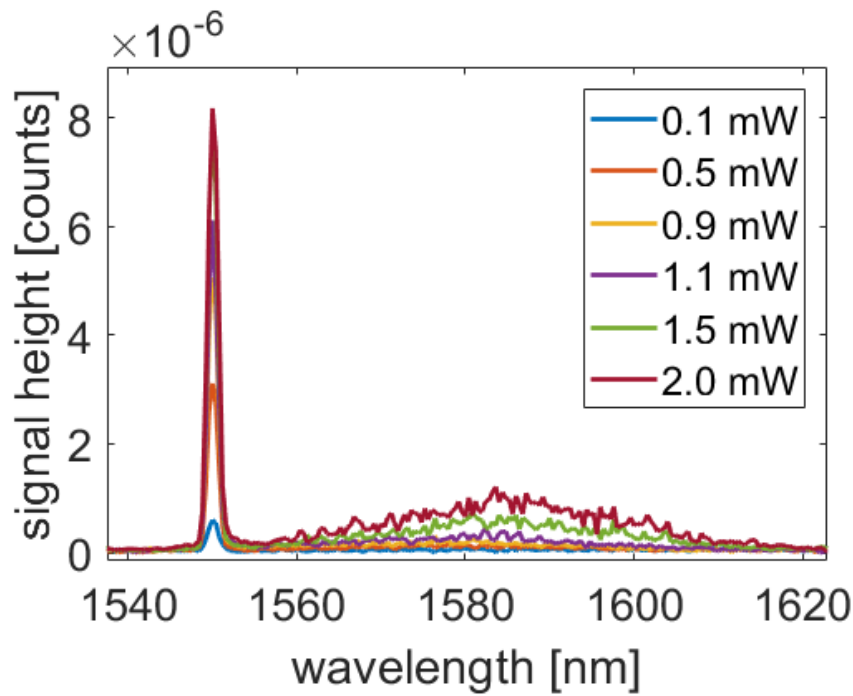


Figure 4.2: Measured spectrum of Raman response obtained from a 7 mm long waveguide in GLS glass for different laser irradiation powers.

The measured spectrum is shown in Fig. 4.2. It can be used to determine the spectral broadening of the main pulse at  $1.55 \mu\text{m}$  (Fig. 4.3 (a)) over the input power which is measured by a power meter in front of the sample, as well as, the peak amplitude of the Raman background irradiation at  $1.58 \mu\text{m}$ , which corresponds to the frequency shift of the pump laser of  $140 \text{ cm}^{-1}$  (Fig. 4.3 (b)).

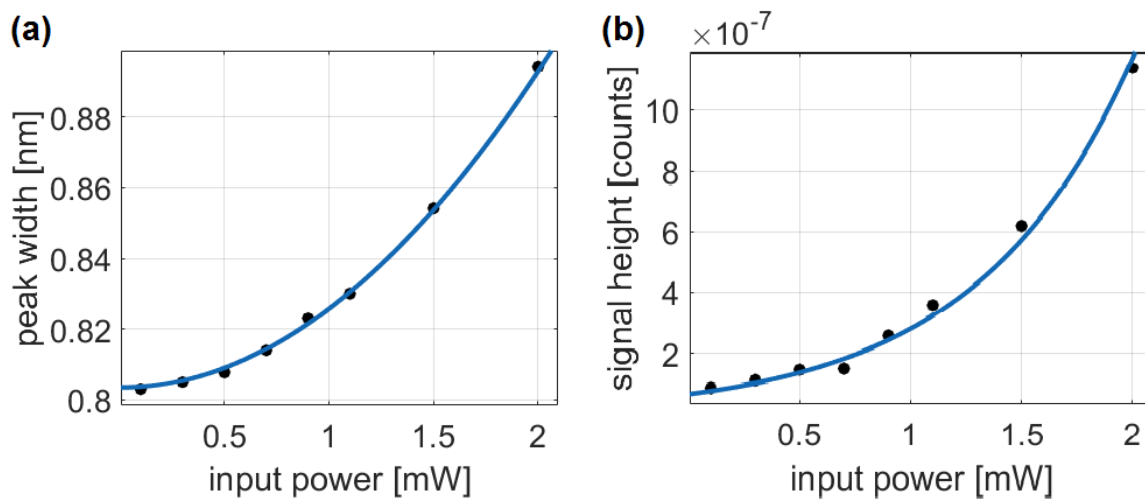


Figure 4.3: (a) Laser peak widths  $\sigma$  (at  $1.55 \mu\text{m}$ ) over laser input power. (b) Peak heights (at  $1.58 \mu\text{m}$ ) over laser input power.

The Raman fraction is estimated using

$$f_R = \frac{\lambda_0}{2\pi^2 n_2} \int_0^\infty R(t) dt. \quad (4.18)$$

The measured gain  $g_0 = (7.37 \pm 1.00) \cdot 10^{-12} \frac{m}{W}$  was obtained by the fit of the measured Raman signal peak heights

$$S_{\text{peak}} = \exp(g_0 L I_0) \quad (4.19)$$

as a function of the input intensity

$$I_0 = \eta_{\text{wg}} \eta_{\text{Fresnel}} \cdot \frac{P_{\text{laser}}}{f_{\text{laser}} \pi^{3/2} T_{\text{laser}} w_0^2}. \quad (4.20)$$

The results of the  $S_{\text{peak}}$  fits are included in Figure 4.3. The Raman fraction was calculated to be  $f_R = 0.37$ .

The experimental value of the nonlinear refractive index is  $n_2 = 1.62 \cdot 10^{-10} \frac{m^2}{W}$  which corresponds to  $\chi^{(3)} = 3.31 \cdot 10^{-20} \frac{m}{V^2}$ . This is about 75 % of the value in literature [125].

#### 4.4.2 Simulation of the output signal

The pulse propagation in the waveguide is simulated using the split-step method or extended Crank-Nicholson scheme. The program code was developed by Arnaud Couairon from the École Polytechnique in Palaiseau (France). First, constants and optical parameters are defined and calculated. Then the grids are determined. The initial field  $E_{\text{input}} = E(r, t, z = 0)$  is defined for a Gaussian beam profile, where  $z$  is the propagation direction and  $r$  is the radial coordinate when using a cylindrical coordinate system. Dispersion and the nonlinear effects mentioned in Section 4.3 are taken into account. The unidirectional pulse propagation equation is calculated stepwise in a loop according to the chosen grid in propagation direction. [178]

To compare the measured data to the simulation results the measured Raman signals (see Fig. 4.4 (a)) are fitted with the decaying sinusoidal function

$$S(t) = A_0 \exp(-\Gamma t) \cdot \sin(-\Omega t) \quad (4.21)$$

which results in the fit parameter values  $\Omega = 0.05629 \frac{1}{\text{fs}}$  and  $\Gamma = 0.01918 \frac{1}{\text{fs}}$ .

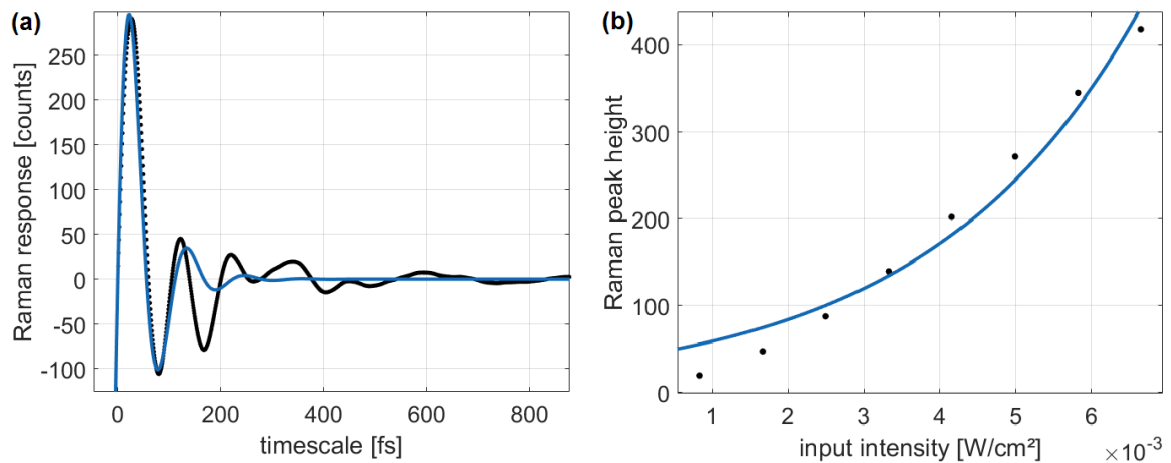


Figure 4.4: (a) Fit (blue) of the measured Raman response signal (black). (b) Simulated output signal for a 7 mm long waveguide.

The fit matches the first oscillation quite well but fails for further oscillation. Adding more terms to the fit function can lower the fit errors and match the fit function to the measured values. However, this would generate many new fit parameters that are difficult to be implemented in the simulation code.

These parameters are fed into the simulation. Assuming the Raman fraction  $f_R = 0.37$  and a length of the waveguide of  $L = 7$  mm the output signal for a propagation length in GLS is generated.

Varying the input powers several Raman spectra can be produced and the peak values at  $1.58 \mu\text{m}$  are calculated, respectively. By fitting these values with Eqn. 4.19 and 4.20 the Raman gain  $g_0 = 5.12 \cdot 10^{-12}$  is obtained.

When using the measured Raman response instead of the fit function as input for the simulation the resulting Raman gain is calculated to be  $g_0 = 5.14 \cdot 10^{-12}$ . This shows that though the fit of the Raman response only matches the first oscillation well the resulting Raman gain is still well distinguished.

Both values are in the same order of magnitude with the Raman gain determined by the measurement.

When comparing the simulation results with ( $g_0 = 5.149 \cdot 10^{-12}$ ) and without ( $g_0 = 5.077 \cdot 10^{-12}$ ) using the term for the Raman-Kerr effect no significant changes can be observed.

For these wavelengths full wave mixing is interfering with the Raman effect.

### 4.4.3 Application

The purpose of the simulations and experiments was to explore the spectral broadening in waveguides in order to generate a broad supercontinuum formed by pulses in the normal group velocity dispersion (GVD) regime. The focus was put to Raman scattering as an important part of this process, for on one hand, the red shift of nonlinear waves induced by the inelastic process shifts the pulses towards the zero GVD point and on the other hand, since the Raman effect is intensity dependent, the pulse separation should take place for pulses with different peak powers.

When the power of a single pulse reaches a certain threshold while traveling through a material with a normal GVD, wave breaking appears. [192] Shock waves induce instabilities in the pulse profile which are broadened by pulse steepening. In the normal GVD regime the red-shifted light (generated by SPM) propagates faster and overtakes the blue-shifted light. Interference can be observed. This can be observed as dips in the flat intensity plateau developed in the central part of the input pulse (dark solitons). Close to the zero dispersion wavelength a compensation between phase matching and dispersion is taking place. Dark solitons are solitary waves that maintain their shape during propagation. [193]

Raman scattering and SPM can broaden an ultrashort pulse to over 100 nm and generate a supercontinuum. [177]

Pulse propagation simulations have shown that for a wavelength of  $3.39 \mu\text{m}$  near the zero group velocity dispersion wavelength and a Raman fraction of 0.37 the propagation distance that is needed to generate dark solitons is larger than 20 cm. A sample of this length with homogeneous properties throughout the whole glass is difficult to manufacture which means instead of GLS waveguides it is more practicable to use fibers which were not available within the limits of this work. Further investigations on this subject could lead to more interesting results.

# Chapter 5

## Conclusions and Outlook

Multi-scan ultrafast laser inscription was shown to be a suitable manufacturing technique of single mode waveguides with a 3D geometry in gallium lanthanum sulfide (GLS) glass. The irradiation with highly focused laser light at a wavelength of  $\lambda = 1026$  nm induces a positive local refractive index change in the focal volume. GLS is a convenient material for waveguides operating in the mid-infrared range, which is interesting for astrophotonic applications. Simulations of GLS glass have shown that the structure of GLS is dominated by  $\text{GaS}_4$  tetrahedra and  $\text{LaS}_8$  polyhedra in which the lanthanum atoms can have a coordination number of 6, 7 and 8. SEM images of etched waveguide cross sections showed a significant change in the surface structure for waveguides written with different writing parameters. Higher laser powers and lower writing speeds result in a clearly rougher surface showing regular ripples, which could indicate the formation of a crystalline structure. Also, the etching rates increase for higher deposited energies due to laser irradiation which can lead to increased micro-cracks or vulnerable atomic configurations.

For the first time, Raman microscopy was used to investigate laser treated GLS glass. Though the Raman spectra of GLS glass are already published [127, 128, 194], the measurements connected to this thesis revealed a structural change of the laser irradiated material from the bulk in direct comparison of the spectra of bulk and waveguide on one sample. Gallium sulfide tetrahedra and lanthanum sulfide polyhedra are the main contributors to the intensity change of the compared Raman peaks. The laser parameters seem to have a crucial influence on the Raman spectra. Low laser powers and high writing speeds increase the Raman intensities for the waveguide structure compared to the bulk. The structural simulations of the GLS glass and the comparison of the measured Raman spectra of bulk and waveguide material for different writing parameters indicate that a change in the La coordina-



tion due to the laser treatment might lead to a reorientation of the  $\text{GaS}_4$  tetrahedra and the  $\text{LaS}_8$  polyhedra, which can result in a local densification of the GLS glass in the waveguide region by lanthanum migration from the surrounding material. Partial crystallization for high induced temperatures might also contribute to the properties of the laser written waveguides.

Structural investigations with different independent experiments, such as mode field diameter (MFD) measurements and polarimetry, showed a consistent behavior. A densification of the waveguide material by atomic migration and partial crystallization is indicated by the comparison of cross sections of Raman peak heights and the stress field over a waveguide which can distinguish a migration region of lower density at the waveguide borders.

Another contribution to the refractive index change of the irradiated material can be color center formation which can be deduced from microscope images of waveguides and the change in fluorescence spectra for irradiated GLS glass. There is still room for interpretation of the experimental results.

Pre-annealing of waveguides in GLS samples aiming at the relieve of stress induced birefringence showed a material relaxation after an annealing time of 24 h at  $500^\circ\text{C}$ , which also indicates the point of lowest density of the material. The material relaxation for longer annealing times is accompanied by an increasing bulk refractive index. This leads to a smaller difference between bulk and possible waveguide refractive index, so that the refractive index change, which is a crucial factor for wave guiding, becomes smaller. The density of the glass increases for increasing annealing temperatures up to  $4.3 \frac{\text{g}}{\text{cm}^3}$  at  $550^\circ\text{C}$ .

Stresses induced by the laser writing have an influence on the properties of waveguides written within the range of the stress field of other waveguides. Asymmetric and polarization-dependent output patterns are the consequence of this dependency. The densification of the laser treated glass is followed by the development of tensile stresses in the surrounding material, which cause a deviation of the refractive index change of the neighboring later written waveguides. Birefringence control and loss reduction during the waveguide fabrication can improve integrated optics components for interferometric beam combination significantly.

A symmetrization of both a 7-waveguide and a 23-waveguide zig-zag array has been achieved for waveguide arrays up to 22 mm length by adjusting  $\Delta\beta$  of neighboring waveguides by a linear increase of the writing speed for successive waveguides. The still remaining polarization dependence indicates a stress field which cannot be corrected with the change of the propagation constant. A variation of the waveguide shape, the separation distance, laser wavelength, repetition rate or pulse length, but

also a temperature treatment could reduce the birefringent effect.

A new 4-telescope discrete beam combiner (DBC) with 23 parallel waveguides with a zig-zag geometry was manufactured and the corresponding visibility-to-pixel matrix (V2PM) was derived. It showed a low condition number of 14 which is comparable to the performance of the GRAVITY instrument at the VLTI. The instrumental visibilities are ranging from 0.86 to 0.97 for the 6 baselines while the estimated coherence functions were closer to unity, ranging from 0.95 to 1.04 with signal-to-noise ratios from 12 to 25. Nevertheless there is still potential to improve the performance of the DBC.

The ABCD beam combination scheme that is actually used at GRAVITY was tested in a 2-telescope configuration. The interferometric combination of the input beams was achieved by the use of directional couplers while exploiting the 3D-writing advantage of ultrafast laser inscription (ULI) for crossing waveguides without intersection. A visibility of 0.92 and a SNR of 28 was achieved.

The Raman response function of a 7 mm-long waveguide in GLS glass was measured by fitting the spectral broadening of the main laser peak at  $1.55 \mu\text{m}$  and the height of the signal peaks at the seed wavelength of  $1.58 \mu\text{m}$  for different input laser powers. The measured values for the laser gain are close to the results obtained with simulations of the pulse propagation in the waveguide. The Raman-Kerr effect influences the output signal only to a small extent, as the comparison of the simulated signals including and excluding the Raman-Kerr term revealed. The generation of dark solitons in GLS waveguides glass close to the zero group velocity dispersion wavelength was calculated to be occur after a propagation distance of over 20 cm. Therefore, to prove the values experimentally GLS fibers should be preferred to waveguides in bulk GLS glass.

A parameter set using a lower number of scans and correspondingly larger spaces between the scan lines, together with a decreased writing speed, which was not addressed in this thesis, was found to generate waveguides with even lower propagation losses of  $0.3 \frac{\text{dB}}{\text{cm}}$ . This shows that there is still room for improvement regarding the waveguide losses and the performance of the IO devices.

In addition, annealing connected with stress management should be researched more intensively.

Further experiments need to be done to verify and refine the results regarding the structural change due to laser irradiation.

The next step for the development of a competitive ABCD beam combiner is the development of a design that allows the combination of 4 telescopes. Measurements

on a beam splitter obtaining 3 output beams from 1 input beam, which are necessary for this device, are already in progress. Therefore, the design parameters for the 4-telescope ABCD beam combiner can be calculated and implemented soon.

# References

- [1] BUSCHER, D.F.: *Practical optical interferometry: Imaging at visible and infrared wavelengths*. Cambridge University Press, 2015
- [2] ESO: *The Extremely Large Telescope: The world's biggest eye on the sky*. <https://www.eso.org/public/teles-instr/elt/>,
- [3] ZHAO, M. ; MONNIER, J.D. ; CHE, X. ; PEDRETTI, E. ; THUREAU, N. ; SCHAEFER, G. ; TEN BRUMMELAAR, T. ; MÉRAND, A. ; RIDGWAY, S.T. ; MCALISTER, H. ; TURNER, N. ; STURMANN, J. ; STURMANN, L. ; GOLDFINGER, P.J. ; FARRINGTON, C.: Towards direct detection of hot jupiters with precision closure phase: Calibration studies and first results from the CHARA array. In: *Publications of the Astronomical Society of the Pacific* 123 (2011), S. 964–975
- [4] KRAUS, A.L. ; IRELAND, M.J.: LkCa 15: A young exoplanet caught at formation? In: *The Astrophysical Journal* 745/1 (2012), S. 1–12
- [5] FALCKE, H. ; MELIA, F. ; AGOL, E.: Viewing the shadow of the black hole at the galactic center. In: *Astrophysical Journal* 528/1 (2000), S. L13–L16
- [6] ARMITAGE, P.J.: *Astrophysics of planet formation*. Cambridge University Press, 2010
- [7] WOLF, S. ; MALBET, F. ; ALEXANDER, R. ; BERGER, J.P. ; CREECH-EAKMAN, M. ; DUCHENE, G. ; DUTREY, A. ; MORDASINI, C. ; PANTIN, E. ; PONT, F. ; POTT, J.U. ; TATULLI, E. ; TESTI, L.: Circumstellar disks and planets. Science cases for next-generation optical/infrared long-baseline interferometers. In: *Astronomy & Astrophysics Review* 20 (2012), S. 82
- [8] MICHELSON, A.A.: On the application of interference methods to astronomical measurements. In: *Philosophical Magazine* 30 (1890), S. 1–20
- [9] MICHELSON, A.A.: Measurement of jupiter's satellites by interference. In: *Nature* 45 (1891), S. 160–161

- 
- [10] HANIFF, C.: An introduction to the theory of interferometry. In: *New Astronomy Reviews* 51 (2007), S. 565–575
- [11] BORN, M. ; WOLF, E.: *Principles of optics*. Cambridge University Press, 1999
- [12] YOUNG, T.: On the theory of light and colors. In: *Philosophical Transactions of the Royal Society London* 387 (1802), S. 12–48
- [13] KLOPPENBORG, B. ; STENCEL, R. ; MONNIER, J.D. ; SCHAEFER, G. ; ZHAO, M. ; BARON, F. ; MCALISTER, H. ; TEN BRUMMELAAR, T. ; CHE, X. ; FARRINGTON, C. ; PEDRETTI, E. ; SALLAVE-GOLDFINGER, P.J. ; STURMANN, J. ; STURMANN, L. ; THUREAU, N. ; TURNER, N. ; CARROLL, S.M.: Infrared images of the transiting disk in the  $\epsilon$  Aurigae system. In: *Nature* 464 (2010), S. 870–872
- [14] MONNIER, J.D: Optical interferometry in astronomy. In: *Reports on Progress in Physics* 66/5 (2003), S. 789
- [15] LACOUR, S. ; MEIMON, S. ; THIEBAUT, E. ; PERRIN, G. ; VERHOELST, T. ; PEDRETTI, E. ; SCHULLER, P.A. ; MUGNIER, L. ; MONNIER, J. ; BERGER, J.P. ; HAUBOIS, X. ; PONCELET, A. ; BESNERAIS, G. L. ; ERIKSSON, K. ; MILLAN-GABET, R. ; TRAUB, S. Ragland and M. Lacasse and W.: The limb-darkened Arcturus: Imaging with the IOTA/IONIC interferometer. In: *Experimental Astronomy* 485 (2011), S. 561–570
- [16] JOCOU, L. ; PERRAUT, K. ; MOULIN, T. ; MAGNARD, Y. ; LABEYE, P. ; LAPRAS, V. ; NOLOT, A. ; PERRIN, G. ; EISENHAEUER, F. ; HOLMES, C. ; AMORIM, A. ; BRANDNER, W. ; STRAUBMEIER, C.: The beam combiners of GRAVITY VLTI instrument: Concept, development and performance in laboratory. In: *Proc. SPIE*, 2014
- [17] LE BOUQUIN, J.B. ; BERGER, J.P. ; LAZAREFF, B. ; ZINS, G. ; HAGUENAUER, P. ; JOCOU, L. ; KERN, P. ; MILLAN-GABET, R. ; TRAUB, W. ; ABSIL, O. ; AUGEREAU, J.C. ; BENISTY, M. ; BLIND, N. ; BONFILS, X. ; BOURGET, P. ; DELBOULBE, A. ; FEAUTRIER, P. ; GERMAIN, M. ; GITTON, P. ; GILLIER, D. ; KIEKEBUSCH, M. ; KLUSKA, J. ; KNUDSTRUP, J. ; LABEYE, P. ; LIZON, J.L. ; MONIN, J.L. ; MAGNARD, Y. ; MALBET, F. ; MAUREL, D. ; MÉNARD, F. ; MICALLEF, M. ; MICHAUD, L. ; MONTAGNIER, G. ; MOREL, S. ; MOULIN, T. ; PERRAUT, K. ; POPOVIC, D. ; RABOU, P. ; ROCHAT, S. ; ROJAS, C. ; ROUSSEL, F. ; ROUX, A. ; STADLER, E. ; STEFL, S. ; TATULLI, E. ; VENTURA, N.: PIONIER: A 4-telescope visitor instrument at VLTI. In: *Astronomy & Astrophysics* 535 (2011), S. A67

- [18] PETROV, R.G. ; MALBET, F. ; WEIGELT, G. ; ANTONELLI, P. ; BECKMANN, U. ; BRESSON, Y. ; CHELLI, A. ; DUGUÉ, M. ; DUVERT, G. ; GENNARI, S. ; GLÜCK, L. ; KERN, P. ; LAGARDE, S. ; LE COARER, E. ; LISI, F. ; MILLOUR, F. ; PERRAUT, K. ; PUGET, P. ; RANTAKYRÖ, F. ; ROBBE-DUBOIS, S. ; ROUSSEL, A. ; SALINARI, P. ; TATULLI, E. ; ZINS, G. ; ACCARDO, M. ; ACKE, B. ; AGABI, K. ; ALTARIBA, E. ; AREZKI, B. ; ARISTIDI, E. ; BAFFA, C. ; BEHREND, J. ; BLÖCKER, T. ; BONHOMME, S. ; BUSONI, S. ; CASSAING, F. ; CLAUSSE, J.M. ; COLIN, J. ; CONNOT, C. ; DELBOULBÉ, A. ; SOUZA, A. D. ; DRIEBE, T. ; FEAUTRIER, P. ; FERRUZZI, D. ; FORVEILLE, T. ; FOSSAT, E. ; FOY, R. ; FRAIX-BURNET, D. ; GALLARDO, A. ; GIANI, E. ; GIL, C. ; GLENTZLIN, A. ; HEIDEN, M. ; HEININGER, M. ; HERNANDEZ UTRERA, O. ; HOFMANN, K.H. ; KAMM, D. ; KIEKEBUSCH, M. ; KRAUS, S. ; LE CONTEL, D. ; LE CONTEL, J.M. ; LESOURD, T. ; LOPEZ, B. ; LOPEZ, M. ; MAGNARD, Y. ; MARCONI, A. ; MARS, G. ; MARTINOT-LAGARDE, G. ; MATHIAS, P. ; MÉGE, P. ; MONIN, J.L. ; MOUILLET, D. ; MOURARD, D. ; NUSSBAUM, E. ; OHNAKA, K. ; PACHECO, J. ; PERRIER, C. ; RABBIA, Y. ; REBATTU, S. ; REYNAUD, F. ; RICHICHI, A. ; ROBINI, A. ; SACCHETTINI, M. ; SCHERTL, D. ; SCHÖLLER, M. ; SOLSCHEID, W. ; SPANG, A. ; STEE, P. ; STEFANINI, P. ; TALLON, M. ; TALLON-BOSC, I. ; TASSO, D. ; TESTI, L. ; VAKILI, F. ; VON DER LÜHE, O. ; VALTIER, J.C. ; VANNIER, M. ; VENTURA, N.: AMBER, the near-infrared spectro-interferometric three-telescope VLTI instrument. In: *Astronomy & Astrophysics* 464/1 (2007), S. 1–12
- [19] ABUTER, R. ; ACCARDO, M. ; AMORIM, A. ; ANUGU, N. ; ÁVILA, G. ; AZOUAOU, N. ; BENISTY, M. ; BERGER, J.P. ; BLIND, N. ; BONNET, H. ; BOURGET, P. ; BRANDNER, W. ; BRAST, R. ; BURON, A. ; BURTSCHER, L. ; CASSAING, F. ; CHAPRON, F. ; CHOQUET, É. ; CLÉNET, Y. ; COLLIN, C. ; COUÉ, V. ; DU FORESTO ; DE WIT, W. ; ZEEUW, P.T. de ; DEEN, C. ; DELPLANCKE-STRÖBELE, F. ; DEMBET, R. ; DERIE, F. ; DEXTER, J. ; DUVERT, G. ; EBERT, M. ; ECKART, A. ; EISENHAEUER, F. ; ESSELBORN, M. ; ÉDOU, P. ; FINGER, G. ; GARCIA, P. ; GARCIA DABO, C.E. ; LOPEZ, R. G. ; GENDRON, E. ; GENZEL, R. ; GILLESSEN, S. ; GONTE, F. ; GORDO, P. ; GROULD, M. ; GRÖZINGER, U. ; GUIEU, S. ; HAGUENAUER, P. ; HANS, O. ; HAUBOIS, X. ; HAUG, M. ; HAUSSMANN, F. ; HENNING, T. ; HIPPLER, S. ; HORROBIN, M. ; HUBER, A. ; HUBERT, Z. ; HUBIN, N. ; HUMMEL, C.A. ; JAKOB, G. ; JANSSEN, A. ; JOCHUM, L. ; JOCOU, L. ; KAUFER, A. ; KELLNER, S. ; KENDREW, S. ; KERN, L. ; KERVELLA, P. ; KIEKEBUSCH, M. ; KLEIN, R. ; KOK, Y. ; KOLB, J. ; KULAS, M. ; LACOUR, S. ; LAPEYRÉRE, V. ; LAZAREFF, B. ; LE BOUQUIN, J.B. ; LÉNA, P. ; LENZEN, R. ; LÉVÊQUE, S. ; LIPPA, M. ; MAGNARD, Y. ; MEHRGAN, L. ; MELLEIN, M. ; MÉRAND, A. ; MORENO-VENTAS, J. ; MOULIN, T. ; MÜLLER, E. ; MÜLLER, F. ; NEUMANN, U. ; OBERTI, S. ; OTT, T. ; PALLANCA, L. ; PANDURO, J. ; PASQUINI, L. ; PAUMARD,

- T. ; PERCHERON, I. ; PERRAUT, K. ; PERRIN, G. ; PFLÜGER, A. ; PFUHL, O. ; DUC, T. P. ; PLEWA, P.M. ; POPOVIC, D. ; RABIEN, S. ; RAMÍREZ, A. ; RAMOS, J. ; RAU, C. ; RIQUELME, M. ; ROHLOFF, R.R. ; ROUSSET, G. ; SANCHEZ-BERMUDEZ, J. ; SCHEITHAUER, S. ; SCHÖLLER, M. ; SCHUHLER, N. ; SPYROMILIO, J. ; STRAUBMEIER, C. ; STURM, E. ; SUAREZ, M. ; TRISTRAM, K.R. ; VENTURA, N. ; VINCENT, F. ; WAISBERG, I. ; WANK, I. ; WEBER, J. ; WIEPRECHT, E. ; WIEST, M. ; WIEZORREK, E. ; WITTKOWSKI, M. ; WOILLEZ, J. ; WOLFF, B. ; YAZICI, S. ; ZIEGLER, D. ; ZINS, G.: First light for GRAVITY: Phase referencing optical interferometry for the Very Large Telescope Interferometer. In: *Astronomy & Astrophysics* 602/A94 (2017), S. 23
- [20] LAGARDE, S. ; LOPEZ, B. ; PETROV, R.G. ; HOFMANN, K.H. ; KRAUS, S. ; JAFFE, W. ; ANTONELLI, P. ; BRESSON, Y. ; LEINERT, C. ; MATTER, A.: MATISSE: Concept analysis. In: *Proc. SPIE*, 2008
- [21] MCALISTER, H.A. ; TEN BRUMMELAAR, T.A. ; GIES, D.R. ; HUANG, W. ; BAGNUOLO, W.G. ; SHURE, M.A. ; STURMANN, J. ; STURMANN, L. ; TURNER, N.H. ; TAYLOR, S.F. ; BERGER, D.H. ; BAINES, E.K. ; GRUNDSTROM, E. ; OGDEN, C. ; RIDGWAY, S.T. ; VAN BELLE, G.: First results from the CHARA array. I. An interferometric and spectroscopic study of the fast rotator alpha Leonis (Regulus). In: *Astrophysical Journal* 628 (2005), S. 439–452
- [22] NASA: <https://science.nasa.gov/missions/lbti>
- [23] OPTICAL, Omega: *Professional Astronomy filters*. 2010
- [24] GLINDEMANN, A.: *Principles of Stellar Interferometry*. Springer, 2011
- [25] MALBET, F. ; KERN, P. ; SCHANEN-DUPOINT, I. ; BERGER, J.P. ; ROUSSELET-PERRAUT, K. ; BENECH, P.: Integrated optics for astronomical interferometry. In: *Astronomy & Astrophysics Supplement Series* 138 (1999), S. 135–145
- [26] LABADIE, L. ; WALLNER, O.: Mid-infrared guided optics: A perspective for astronomical instruments. In: *Optics Express* 17 (2009), S. 1947–1962
- [27] BENISTY, M. ; BERGER, J.P. ; JOCOU, L. ; LABEYE, P. ; MALBET, F. ; PERRAUT, K. ; KERN, P.: An integrated optics beam combiner for the second generation VLTI instruments. In: *Astronomy & Astrophysics* 498 (2009), S. 601–613
- [28] KERN, P. ; MALBET, F.: Astrofib'96: Integrated optics for astronomical interferometry. In: *Proc. of conference at Grenoble (France)*, 1997

- [29] GRELIN, J. ; BOUCHARD, A. ; GHIBAUDO, E. ; BROQUIN, J.E.: Study of  $\text{Ag}^+/\text{Na}^+$  ion-exchange diffusion on germanate glasses: Realization of single-mode waveguides at the wavelength of  $1.55 \mu\text{m}$ . In: *Materials Science and Engineering B, Solid-State Materials for Advanced Technology* 149/2 (2007), S. 190–194
- [30] RUAN, Y. ; LI, W. ; JARVIS, R. ; MADSEN, N. ; RODE, A. ; LUTHER-DAVIES, B.: Fabrication and characterization of low loss rib chalcogenide waveguides made by dry etching. In: *Optics Express* 12/21 (2004), S. 5140–5145
- [31] MADDEN, S.J. ; CHOI, D.Y. ; BULLA, D.A. ; RODE, A.V. ; LUTHER-DAVIES, B. ; TA'EEED, V.G. ; PELUSI, M.D. ; EGGLETON, B.J.: Long, low loss etched  $\text{As}_2\text{S}_3$  chalcogenide waveguides for all-optical signal regeneration. In: *Optics Express* 15/22 (2007), S. 14414–14421
- [32] MA, P. ; CHOI, D.Y. ; YU, Y. ; GAI, X. ; YANG, Z. ; DEBBARMA, S. ; MADDEN, S. ; LUTHER-DAVIES, B.: Low-loss chalcogenide waveguides for chemical sensing in the midinfrared. In: *Optics Express* 21/24 (2013), S. 29927–29937
- [33] GATTASS, R.R. ; MAZUR, E.: Femtosecond laser micromachining in transparent materials. In: *Nature Photonics* 2 (2008), S. 219–225
- [34] DAVIS, K.M. ; MIURA, K. ; SUGIMOTO, N. ; HIRA, K.: Writing waveguides in glass with a femtosecond laser. In: *Optics Letters* 21/21 (1996), S. 1729–1731
- [35] STRELTSOV, A.M. ; BORRELLI, N.F.: Study of femtosecond-laser-written waveguides in glasses. In: *Journal of the Optical Society of America B* 19/10 (2002), S. 2496–2504
- [36] CHAN, J.W. ; HUSER, T.R. ; RISBUD, S.H. ; HAYDEN, J.S. ; KROL, D.M.: Waveguide fabrication in phosphate glasses using femtosecond laser pulses. In: *Applied Physics Letters* 82/15 (2003), S. 2371–2373
- [37] SIEGEL, J. ; FERNANDEZ-NAVARRO, J.M. ; GARCIA-NAVARRO, A. ; DIEZ-BLANCO, V. ; SANZ, O. ; SOLIS, J. ; VEGA, F. ; ARMENGOL, J.: Waveguide structures in heavy metal oxide glass written with femtosecond laser pulses above the critical self-focusing threshold. In: *Applied Physics Letters* 86 (2005), S. 121109–21109
- [38] EFIMOV, O.M. ; GLEBOV, L.B. ; RICHARDSON, K.A. ; VAN STRYLAND, E. ; CARDINAL, T. ; PARK, S.H. ; COUZI, M. ; BRUNÉEL, J.L.: Waveguide writing in chalcogenide glasses by a train of femtosecond laser pulses. In: *Optical Materials* 17 (2001), S. 379–386



- [39] GROSS, S. ; AMS, M. ; PALMER, G. ; MIESE, C.T. ; WILLIAMS, R.J. ; MARSHALL, G.D. ; FUERBACH, A. ; LANCASTER, D.G. ; EBENDORFF-HEIDEPRIEM, H. ; WITHFORD, M.J.: Ultrafast Laser Inscription in soft glasses: A comparative study of athermal and thermal processing regimes for guided wave optics. In: *International Journal of Applied Glass Science* 3/4 (2012), S. 332–348
- [40] LANCASTER, D.G. ; GROSS, S. ; EBENDORFF-HEIDEPRIEM, H. ; KUAN, K. ; MONRO, T.M. ; AMS, M. ; FUERBACH, A. ; WITHFORD, M.J.: Fifty percent internal slope efficiency femtosecond direct-written  $\text{Tm}^{3+}$ :ZBLAN waveguide laser. In: *Optics Letters* 36 (2011), S. 1587–1589
- [41] BERESNA, M. ; GECEVIČIUS, M. ; KAZANSKY, P.G.: Ultrafast laser direct writing and nanostructuring in transparent materials. In: *Advances in Optics and Photonics* 6/3 (2014), S. 293–339
- [42] KAZANSKY, P.G. ; INOUE, H. ; MITSUYU, T. ; MIURA, K. ; QIU, J. ; HIRAO, K. ; STARROST, F.: Anomalous anisotropic light scattering in Ge-doped silica glass. In: *Physical Review Letters* 82 (1999), S. 2199–2202
- [43] SHIMOTSUMA, Y. ; KAZANSKY, P.G. ; QIU, J. ; HIRAO, K.: Self-organized nanogratings in glass irradiated by ultrashort light pulses. In: *Physics Review Letters* 91 (2003), S. 247405
- [44] RICHTER, S. ; MIESE, C. ; DÖRING, S. ; ZIMMERMANN, F. ; WITHFORD, M.J. ; TÜNNERMANN, A. ; NOLTE, S.: Laser induced nanogratings beyond fused silica - periodic nanostructures in borosilicate glasses and ULE<sup>TM</sup>. In: *Optical Materials Express* 3/8 (2013), S. 1161–1166
- [45] QIU, J. ; KAZANSKI, P.G. ; SI, J. ; MIURA, K. ; MITSUYU, T. ; HIRAO, K. ; GAETA, A.L.: Memorized polarization-dependent light scattering in rare-earth-ion-doped glass. In: *Applied Physics Letters* 77/13 (2000), S. 1940–1942
- [46] SHIMOTSUMA, Y. ; HIRAO, K. ; QIU, J. ; MIURA, K.: Nanofabrication in transparent materials with a femtosecond pulse laser. In: *Journal of Non-Crystalline Solids* 352 (2006), S. 646–656
- [47] WORTMANN, D. ; GOTTMANN, J. ; BRANDT, N. ; HORN-SOLLE, H.: Micro- and nanostructures inside sapphire by fs-laser irradiation and selective etching. In: *Optics Express* 16/3 (2008), S. 1517–1522

- [48] CHEN, F. ; VÁZQUEZ DE ALDANA, J.R.: Optical waveguides in crystalline dielectric materials produced by femtosecond-laser micromachining. In: *Laser & Photonics Reviews* 8/2 (2013), S. 251–275
- [49] BURGHOFF, J. ; GREBING, C. ; NOLTE, S. ; TÜNNERMANN, A.: Efficient frequency doubling in femtosecond laser-written waveguides in lithium niobate. In: *Applied Physics Letters* 89/8 (2006), S. 081108
- [50] OKHRIMCHUK, A.G. ; SHESTAKOV, A.V. ; KHRUSHCHEV, I. ; MITCHELL, J.: Depressed cladding, buried waveguide laser formed in a YAG:Nd<sup>3+</sup> crystal by femtosecond laser writing. In: *Optics Letters* 30/17 (2005), S. 2248–2250
- [51] GLEZER, E. N. ; MAZUR, E.: Ultrafast-laser driven micro-explosions in transparent materials. In: *Applied Physics Letters* 71/7 (1997), S. 882–884
- [52] LOIREAU LOZAC'H, A.M. ; GUITTARD, M. ; FLAHAUT, J.: Glasses formed by rare earth sulphides La<sub>2</sub>S<sub>3</sub> with gallium sulphide Ga<sub>2</sub>S<sub>3</sub>. In: *Material Research Bulletin* 11 (1976), S. 1489–1496
- [53] CRYSTAN LTD, POOLE, UK (Hrsg.): *Gallium lanthanum sulfide (GLS)*. Crystan Ltd, Poole, UK
- [54] CHG SOUTHAMPTON LTD, UK (Hrsg.): *Safety data sheet. Gallium lanthanum sulphide optical glass*. ChG Southampton Ltd, UK, 2005
- [55] BERGER, J.P. ; HAGUENAUER, P. ; KERN, P. ; PERRAUT, K. ; MALBET, F. ; SCHANEN, I. ; SEVERI, M. ; MILLAN-GABET, R. ; TRAUB, W.: Integrated optics for astronomical interferometry: IV. First measurements of stars. In: *Astronomy & Astrophysics* 376 (2001), S. L31–L34
- [56] RODENAS, A. ; MARTIN, G. ; ARZEKI, B. ; PSAILA, N.D. ; JOSE, G. ; JHA, A. ; LABADIE, L. ; KERN, P. ; KAR, A.K. ; THOMSON, R.R.: Three-dimensional mid-infrared photonic circuits in chalcogenide glass. In: *Optics Letters* 37/3 (2012), S. 392–394
- [57] MINARDI, S. ; PERTSCH, T.: Interferometric beam combination with discrete optics. In: *Optics Letters* 35/18 (2010), S. 3009–3011
- [58] MINARDI, S. ; DREISOW, F. ; GRÄFE, M. ; NOLTE, S. ; PERTSCH, T.: Three-dimensional photonic component for multichannel coherence measurements. In: *Optics Letters* 37 (2012), S. 3030–3032

- 
- [59] SAVIAUK, A. ; MINARDI, S. ; DREISOW, F. ; NOLTE, S. ; PERTSCH, T.: 3D-integrated optics component for astronomical spectro-interferometry. In: *Applied Optics* 52/19 (2013), S. 4556–4565
- [60] MINARDI, S.: Photonic lattices for astronomical interferometry. In: *Monthly Notices of the Royal Astronomical Society* 422 (2012), S. 2656–2660
- [61] MINARDI, S.: Nonlocality of coupling and the retrieval of field correlations with arrays of waveguides. In: *Physics Review A* 92 (2015), S. 013804
- [62] SUN, H.B. ; KAWATA, S. ; LEE, S.K. (Hrsg.): *NMR - 3D analysis - Photopolymerization*. Springer Berlin, 2004. – 169–273 S.
- [63] MARUO, S. ; NAKAMURA, O. ; KAWATA, S.: Three-dimensional microfabrication with two-photon-absorbed photopolymerization. In: *Optics Letters* 22/2 (1997), S. 132–134
- [64] STRELTSOV, A.M. ; BORRELLI, N.F.: Fabrication and analysis of a directional coupler written in glass by nanojoule femtosecond laser pulses. In: *Optics Letters* 26 (2001), S. 42–43
- [65] HOMOELLE, D. ; WIELANDY, S. ; GAETA, A.L.: Infrared photosensitivity in silica glasses exposed to femtosecond laser pulses. In: *Optics Letters* 24/18 (1999), S. 1311
- [66] NOLTE, S. ; WILL, M. ; BURGHOFF, J. ; TÜNNERMANN, A.: Ultrafast laser processing: New options for three-dimensional photonic structures. In: *Journal of Modern Optics* 51 (2004), S. 2533–2542
- [67] MINOSHIMA, K. ; KOWALEVICZ, A.M. ; HARTL, I. ; IPPEN, E.P. ; FUJIMOTO, J.G.: Photonic device fabrication in glass by use of nonlinear materials processing with a femtosecond laser oscillator. In: *Optics Letters* 26 (2001), S. 1516–1518
- [68] MINOSHIMA, K. ; KOWALEVICZ, A.M. ; IPPEN, E.P. ; FUJIMOTO, J.G.: Fabrication of coupled mode photonic devices in glass by nonlinear femtosecond laser materials processing. In: *Optics Express* 10 (2002), S. 645–652
- [69] ZHANG, H. ; EATON, S.M. ; HERMAN, P.R.: Single-step writing of Bragg grating waveguides in fused silica with an externally modulated femtosecond fiber laser. In: *Optics Letters* 32/17 (2007), S. 2559–2561

- 
- [70] KÖNIG, K. ; RIEMANN, I. ; FISCHER, P. ; HALBHUBER, K.H.: Intracellular nanosurgery with near infrared femtosecond laser pulses. In: *Cellular and Molecular Biology* 45 (1999), S. 195–201
- [71] WATANABE, W. ; ARAKAWA, N.: Femtosecond laser disruption of subcellular organelles in a living cell. In: *Optics Express* 12 (2004), S. 4203–4213
- [72] SHEN, N. ; DATTA, D. ; SCHAFFER, C.B. ; LE DUC, P. ; INGBER, D.E. ; MAZUR, E.: Ablation of cytoskeletal filaments and mitochondria in live cells using a femtosecond laser nanoscissor. In: *Mechanics & Chemistry of Biosystems* 2 (2005), S. 17–25
- [73] WATANABE, W. ; ONDA, S. ; TAMAKI, T. ; ITOH, K. ; NISHII, J.: Space-selective laser joining of dissimilar transparent materials using femtosecond laser pulses. In: *Applied Physics Letters* 89 (2006), S. 021106
- [74] MIURA, K. ; QIU, J.R. ; MITSUYU, T. ; HIRAO, K.: Space-selective growth of frequency-conversion crystals in glasses with ultrashort infrared laser pulses. In: *Optics Letters* 25 (2000), S. 408–410
- [75] YU, B. ; CHEN, B. ; YANG, X. ; QIU, J. ; JIANG, X. ; ZHU, C. ; HIRAO, K.: Study of crystal formation in borate, niobate, and titanate glasses irradiated by femtosecond laser pulses. In: *Journal of the Optical Society of America B Optical Physics* 21 (2004), S. 83–87
- [76] YMETI, A. ; KANGER, J. ; GREVE, J. ; LAMBECK, P. ; WIJN, R. ; HEIDEMAN, R.: Realization of a multichannel integrated young interferometer chemical sensor. In: *Applied Optics* 42/28 (2003), S. 5649–5660
- [77] SZAMEIT, A. ; BURGHOFF, J. ; PERTSCH, T. ; NOLTE, S. ; TÜNNERMANN, A. ; LEDERER, F.: Two-dimensional soliton in cubic fs laser written waveguide arrays in fused silica. In: *Optics Express* 14 (2006), S. 6055–6062
- [78] MEANY, T. ; GRÄFE, M. ; HEILMANN, R. ; PEREZ-LEIJA, A. ; GROSS, S. ; STEEL, M.J. ; WITHFORD, M.J. ; SZAMEIT, A.: Laser written circuits for quantum photonics. In: *Laser & Photonics Review* 9 (2015), S. 363–384
- [79] OREN, D. ; SHECHTMAN, Y. ; MUTZAFI, M. ; ELDAR, Y.C. ; SEGEV, M.: Sparsity-based recovery of three-photon quantum states from two-fold correlations. In: *Optica* 3 (2016), S. 226–232
- [80] TITCHENER, J.G. ; SOLNTSEV, A.S. ; SUKHORUKOV, A.A.: Two-photon tomography using on-chip quantum walks. In: *Optica* 4a (2016), S. 4079–4082

- 
- [81] GLEZER, E. ; MILOSAVLJEVIC, M. ; HUANG, L. ; FINLAY, R. ; HER, T.H. ; CALLAN, T. ; MAZUR, E.: Three-dimensional optical storage inside transparent materials. In: *Optics Letters* 21/24 (1996), S. 2023
- [82] OSELLAME, R. ; CERULLO, G. ; RAMPONI, R. ; ASCHERON, C.E. (Hrsg.): *Femtosecond laser micromachining: Photonic and microfluidic devices in transparent materials*. Springer Berlin Heidelberg, 2012
- [83] GROSS, S. ; JOVANOVIĆ, N. ; SHARP, A. ; IRELAND, M. ; LAWRENCE, J. ; WITHFORD, M.J.: Low loss mid-infrared ZBLAN waveguides for future astronomical applications. In: *Optics Express* 23 (2015), S. 7946
- [84] CHAN, J.W. ; HUSER, T. ; RISBUD, S. ; KROL, D.M.: Structural changes in fused silica after exposure to focused femtosecond laser pulses. In: *Optics Letters* 26 (2001), S. 1726–1728
- [85] JUODKAZIS, S. ; NISHIMURA, K. ; TANAKA, S. ; MISAWA, H. ; GAMALY, E.G. ; LUTHER-DAVIES, B. ; HALLO, L. ; NICOLAI, P. ; TIKHONCHUK, V.T.: Laser-induced microexplosion confined in the bulk of a sapphire crystal: Evidence of multimegabar pressures. In: *Physical Review Letters* 96 (2006), S. 166101
- [86] PONADER, C.W. ; SCHROEDER, J.F. ; STRELTSOV, A.M.: Origin of the refractive-index increase in laser-written waveguides in glasses. In: *Journal of Applied Physics* 103/6 (2008), S. 063516
- [87] BHARDWAJ, V.R. ; CORKUM, P.B. ; RAYNER, D.M. ; HNATOVSKY, C. ; SIMOVA, E. ; TAYLOR, R.S.: Stress in femtosecond-laser-written waveguides in fused silica. In: *Optics Letters* 29 (2004), S. 1312–1314
- [88] RAYNER, D.M. ; NAUMOV, A. ; CORKUM, P.B.: Ultrashort pulse non-linear optical absorption in transparent media. In: *Optics Express* 13 (2005), S. 3208–3217
- [89] FERNANDEZ, T.T. ; HERNANDEZ, M. ; SOTILLO, B. ; EATON, S.M. ; JOSE, G. ; OSELLAME, R. ; JHA, A. ; FERNANDEZ, P. ; SOLIS, J.: Role of ion migrations in ultrafast laser written tellurite glass waveguides. In: *Optics Express* 22 (2014), S. 15298–15304
- [90] MIURA, K. ; QIU, J. ; INOUE, H. ; MITSUYU, T. ; HIRAO, K.: Photowritten optical waveguides in various glasses with ultrashort pulse laser. In: *Applied Physics Letters* 71 (1997), S. 3329–3331

- [91] APOSTOLOPOULOS, G. ; VELLIANITIS, G. ; DIMOULAS, A. ; HOOKER, J.C. ; CONARD, T.: Complex admittance analysis for  $\text{La}_2\text{Hf}_2\text{O}_7/\text{SiO}_2$  high- $\kappa$  dielectric stacks. In: *Applied physics letters* 84/2 (2004), S. 260–262
- [92] NEJADMALAYERI, A. H. ; HERMAN, P. R. ; BURGHOFF, J. ; WILL, M. ; NOLTE, S. ; TÜNNERMANN, A.: Inscription of optical waveguides in crystalline silicon by mid-infrared femtosecond laser pulses. In: *Optics Letters* 30 (2005), S. 964–966
- [93] ZOUBIR, A. ; LOPEZ, C. ; RICHARDSON, M. ; RICHARDSON, K.: Femtosecond laser fabrication of tubular waveguides in poly(methyl-methacrylate). In: *Optics letters* 29/16 (2004), S. 1840–1842
- [94] CAULIER, O. ; LE COQ, D. ; CALVEZ, L. ; BYCHKOV, E. ; MASSELIN, P.: Free carrier accumulation during direct laser writing in chalcogenide glass by light filamentation. In: *Optics Express* 19/21 (2011), S. 20088–20096
- [95] ITOH, K. ; WATANABE, W. ; NOLTE, S. ; SCHAFFER, C.B.: Ultrafast processes for bulk modification of transparent materials. In: *MRS Bulletin* 31 (2006), S. 620–625
- [96] D'AMICO, C. ; CAILLAUD, C. ; VELPULA, P.K. ; BHUYAN, M.K. ; SOMAYAJI, M. ; COLOMBIER, J.P. ; TROLES, J. ; CALVEZ, L. ; NAZABAL, V. ; BOUKENTER, A. ; STOIAN, R.: Ultrafast laser-induced refractive index changes in  $\text{Ge}_{15}\text{As}_{15}\text{S}_{70}$  chalcogenide glass. In: *Optical Materials Express* 6 (2015), S. 1914–1928
- [97] NAMDEO, M. ; CHANSHETTI, U.: Scope of chalcogenide glasses in emerging science and technology. In: *Advances in Engeneering Science and Management* 1/2 (2015), S. 172–178
- [98] BASTOCK, P. ; CRAIG, C. ; KHAN, K. ; WEATHERBY, E. ; YAO, J. ; HEWAK, D.W.: Properties of gallium lanthanum sulphide glass. In: *Proc. CLEO, 2015*
- [99] HEWAK, D.W.: *Personal correspondence via e-mail, (ChG Southampton)*. 2016
- [100] LI, P. ; LI, L.H. ; CHEN, L. ; WU, L.M.: Synthesis, structure and theoretical studies of a new ternary non-centrosymmetric  $\beta\text{-La-Ga-S}_3$ . In: *Journal of Solid State Chemistry* 183/2 (2010), S. 444–450
- [101] YAYAMA, H. ; FUJINO, S. ; MORINAGA, K. ; TAKEBE, H. ; HEWAK, D.W. ; PAYNE, D.N.: Refractive index dispersion of gallium lanthanum sulfide and oxysulfide glasses. In: *Journal of Non-Crystalline Solids* 239 (1998), S. 187–191

- 
- [102] BENAZETH, S. ; TUILLIER, M.H. ; LOIREAU-LOZAC'H, A.M. ; DEXPERT, H. ; LAGARDE, P. ; FLAHAUT, J.: An EXAFS structural approach of the lanthanum-gallium-sulfur glasses. In: *Journal of Non-Crystalline Solids* 110/1 (1989), S. 89–100
- [103] HUGHES, M.A.: *Modified chalcogenide glasses for optical device applications*, University of Southampton, Diss., 2007
- [104] HEWAK, D.W. ; BRADY, D. ; CURRY, R.J. ; ELLIOTT, G. ; HUANG, C.C. ; HUGHES, M. ; KNIGHT, K. ; MAIRAJ, A. ; PETROVICH, M. ; SMITH, C. ; SPROAT, C. ; RESEARCH SIGNPOST, India Kerala (Hrsg.): *Chalcogenide glasses for photonics device applications*. G.S. Murugan, 2010
- [105] PETROVICH, M.N. ; HEWAK, D.W.: Materials data from Crystran Ltd . Poole . UK: Gallium lanthanum sulphide (GLS). In: *Journal of Non-Crystalline Solids* 326-327 (2003), S. 93–97
- [106] BÖTTGER, G.C. ; ZORLL, O. ; MÖNCH, U.: *Längenmessung und Brechzahlbestimmung mit Lichtinterferenzen. Methoden und Anordnungen zum Messen mit Lichtwellenlängen als Maßeinheit unter Bevorzugung von Endmaßen und dünnen Schichten*. Leipzig, Fachbuchverlag, 1954
- [107] SALEH, B.E.A. ; TEICH, M.C.: *Fundamentals of photonics*. Wiley, Hoboken, New Jersey, 2007
- [108] WEST, Y.D. ; SCHWEIZER, T. ; BRADY, D.J. ; HEWAK, D.W.: Gallium lanthanum sulphide fibers for infrared transmission. In: *Fiber and Integrated Optics* 19/3 (2000), S. 229–250
- [109] DIENER, R. ; MINARDI, S. ; TEPPER, J. ; NOLTE, S. ; LABADIE, L.: All-in-one 4-telescope beam combination with a zig-zag array of waveguides. In: *Proc. SPIE*, 2016
- [110] DIENER, R. ; TABACCHI, G. ; NOLTE, S. ; MINARDI, S.: Structural modification of gallium lanthanum sulfide glass induced by ultrafast laser inscription. In: *Proc. SPIE*, 2017
- [111] AMS, M. ; MARSHALL, G.D. ; SPENCE, D. ; WITHFORD, M.: Slit beam shaping method for femtosecond laser direct-write fabrication of symmetric waveguides in bulk glasses. In: *Optics Express* 13/15 (2005), S. 5676–81
- [112] ARRIOLA, A. ; MUKHERJEE, S. ; CHOUDHURY, D. ; LABADIE, L. ; THOMSON, R.R.: Ultrafast laser inscription of mid-IR directional couplers for stellar interferometry. In: *Optics Letters* 39 (2014), S. 4820–4822

- [113] OKAMURA, Y. ; MIKI, A. ; YAMAMOTO, S.: Observation of wave propagation in integrated optical circuits. In: *Applied Optics* 25/19 (1986), S. 3405–3408
- [114] WEBER, H.P. ; DUNN, F.A. ; LEIBOLT, W.N.: Loss measurements in thin-film optical waveguides. In: *Applied Optics* 12/4 (1973), S. 755–757
- [115] TITTELBACH, G. ; RICHTER, B. ; KARTHE, W.: Comparison of three transmission methods for integrated optical waveguide propagation loss measurement. In: *Pure and Applied Optics* 2 (1993), S. 683–706
- [116] QIU, J.: Femtosecond laser-induced microstructures in glasses and applications in micro-optics. In: *The Chemical Record* 4/1 (2004), S. 50–58
- [117] TONG, X.C.: *Advanced materials for integrated optical waveguides*. Springer Series in Advanced Microelectronics, 2014
- [118] COLLIEX, C.: *Elektronenmikroskopie - Eine anwendungsbezogene Einführung*. Wissenschaftliche Verlagsgesellschaft mbH Stuttgart, 2008
- [119] VANDENABEELE, P.: *Practical raman spectroscopy*. Wiley and Sons, Ltd., 2013
- [120] ZHANG, S.L.: *Raman spectroscopy and its application in nanostructures*. Wiley and Sons Ltd., 2012
- [121] MYSEN, B.O. ; FINGER, L.W. ; VIRGO, D. ; SEIFERT, F.A.: Curve-fitting of Raman spectra of silicate glasses. In: *American Mineralogist* 67/7-8 (1982), S. 686–695
- [122] GEISSBERGER, A.E. ; GALEENER, F.L.: Raman studies of vitreous SiO<sub>2</sub> versus fictive temperature. In: *Physical Review B* 28 (1983), S. 3266–3271
- [123] REICHMAN, W. ; CHAN, J.W. ; KROL, D.M.: Confocal fluorescence and Raman microscopy of femtosecond laser-modified fused silica. In: *Journal of Physics: Condensed Matter* 15/31 (2003), S. 2447–2456
- [124] PETIT, L. ; CARLIE, N. ; ADAMIETZ, F. ; COUZI, M. ; RODRIGUEZ, V. ; RICHARDSON, K.: Correlation between physical, optical and structural properties of sulfide glasses in the system Ge-Sb-S. In: *Materials Chemistry and Physics* 97 (2006), S. 64–70
- [125] HUGHES, M. ; YANG, W. ; HEWAK, D.W.: Fabrication and characterization of femtosecond laser written waveguides in chalcogenide glass. In: *Applied Physics Letters* 90 (2007), S. 131113



- [126] McMILLEN, B. ; ZHANG, B. ; CHEN, K.P. ; BENAYAS, A. ; JAQUE, D.: Ultrafast laser fabrication of low-loss waveguides in chalcogenide glass with 0.65 dB/cm loss. In: *Optics Letters* 37 (2012), S. 1418–1420
- [127] NĚMEC, P. ; NAZABAL, V. ; PAVLIŠTA, M. ; MOREAC, A. ; FRUMAR, M. ; VLČEK, M.: Gallium-lanthanum-sulphide amorphous thin films prepared by pulsed laser deposition. In: *Materials Chemistry and Physics* 117 (2009), S. 23–25
- [128] LUCAZEAU, G. ; LEROY, J.: Etude vibrationnelle de  $\alpha$  Ga<sub>2</sub>S<sub>3</sub>. In: *Spectrochimica Acta* 34A (1978), S. 29–32
- [129] LUCAZEAU, G. ; BARNIER, S. ; LOIREAU-LOZAC'H, A.M.: Vibrational spectra, electronic transitions and short order structure of rare earth-gallium sulphide glasses. In: *Spectrochimica Acta* 34A (1978), S. 21–29
- [130] KATTE, H.: *Bildgebende Messung der Spannungsdoppelbrechung in optischen Materialien und Komponenten*. ilis GmbH Erlangen, 2008
- [131] TILLEY, R.D.: *Encyclopedia of color science and technology: Color centers*. Springer, New York, 2013
- [132] LECONTE, B. ; XIE, W.X. ; DOUAY, M. ; BERNAGE, P. ; NIAY, P. ; BAYON, J.F. ; DELEVAQUE, E. ; POIGNANT, H.: Analysis of color-center-related contribution to Bragg grating formation in Ge:SiO<sub>2</sub> fiber based on a local Kramers-Kronig transformation of excess loss spectra. In: *Applied Optics* 36/24 (1997), S. 5923–5930
- [133] DEMTRÖDER, W.: *Experimentalphysik Band 3*. Springer, Berlin/ Heidelberg, 2005
- [134] PIERCE, J.R.: Coupling of modes of propagation. In: *Journal of Applied Physics* 25 (1954), S. 179–183
- [135] MILLER, S.E.: Coupled wave theory and waveguide applications. In: *The Bell System Technical Journal* 33 (1954), S. 661–719
- [136] JONES, A.J.: Coupling of optical fibers and scattering in fibers. In: *Journal of the Optical Society of America* 55/3 (1965), S. 261–271
- [137] SNYDER, A.W.: Coupled-mode theory for optical fibers. In: *Journal of the Optical Society of America* 62/11 (1972), S. 1267–1277
- [138] MARCUSE, D.: Coupled mode theory of round optical fibers. In: *Bell Labs Technical Journal* 52/6 (1973), S. 817–842

- 
- [139] YARIV, A.: Coupled-mode theory for guided-wave optics. In: *IEEE Journal of Quantum Electronics* 9/9 (1973), S. 919–933
- [140] HUANG, W.-P.: Coupled-mode theory for optical waveguides: An overview. In: *Journal of the Optical Society of America A* 11/3 (1994), S. 963–983
- [141] MARCUSE, D.: Directional couplers made of nonidentical asymmetric slabs. Part I: Synchronous couplers. In: *Journal of Lightwave Technology* LT-5/1 (1987), S. 113–118
- [142] IRAJ NAJAFI, S. ; BELANGER, M.: GaAs directional coupler devices: Design considerations. In: *Applied Optics* 26/21 (1987), S. 4593–4596
- [143] TEPPER, J. ; LABADIE, L. ; DIENER, R. ; MINARDI, S. ; POTT, J.U. ; THOMSON, R.R. ; NOLTE, S.: Integrated optics prototype beam combiner for long baseline interferometry in the L and M bands. In: *Astronomy & Astrophysics* 602 (2017), S. A66
- [144] TATULLI, E. ; DUVERT, G.: AMBER data reduction. In: *New Astronomy Reviews* 51 (2007), S. 682–696
- [145] TATULLI, E. ; MILLOUR, F. ; CHELLI, A. ; DUVERT, G. ; ACKE, B. ; HERNANDEZ UTRERA, O. ; HOFMANN, K.H. ; KRAUS, S. ; MALBET, F. ; MÈGE, P. ; PETROV, R.G. ; VANNIER, M. ; ZINS, G. ; ANTONELLI, P. ; BECKMANN, U. ; BRESSON, Y. ; DUGUÉ, M. ; GENNARI, S. ; GLÜCK, L. ; KERN, P. ; LAGARDE, S. ; LECOARER, E. ; LISI, F. ; PERRAUT, K. ; PUGET, P. ; RANTAKYRÖ, F. ; ROBBE-DUBOIS, S. ; ROUSSEL, A. ; WEIGELT, G. ; ACCARDO, M. ; AGABI, K. ; ALTARIBA, E. ; AREZKI, B. ; ARISTIDI, E. ; BAFFA, C. ; BEHREND, J. ; BLÖCKER, T. ; BONHOMME, S. ; BUSONI, S. ; CASSAING, F. ; CLAUSSE, J.M. ; COLIN, J. ; CONNOT, C. ; DELBOULB, A. ; DOMICIANO DE SOUZA, A. ; DRIEBE, T. ; FEAUTRIER, P. ; FERRUZZI, D. ; FORVEILLE, T. ; FOSSAT, E. ; FOY, R. ; FRAIX-BURNET, D. ; GALLARDO, A. ; GIANI, E. ; GIL, C. ; GLENTZLIN, A. ; HEIDEN, M. ; HEININGER, M. ; KAMM, D. ; KIEKEBUSCH, M. ; LE CONTEL, D. ; LE CONTEL, J.M. ; LESOURD, T. ; LOPEZ, B. ; LOPEZ, M. ; MAGNARD, Y. ; MARCONI, A. ; MARS, G. ; MARTINOT-LAGARDE, G. ; MATHIAS, P. ; MONIN, J.L. ; MOUILLET, D. ; MOURARD, D. ; NUSSBAUM, E. ; OHNAKA, K. ; PACHECO, J. ; PERRIER, C. ; RABBIA, Y. ; REBATTU, S. ; REYNAUD, F. ; RICHICHI, A. ; ROBINI, A. ; SACCHETTINI, M. ; SCHERTL, D. ; SCHÖLLER, M. ; SOLSCHEID, W. ; SPANG, A. ; STEE, P. ; STEFANINI, P. ; TALLON, M. ; TALLON-BOSC, I. ; TASSO, D. ; TESTI, L. ; VAKILI, F. ; VON DER LÜHE, O. ; VALTIER, J.C. ; VENTURA, N.: Interferometric data reduction with AMBER/VLTI. Principle, estimators, and illustration. In: *Astronomy & Astrophysics* 464 (2007), S. 29–42

- 
- [146] LACOUR, S. ; JOCOU, L. ; MOULIN, T. ; LABEYE, P.R. ; BENISTY, M. ; BERGER, J.P. ; DELBOULB, A. ; HAUBOIS, X. ; HERWATS, E. ; KERN, P.Y. ; MALBET, F. ; ROUSSELET-PERRAUT, K. ; PERRIN, G.: Characterization of integrated optics components for the second generation of VLTI instruments. In: *Proc. SPIE* Bd. 7013, 2008
- [147] PRESS, W.H. ; TEUKOLSKY, S.A. ; VETTERLING, W.T. ; FLANNERY, B.P.: *Numerical recipes in C++ : the art of scientific computing*. Cambridge University Press, 1986
- [148] DIENER, R. ; TEPPER, J. ; LABADIE, L. ; PERTSCH, T. ; NOLTE, S. ; MINARDI, S.: Towards 3D-photonics, multi-telescope beam combiners for mid-infrared astrometry. In: *Optics Express* 25/16 (2017), S. 19262–19274
- [149] DIENER, R. ; TEPPER, J. ; NOLTE, S. ; LABADIE, L. ; MINARDI, S.: 4-channel interferometry with a zig-zag array of mid-infrared integrated waveguides. In: *Proc. SPIE*, 2017
- [150] BELLOUARD, Y. ; CHAMPION, A. ; McMILLEN, B. ; MUKHERJEE, S. ; THOMSON, R.R. ; PEPIN, C. ; GILLET, P. ; CHENG, Y.: Stress-state manipulation in fused silica via femtosecond laser irradiation. In: *Optica* 3/12 (2016), S. 1285–1293
- [151] GUAN, J. ; LIU, X. ; SALTER, P.S. ; BOOTH, M.J.: Hybrid laser written waveguides in fused silica for low loss and polarization independence. In: *Optics Express* 25 (2017), S. 4845–4859
- [152] LANCERY, M. ; DESMARCHELIER, R. ; COOK, K. ; POUMELLE, B. ; CANNING, J.: Compact birefringent waveplates photo-induced in silica by femtosecond laser. In: *micromachines* 5 (2014), S. 825–838
- [153] CORRIELLI, G. ; CRESPI, A. ; GEREMIA, R. ; RAMPONI, R. ; SANSONI, L. ; SANTINELLI, A. ; MATALONI, P. ; SCARRINO, F. ; OSELLAME, R.: Rotated waveplates in integrated waveguide optics. In: *Nature Communications* 5/4249 (2014), S. 1–6
- [154] McMILLEN, B. ; ATHANASIOU, C. ; BELLOUARD, Y.: Femtosecond laser direct-write waveplates based on stress-induced birefringence. In: *Optics Express* 24 (2016), S. 27239–27252
- [155] COLAVITA, M.M.: Fringe visibility estimators for the Palomar testbed interferometer. In: *Publications of the Astronomical Society of the Pacific* 111/755 (1999), S. 111–117

- 
- [156] ALFANO, R.: *The supercontinuum laser source*. Springer, Berlin, 1989
- [157] SCHENKEL, B.: *Supercontinuum generation and compression*, Swiss Federal Institute of Technology Zürich, Diss., 2004
- [158] ALFANO, R.R. ; SHAPIRO, S.L.: Emission in the region 4000 to 7000 Å via four-photon coupling in glass. In: *Physical Review Letters* 24 (1970), S. 584
- [159] ALFANO, R.R. ; SHAPIRO, S.L.: Observation of self-phase-modulation and small-scale filaments in crystals and glasses. In: *Physical Review Letters* 24 (1970), S. 592
- [160] WERNCKE, W. ; LAU, A. ; PFEIFFER, M. ; LENZ, K. ; WEIGMANN, H.J. ; THUY, C.D.: An anomalous frequency broadening in water. In: *Optics Communications* 4 (1972), S. 413
- [161] YU, W. ; ALFANO, R.R. ; SAM, C.L. ; SEYMOUR, R.J.: Spectral broadening of picosecond 1.06 nm pulse in KBr. In: *Optics Communications* 14 (1975), S. 344
- [162] PENZKOFER, A. ; LAUBEREAU, A. ; KAISER, W.: Stimulated short-wave radiation due to single-frequency resonances of 3%. In: *Physical Review Letters* 31 (1973), S. 863
- [163] SMITH, W.L. ; LIU, P. ; BLOEMBERGEN, N.: Superbroadening in H<sub>2</sub>O and D<sub>2</sub>O by selffocused picosecond pulses from a YAG:Nd laser. In: *Physical Review A* 15 (1977), S. 2396
- [164] FORK, R.L. ; SHANK, C.V. ; HIRLMANN, C. ; YEN, R. ; TOMLINSON, W.J.: Femtosecond white-light continuum pulses. In: *Optics Letters* 8/1 (1983), S. 1
- [165] CORKUM, P.B. ; ROLLAND, C. ; SRINIVASAN-RAO, T.: Supercontinuum generation in gases. In: *Physical Review Letters* 57 (1986), S. 2268
- [166] FRANCOIS, V. ; ILKOV, F.A. ; CHIN, S.L.: Experimental study of the supercontinuum spectral width evolution in CO<sub>2</sub> gas. In: *Optics Communications* 99 (1993), S. 1993
- [167] KASPARIAN, J. ; SAUERBREY, R. ; MONDELAIN, D. ; NIEDERMEIER, S. ; YU, J. ; WOLF, J.P. ; ANDRÉ, Y.B. ; FRANCO, M. ; PRADE, B. ; TZORTZAKIS, S. ; MYSYROWICZ, A. ; RODRIGUEZ, M. ; WILLE, H. ; WÖSTE, L.: Infrared extension of the supercontinuum generated by femtosecond terawatt laser pulses propagating in the atmosphere. In: *Optics Letters* 25 (2000), S. 1397

- 
- [168] LIN, C. ; STOLEN, R.H.: New nanosecond continuum for excited-state spectroscopy. In: *Applied Physics Letters* 28 (1976), S. 216
- [169] BALDECK, P.L. ; ALFANO, R.R.: Intensity effects on the stimulated four photon spectra generated by picosecond pulses in optical fibers. In: *Journal of Lightwave Technology* 5 (1987), S. 1712
- [170] NISOLI, M. ; SILVESTRI, S.D. ; SVELTO, O.: Generation of high energy 10 fs pulses by a new pulse compression technique. In: *Applied Physics Letters* 68 (1996), S. 2793
- [171] BALTUSKA, A. ; FUJI, T. ; KOBAYASHI, T.: Visible pulse compression to 4 fs by optical parametric amplification and programmable dispersion control. In: *Opt. Lett.* 27, 306 (2002).] 27 (2002), S. 306
- [172] SHEN, Y.R.: *Principles of nonlinear optics*. John Wiley & Sons, New York, 1984
- [173] DEL COSO, R. ; SOLIS, J.: Relation between nonlinear refractive index and third-order susceptibility in absorbing media. In: *Journal of the Optical Society of America B* 21/3 (2004), S. 640–644
- [174] STOLEN, R.H. ; LIN, C.: Self-phase-modulation in silica optical fibers. In: *Physical Review A* 17 (1978), S. 1448
- [175] STOLEN, R.H. ; IPPEN, E.P. ; TYNES, A.R.: Raman oscillation in glass optical waveguide. In: *Applied Physics Letters* 20 (1972), S. 63
- [176] HASEGAWA, A. ; TAPPERT, F.: Transmission of stationary nonlinear optical pulses in dispersive dielectric fibers. I. Anomalous dispersion. In: *Applied Physics Letters* 23 (1973), S. 142
- [177] AGRAWAL, G.P. ; KELLEY, P.L. (Hrsg.) ; KAMINOW, I.P. (Hrsg.): *Nonlinear fiber optics*. Academic Press, San Diego, 2001
- [178] COUAIRO, A. ; BRAMBILLA, E. ; CORTI, T. ; MAJUS, D. ; RAMÍRES-GÓNGORA, O.J. ; KOLESIK, M.: Practitioner's guide to laser pulse propagation models and propagation: Numerical implementation and practical usage of modern pulse propagation models. In: *The European Physical Journal Special Topics* 199 (2011), S. 5–76
- [179] PLANCK, M.: On the law of the energy distribution in the normal spectrum. In: *Annalen der Physik* 4 (1901), S. 553–554

- 
- [180] EINSTEIN, A.: Concerning an heuristic point of view toward the emission and transformation of light. In: *Annalen der Physik* 17 (1905), S. 132–148
- [181] SMEKAL, A.: Zur Quantentheorie der Dispersion. In: *Die Naturwissenschaften* 11/43 (1923), S. 873–875
- [182] RAMAN, C.V. ; KRISHNAN, K.S.: A new type of secondary radiation. In: *Nature* 121/3048 (1928), S. 501–502
- [183] LANDSBERG, G.S. ; MANDELSTAM, L.I.: Eine neue Erscheinung bei der Lichtzertreuung in Kristallen. In: *Naturwissenschaften* 16 (1928), S. 557–558
- [184] PLACZEK, G. ; MARX, E. (Hrsg.): *Rayleigh-Streuung und Raman-Effekt in Handbuch der Radiologie*. Akademischer-Verlag, Leipzig, 1934
- [185] OPEL, M. ; VENTURINI, F.: Raman scattering in solids. In: *European Pharmaceutical Review*
- [186] STOLEN, R.H. ; GORDON, J.P. ; TOMLINSON, W.J. ; HAUS, H.A.: Raman response function of silica-core fibers. In: *Journal of the Optical Society of America B* 6 (1989), S. 1159–1166
- [187] BOURKOFF, E. ; ZHAO, W. ; JOSEPH, R.I. ; CHRISTODOULIDES, D. N.: Evolution of femtosecond pulses in single-mode fibers having higher-order nonlinearity and dispersion. In: *Optics Letters* 12 (1987), S. 272
- [188] MITSCHKE, F.M. ; MOLLENAUER, L.F.: Discovery of the soliton self-frequency shift. In: *Optics Letters* 11/10 (1986), S. 659–661
- [189] GORDON, J.P.: Theory of the soliton self-frequency shift. In: *Optics Letters* 11 (1986), S. 622
- [190] HELLWARTH, R.W. ; OWYOUNG, A. ; GEORGE, N.: Origin of the nonlinear refractive index of liquid CCl<sub>4</sub>. In: *Physical Review A* 4/6 (1971), S. 2342–2347
- [191] SHEN, Y.R. ; BLOEMBERGEN, N.: Theory of stimulated Brillouin and Raman scattering. In: *Physical Review* 137/6 (1965), S. A1787–A1805
- [192] ANDERSON, D. ; DESAIX, M. ; LISAK, M. ; QUIROGA-TEIXEIRO, M.L.: Wave breaking in nonlinear-optical fibers. In: *Journal of the Optical Society of America B* 9/8 (1992), S. 1358–1361
- [193] SKRYABIN, D.V. ; GORBACH, A.V.: Looking at a soliton through the prism of optical supercontinuum. In: *Review of Modern Physics* 82 (2010), S. 1287

- [194] SCHWEIZER, T. ; GOUTALAND, F. ; MARTINS, E. ; HEWAK, D.W. ; BROCKLESBY, W.S.: Site-selective spectroscopy in dysprosium-doped chalcogenide glasses for 1.3- $\mu\text{m}$  optical-fiber amplifiers. In: *Journal of the Optical Society of America B* 18/10 (2001), S. 1436–1442

# List of abbreviations

<b>CCD</b>	Charge-Coupled Device
<b>CHARA</b>	Center for High Angular Resolution Astronomy
<b>CN</b>	Condition Number
<b>DBC</b>	Discrete Beam Combiner
<b>ELT</b>	Extremely Large Telescope
<b>FWHM</b>	Full Width at Half Maximum
<b>FWM</b>	Four Wave Mixing
<b>GLINT</b>	Guided light Interferometric Nulling Technology
<b>GLS</b>	Gallium Lanthanum Sulfide
<b>IO</b>	Integrated Optics
<b>LBTI</b>	Large Binocular Telescope Interferometer
<b>LIGO</b>	Laser Interferometric Gravitational-Wave Observatory
<b>MFD</b>	Mode Field Diameter
<b>MPA</b>	Multi-Photon Absorption
<b>NA</b>	Numerical Aperture
<b>Nd:YAG</b>	Neodymium-doped Yttrium Aluminium Garnet ( $\text{Nd:Y}_3\text{Al}_5\text{O}_{12}$ )
<b>NN</b>	Nearest Neighbor
<b>NNN</b>	Next Nearest Neighbor
<b>NOPA</b>	Non-collinear Optical Parametric Amplifier
<b>OPD</b>	Optical Path Difference
<b>OSA</b>	Optical Spectrum Analyzer
<b>P<sub>2</sub>VM</b>	Pixel to Visibility Matrix



<b>PIONIER</b>	Precision Integrated-Optics Near-infrared Imaging Experiment
<b>SBS</b>	Stimulated Brillouin Scattering
<b>SEM</b>	Scanning Electron Microscope
<b>SNR</b>	Signal-to-Noise Ratio
<b>SPM</b>	Self-Phase Modulation
<b>SRS</b>	Stimulated Raman Scattering
<b>SVD</b>	Singular Value Decomposition
<b>SVEA</b>	Slowly Varying Envelope Approximation
<b>TE</b>	Transverse Electric mode
<b>TM</b>	Transverse Magnetic mode
<b>ULI</b>	Ultrafast Laser Inscription
<b>V<sub>2</sub>PM</b>	Visibility to Pixel Matrix
<b>VLT</b>	Very Large Telescope Interferometer
<b>wg</b>	waveguide
<b>Yb:KGW</b>	Ytterbium doped Potassium-Gadolinium Tungstate (Yb:KGd(WO <sub>4</sub> ) <sub>2</sub> )
<b>ZBLAN</b>	ZrF <sub>4</sub> -BaF <sub>2</sub> -LaF <sub>3</sub> -AlF <sub>3</sub> -NaF
<b>ZDW</b>	Zero Dispersion Wavelength

# Ehrenwörtliche Erklärung

Ich erkläre hiermit ehrenwörtlich, dass ich die vorliegende Arbeit selbstständig, ohne unzulässige Hilfe Dritter und ohne Benutzung anderer als der angegebenen Hilfsmittel und Literatur angefertigt habe. Die aus anderen Quellen direkt oder indirekt übernommenen Daten und Konzepte sind unter Angabe der Quellen gekennzeichnet. Bei der Auswahl und Ausfertigung folgenden Materials haben mir die nachstehend aufgeführten Personen in der jeweils beschriebenen Weise entgeltlich/unentgeltlich geholfen:

1. Stefano Minardi - Simulationen zur Parameterbestimmung für zig-zag DBCs und ABCD-Strahlkombinierer
2. Gloria Tabacchi - Simulation der Moleküldynamik des GLS-Glases und Darstellung in Abb. 2.2
3. Arnaud Couairon - Bereitstellung des Matlab-Codes für die Simulationen in Abschnitt 4.4.2
4. Jan Tepper - Photometrische Messung von Strahlkombinierern, beschrieben in Abschnitt 3.5
5. Stefan Fasold und Michael Steinert - Chemisches Ätzen der Proben und REM-Aufnahmen (Abb. 2.10)
6. Christiane Otto und Kristina Garlipp - Schneiden und Polieren des GLS-Glases
7. ChG Southampton Ltd. - Herstellung des GLS-Glases
8. VITRON Spezialwerkstoffe GmbH - Brechzahlmessung für GLS-Glas, beschrieben in Abschnitt 2.2

Weitere Personen waren an der inhaltlich-materiellen Erstellung der vorliegenden Arbeit nicht beteiligt. Insbesondere habe ich hierfür nicht die entgeltliche Hilfe von Vermittlungs- bzw. Beratungsdiensten (Promotionsberater oder andere Personen) in Anspruch genommen. Niemand hat von mir unmittelbar und mittelbar geldwerte Leistungen für Arbeiten erhalten, die im Zusammenhang mit dem Inhalt der vorgelegten Dissertation stehen. Die Arbeit wurde bisher weder im In- noch im Ausland in gleicher oder ähnlicher Form einer anderen Prüfungsbehörde vorgelegt. Die geltende Promotionsordnung der Physikalisch-Astronomischen Fakultät ist mir bekannt. Ich versichere ehrenwörtlich, dass ich nach bestem Wissen die reine Wahrheit gesagt und nichts verschwiegen habe.

Jena, den 28.03.2018  
Ort, Datum

\_\_\_\_\_  
Unterschrift